AIP | Journal of Applied Physics

Tunable, continuous-wave Terahertz photomixer sources and applications

S. Preu, G. H. Döhler, S. Malzer, L. J. Wang, and A. C. Gossard

Citation: J. Appl. Phys. **109**, 061301 (2011); doi: 10.1063/1.3552291
View online: http://dx.doi.org/10.1063/1.3552291
View Table of Contents: http://jap.aip.org/resource/1/JAPIAU/v109/i6
Published by the American Institute of Physics.

APPLIED PHYSICS REVIEWS

Tunable, continuous-wave Terahertz photomixer sources and applications

S. Preu,[1,2,3,a)] G. H. Döhler,[1] S. Malzer,[1] L. J. Wang,[1,4,a)] and A. C. Gossard[2]
[1]*Max Planck Institute for the Science of Light and University of Erlangen-Nürnberg, D-91058 Erlangen, Germany*
[2]*Materials Department, University of California, Santa Barbara, California 93106, USA*
[3]*Now at Physics Department, University of California, Santa Barbara, California 93106, USA*
[4]*Now at Physics Department, Tsinghua University, Beijing 100084, China*

(Received 4 August 2010; accepted 5 January 2011; published online 22 March 2011)

This review is focused on the latest developments in continuous-wave (CW) photomixing for Terahertz (THz) generation. The first part of the paper explains the limiting factors for operation at high frequencies ~ 1 THz, namely transit time or lifetime roll-off, antenna (R)-device (C) RC roll-off, current screening and blocking, and heat dissipation. We will present various realizations of both photoconductive and p-i-n diode–based photomixers to overcome these limitations, including perspectives on novel materials for high-power photomixers operating at telecom wavelengths (1550 nm). In addition to the classical approach of feeding current originating from a small semiconductor photomixer device to an antenna (antenna-based emitter, AE), an antennaless approach in which the active area itself radiates (large area emitter, LAE) is discussed in detail. Although we focus on CW photomixing, we briefly discuss recent results for LAEs under pulsed conditions. Record power levels of 1.5 mW average power and conversion efficiencies as high as 2×10^{-3} have been reached, about 2 orders of magnitude higher than those obtained with CW antenna-based emitters. The second part of the paper is devoted to applications for CW photomixers. We begin with a discussion of the development of novel THz optics. Special attention is paid to experiments exploiting the long coherence length of CW photomixers for coherent emission and detection of THz arrays. The long coherence length comes with an unprecedented narrow linewidth. This is of particular interest for spectroscopic applications, the field in which THz research has perhaps the highest impact. We point out that CW spectroscopy systems may potentially be more compact, cheaper, and more accurate than conventional pulsed systems. These features are attributed to telecom-wavelength compatibility, to excellent frequency resolution, and to their huge spectral density. The paper concludes with prototype experiments of THz wireless LAN applications. For future telecommunication systems, the limited bandwidth of photodiodes is inadequate for further upshifting carrier frequencies. This, however, will soon be required for increased data throughput. The implementation of telecom-wavelength compatible photomixing diodes for down-conversion of an optical carrier signal to a (sub-)THz RF signal will be required.
 [doi:10.1063/1.3552291]

TABLE OF CONTENTS

a)Electronic addresses: psascha@mrl.ucsb.edu and lwan@mail.tsinghua.edu.cn

I. INTRODUCTION

Terahertz (THz) radiation covers the frequency range between 100 GHz and 10 THz in the spectrum of electromagnetic waves. For a long time, this range of frequencies was called the THz gap, since it had not been possible to bridge the high-frequency limit of RF sources with the low-frequency end of optical emitters. Within the last decade, however, efforts to build suitable sources and detectors have drastically closed the gap. The THz frequency range became a very active field of research, attributed to the wide range of potential applications: In contrast to microwaves, imaging of macroscopic objects with rather high spatial resolution is possible with THz radiation due to the (sub-)mm wavelength. Moreover, many optically opaque materials such as common clothing,[1] paper (envelopes),[2] or many kinds of plastics[3] are transparent to THz radiation. Thus, imaging in combination with these properties implies the possibility to obtain pictures of objects hidden below such materials.[4] Using very short pulses allows for easily gaining very accurate information about the distance and the shape of an object. This is achieved by measuring the time of flight of the reflected pulse[5] (THz time-domain systems). Coherent continuous wave (CW) detection schemes were demonstrated and also allow for depth resolution.[6]

The THz range covers the energy range for molecular rotation of polar molecules and librations of macromolecules. Because rotation spectra with many narrow characteristic lines in this frequency range represent highly selective fingerprints of molecules,[7–9] including (large) organic molecules,[10–13] high-resolution THz absorption spectroscopy is very appealing for chemical composition analysis, even down to the parts-per-million range.[14] In combination with imaging techniques—in particular by transmission or reflection scanning—the strong spectral sensitivity of the absorption allows for pictures that isolate certain materials or substances,[15] a property of interest to medicine, biology, and industrial production processes.[16] It is obvious that the features of THz radiation just mentioned are of particular interest to security applications. They allow identification of persons carrying concealed weapons, even nonmetallic threats,[4] for example explosive[17,18] or chemical or biological agents.[19] For this reason, significant sponsorship of THz technologies followed after the terrorist attacks on 11 September 2001.

Another wide field of interesting applications of THz radiation is related to the fact that the cosmic background radiation density, $u(\lambda)$, peaks in the THz range[20,21] [the cosmic background blackbody temperature of $T_{BB} = 2.725$ K implies a peak of $u(\lambda)d\lambda$ at 1.063 mm (281.91 GHz); in frequency representation, $u(v)dv = u(\lambda)(\partial\lambda)/(\partial v)dv$ peaks at 160.4 GHz, corresponding to 1.87 mm]. Tunable CW THz sources can be used as local oscillators for heterodyne detection of cosmic radiation. A particular advantage results for phase-locked coherent detection within an array of antennas, as will be discussed in Sec. III B 2.

In the past years, the THz gap has been narrowed from both sides with various purely electronic RF sources[22] and purely optical emitters,[23,24] but also by combining optical with RF techniques, e.g., the concept of photomixing.[25] In terms of the generated THz radiation we have to distinguish between short-pulse broadband, long-pulse quasi-CW, and coherent CW emitters. For many possible applications, short pulses of broadband THz radiation are sufficient, or even sometimes advantageous, for instance for the above mentioned monitoring purposes.

On the RF side, Backward-Wave Oscillators (BWO) are able to provide tunable narrowband CW THz radiation.[26] Rather high power levels up to tens of mW and frequencies up to 1.45 THz for BWOs[27] have been demonstrated. They are, however, heavy, bulky, and expensive. They require high magnetic fields, in addition to a vacuum. More recently, CW THz emitters based on semiconductor electronics have been demonstrated. Resonant tunneling diodes have reached a maximum frequency of 0.712 THz at a power level of 0.3 μW.[28] Multipliers (doubler, tripler) based on Gunn diodes, impact ionization avalanche transit time (IMPATT) diodes, or heterostructure barrier varactor (HBV) diodes, cover the range up to or greater than 1.9 THz, with still several μW of power available.[22] Significantly higher power levels have been demonstrated at lower frequencies. Cryogenic Josephson junction–based devices[29] have almost reached the μW level at frequencies up to 850 GHz.[30]

On the optical end there has been remarkable progress in the field of quantum cascade lasers (QCLs). After the first demonstration of THz-QCLs emitting at 4.4 THz in 2002 by Tredicucci *et al.*[31] and at 1.6 THz by Faist *et al.*[32] in 2006, the emission frequency was able to be red-shifted down to 0.95 THz.[23] Also the operation temperature range has been extended to 168 K[33] for (long) pulse operation at 2.9 THz.

Purely optical approaches include difference mixing of two laser beams of frequencies $\nu_+ = \nu_0 + \nu_{THz}/2$ and

$\nu_- = \nu_0 - \nu_{THz}/2$ in a dielectric (or semiconducting) medium with a (relatively) large second-order susceptibility,[34–37] $\chi^{(2)}$. The nonlinear interaction results in a polarization of the medium with frequency ν_{THz}, which, in turn, generates a THz wave. This process is usually called "optical rectification" as it generates a signal with the (relatively low) THz frequency from the beat of the two optical frequency (NIR or IR) laser beams. It requires laser intensities of the order of several hundred W/cm^2 in order to yield reasonable THz power, as the best $\chi^{(2)}$ values are in the range of 25.2 pm/V (in $LiNbO_3$,[38] for example). Therefore, CW operation is fairly difficult and would require phase-matching over extremely long interaction lengths. Thus, these sources are usually operated with pulses in the 10 ns range. The pulse length τ_{pls} imposes a limit on the minimum linewidth $\Delta\nu_{THz}$ of the THz signal. As a result of the Fourier limitation (or, alternatively, the uncertainty relation) $\Delta\nu_{THz}\tau_{pls} \geq 1/(4\pi)$, very short pulses diminish the spectral purity of the THz signal. An elegant method for optical rectification requires only a single pulsed laser. This method uses parametric interactions in Raman-active, nonlinear crystals.[39,40] The interaction with phonon-photon polaritons first generates an optical idler wave at $\nu_I = \nu_P - \nu_{THz}$ that mixes with the pump beam[41] in a subsequent $\chi^{(2)}$ process and yields THz photons where the phase-matching condition $\vec{k}_{THz} = \vec{k}_P - \vec{k}_I$ is fulfilled.[24]

The mixing approach discussed above is based on the nonlinear THz-periodic polarization of dielectrics or semiconductors. The elastic electron displacement s_{pol} associated with this polarization follows the intensity beat of the two laser beams with the difference frequency $\nu_+ - \nu_- = \nu_{THz}$. The electric field emitted by these induced atomic THz dipoles $p_{THz}(t) = es_{\mathrm{pol}}(t)$ is proportional to their second time derivative, i.e.,

$$E_{THz} \propto \frac{d^2 s_{\mathrm{pol}}(t)}{dt^2}. \tag{1}$$

The displacement amplitudes s_{pol} of the THz dipoles, however, are very small compared to the lattice spacing a_0 even at high laser intensities. This explains the small values of $\chi^{(2)}$ and the long interaction lengths required for the transformation of two optical signals into a THz signal, although all the lattice sites are contributing coherently when the phases are well matched. The optical mixing concept can, however, be extended to a much more efficient process. This process is based on the THz-periodic generation of free carriers by absorption of the two beating laser beams. The free electrons and holes are subsequently accelerated by a suitably chosen DC electric field over distances s_{eh} which may exceed the lattice constant a_0 by orders of magnitude. Each absorbed photon results in the generation of a transient free electron-hole dipole $p_{THz}(t) = es_{eh}(t)$ which emits a broadband THz field

$$E_{THz}(t) \propto \frac{d^2 s_{pol}(t)}{dt^2}. \tag{2}$$

Due to the THz-periodic generation of these electron-hole dipoles, only the narrowband THz component with the difference frequency $\nu_+ - \nu_- = \nu_{THz}$ survives the phase-coherent superposition of these broadband THz fields. This approach is called photomixing. It should be noted that, in principle, all incident photons can be absorbed within a few μm, due to the large absorption coefficient ($\alpha \sim 1\ \mu m^{-1}$) of semiconductors for photon energies $h\nu_0$ above the bandgap energy E_G. Therefore, the radiation emitted per incident photon is expected to be large, yielding much larger THz power at a given optical power as compared to the $\chi^{(2)}$ mixing approaches. It should be possible to generate coherent CW THz radiation with high conversion efficiency in a thin layer and an illuminated area with dimensions on the order of (or even larger than) the THz wavelength without phase-matching problems (large area emitter, LAE). This will be discussed in Sec. II A 2 and in more detail in Sec. II F. This direct generation of THz radiation by accelerated photogenerated carriers within a large area has been demonstrated first for the case of carrier generation normal to the surface by ultrashort single laser pulses. These experiments had a more or less common design with a femtosecond (fs)-laser pulse incident to the sample under a certain angle. The THz pulse was observed in mirror reflection geometry. This concept was used to study physical concepts like Bloch oscillations[42] or quantum beats in optical transitions to neighboring Wannier–Stark levels and Bloch gain in artificial superlattices.[43,44] Other groups studied the "velocity overshoot" in the coherent ballistic transport of carriers simultaneously generated by fs-laser pulses,[45] or the transient current generated in the surface layer of III-V semiconductors due to surface band bending,[46] or due to the Dember effect.[47] The THz power observed in these experiments was relatively small due to the fact that the effective dipoles were oriented normal to the surface. As a result of the large refractive index of the semiconducting materials ($n_{\mathrm{opt}} \approx 3.5$) the emission intensity was at least reduced by a factor of $\sin^2 \Theta_{\mathrm{tot}} = (1/n_{\mathrm{opt}})^2 \approx 0.1$ (where Θ_{tot} is the critical angle for total reflection). Strongly increased THz power has been achieved by implementing transient surface currents in III-V-semiconductors by a surface-parallel magnetic field oriented normal to the incident laser beam. This induces a surface-parallel component of near-surface carrier transport due to the Lorentz force.[48–50]

A simpler way to generate strong in-plane components of the carrier acceleration and, hence, strong in-plane components of the THz fields, is with the application of a DC bias to large area coplanar metallic contacts. This creates a strong in-plane electric field. The THz power is emitted with high efficiency into the semiconductor in a direction normal to the surface.[51,52] The radiated electric field strength is proportional to the time derivative of the transient current,

$$E_{THz} \propto \frac{dI_{THz}}{dt} = \frac{d(G(t)U_{DC})}{dt}, \tag{3}$$

where $G(t)$ is the optically-induced transient conductance of the semiconductor due to the generation of electrons and holes by absorption. The conductivity can be modulated either by a single, very short (fs) laser pulse [$\tau_{pls} < 1$ ps $= (1\ \mathrm{THz})^{-1}$] or by mixing two lasers with $\tau_{pls} \gg 1$ ps (or even CW) that are frequency offset by the desired THz frequency. For the latter case,

$$\frac{dI_{THz}}{dt} \propto \cos(2\pi(\nu_+ - \nu_-)t + \varphi), \tag{4}$$

provides a single frequency, Fourier-limited THz signal similar to optical rectification.

By excitation with single ~50 fs pulses, peak THz field amplitudes of 36 kV/cm have recently been reported.[53]

A much higher conversion efficiency is achieved if the purely "opto-electronic" photomixing approach is replaced by a combination with RF techniques. The photogenerated current, $I(t)$, is fed into a suitably designed antenna. The advantage of an antenna is that its length can be matched to the wavelength, i.e., it is resonant to the THz frequency. The emission efficiency of the Hertzian dipole of LAEs, however, is $\propto (s_{eh}/\lambda)^2$. In the case of transient dipoles and Bloch oscillators, $s_{eh} \approx 100$ nm, providing $(s_{eh}/\lambda_{\text{eff}})^2 \approx 10^{-6}$ (with $\lambda_{\text{eff}} = \lambda_0/n_{\text{eff}} = 300\ \mu\text{m}/2.6 = 115\ \mu\text{m}$) at 1 THz. The effective dipole length for large area photomixers can be significantly enlarged by using an array of phase-coherent, parallel metal-semiconductor-metal (MSM) junctions as reported by researchers in Refs. 51–53 and further discussed in Sec. II F. As an example of achievable power levels with antenna-based devices, we discuss in the following emitters based on GaAs as this is the most widely used material for photomixing. The ideal THz output power of a photomixer with antenna is

$$P_{THz} = \frac{1}{2} R_A I_{THz}^2 = \frac{1}{2} R_A \left[\frac{eP_L}{h\nu}\right]^2. \quad (5)$$

Here, $R_A \sim 20 - 100\,\Omega$ is the radiation resistance of the antenna. The quadratic scaling, $P_{THz} \sim P_L^2$, with the laser power P_L, also applies to THz generation in materials with nonlinear $\chi^{(2)}$ susceptibility. In the latter case, however, the quantum mechanical rule of photon number conservation, i.e., the Manley–Rowe rule, applies.[41] Only one secondary (i.e., THz) photon per primary photon can be obtained. The "detour" via generation of a photocurrent, circumvents the Manley–Rowe limit. Conservation laws require that one photon generates one electron-hole pair. The radiated energy, however, does not stem from the incident photons, but rather from the accelerating (external) electric DC field. One electron-hole pair can emit many THz photons. Photomixing can be much more efficient than $\chi^{(2)}$ mixing at THz frequencies: Eq. (5) implies that the Manley–Rowe limit is already met by an ideal photomixer with a typical radiation resistance of $R_A = 70\,\Omega$ at 1 THz ($h\nu = 4$ meV) when pumped at 850 nm (1.45 eV, 354 THz) with a laser power of only 1.6 mW. This yields a THz power of 46 μW and an efficiency of 3%. This example demonstrates that extremely high conversion efficiencies may be obtained at very moderate laser power. At low frequencies (100 GHz), where the photomixer performance is close to ideal, CW output powers of 20 mW[54] could be demonstrated using InGaAs/InP based devices and 1550 nm lasers, exceeding the Manley–Rowe limit by orders of magnitudes. Although the actual conversion efficiency of antenna-based THz emitters remains typically well below the ideal value—for reasons which will be discussed in Sec. II B 1—most of the THz work has been performed with these kinds of sources, either using fs excitation or CW operation.

Most of the progress in the field of THz research has been documented in a significant number of excellent reviews,[16,24,56–58] including books.[59] This is particularly true for the case of broadband THz investigations using fs-laser pulses and for CW THz research using photomixing for the period up to the year 2005. We note, however, that recent significant progress has been made specifically in the fields of CW photomixing and large area emitters (LAEs). Development of new sources, as well as applications of the particular features of THz radiation generated by CW photomixers, like huge bandwidth, high coherence, and interference properties, are not included in those reviews. Apart from that, there are also several more fundamental issues—such as a comparison of different photomixing techniques—which have not received adequate attention so far. Therefore, one of our goals in this review is a detailed discussion of these points, which we consider quite important for the future direction of activities in the field of THz radiation. In particular, we will cover the issue of large area emitters (LAE) versus antenna-based emitters (AE).

Our review is organized as follows. Sec. II A illustrates two approaches to generating THz radiation by photomixing, LAEs and AEs. The subsequent section describes the photomixing process in detail for the example of antenna-based emitters. Different realizations of photomixers using 850 nm or telecom wavelength lasers will be given in Secs. II C and II D for AE emitters and in II F for the LAE concept. Sec. III describes several applications for CW photomixers. Special attention is devoted to the high coherence of continuous-wave THz radiation that allows for constructing mutually coherent emitters in an array configuration. In Sec. III C we show that the narrow linewidth offers high resolution in spectroscopy systems. Several examples will be given, including the spectroscopy of artificial, photonic atoms, namely whispering gallery mode resonators. The last part of Sec. III shows that InGaAs-based photomixers are compatible with current communication technology and can be used for future wireless LAN applications. The paper concludes with a summary in Sec. IV.

II. THz GENERATION BY PHOTOMIXING

A. Principles of photomixing: Antenna-based versus large area emitters

CW or quasi-CW THz generation by photomixing is based on the THz-periodic generation of electrons and holes in semiconductors by absorption of two interfering laser beams of frequencies $\nu_\pm = \nu_0 \pm \nu_{THz}/2$. The interference results in intensity modulation of the laser beams with the frequency ν_{THz} and, hence, the THz-periodic carrier generation. The emission of THz radiation originates either directly from the (phase-coherent) acceleration of the individual photogenerated carriers $\vec{a}_i(t) = d\vec{v}_i/dt$, typically within a large area as schematically depicted in Fig. 1(a). Alternatively, it originates from the collective current of these carriers $I_{THz}(t)$, generated within a very small area and being fed into an antenna (of length L_A) as shown in Fig. 1(b). We name these two emitter types large area emitter (LAE) and antenna-based emitter (AE).

The quadratic relation between laser power and THz power for AEs in Eq. (5), $P_{THz} = \gamma P_L^2$, applies also for LAEs for constant dimensions, L_x, L_y. However, AEs and LAEs

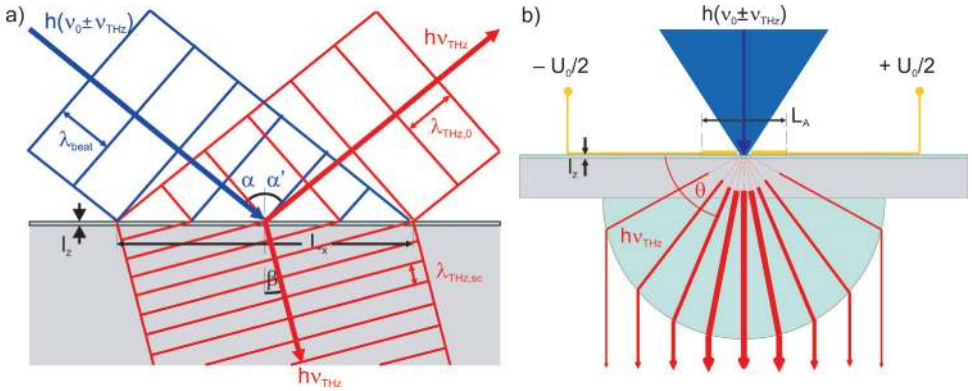

FIG. 1. (Color online) Two collimated beams with frequencies $\nu_{\pm} = \nu_0 \pm \nu_{THz}/2$ are generating free electrons and holes within a thin layer of thickness l_z. (a) Schematic diagram of photomixing in a large area emitter (LAE). The lateral dimensions L_x, L_y are comparable to or larger than the THz wavelength λ_{THz}. The contacts for the external bias generating a surface-normal or in-plane DC electric field E_{DC} are not shown. The phase-coherent THz radiation is emitted into air in the direction of the reflected optical beam and into the semiconductor under the angle β according to Snellius's law. (b) Schematic diagram of photomixing in an antenna emitter (AE). The two laser beams are focused onto a small area device. The external bias applied to the arms of the antenna generates a DC electric field, E_{DC}, which drives the THz periodic photocurrent, fed into the antenna of length L_A. The THz radiation is emitted mostly into the semiconductor by the antenna and is collimated by a hyperhemispherical (silicon) lens.

differ strongly with regard to the pattern of the emitted radiation field as well as the scaling factor, γ. Therefore, we will discuss the two cases separately.

1. Antenna emitter (AE)

We begin with the AE [Fig. 1(b)], the version most commonly used for THz photomixers. In the AE, laser beams are focused onto an area of the semiconductor with dimensions L_x and L_y much smaller than the THz wavelength, λ_{THz} (300 μm for 1 THz in air). Assuming the same polarization and electric field amplitude $E_+ = E_- = E_0$ of the two laser beams, their superposition yields

$$\begin{aligned} E(t) &= E_0 \cdot \exp(i\omega_+ t) + E_0 \cdot \exp(i\omega_- t) \\ &= E_0 \cdot \exp(i\omega_0 t) \cdot 2\cos(\omega_{THz} t/2), \end{aligned} \tag{6}$$

where we have substituted the frequencies ν with the corresponding angular frequencies $\omega = 2\pi\nu$. The total laser power responsible for carrier generation, $P_{L,0} = P_{L,+} + P_{L,-}$ is modulated according to

$$\begin{aligned} P_L(t) \sim 4E_0^2 \cos^2(\omega_{THz} t/2) = 2E_0^2[1 + \cos(\omega_{THz} t)] \\ \Rightarrow P_L(t) = P_0[1 + \cos(\omega_{THz} t)]. \end{aligned} \tag{7}$$

If the power and/or the polarization of the two laser beams differ, $\vec{E}_+ \neq \vec{E}_-$, the modulation amplitude is reduced and Eq. (7) is replaced by

$$P_L(t) = P_+ + P_- + 2\sqrt{P_+ P_-}\,\frac{\vec{E}_+ \circ \vec{E}_-}{|E_+| \cdot |E_-|}\cos(\omega_{THz} t). \tag{8}$$

As a result of the large optical absorption coefficient of semiconductors at photon energies above the bandgap energy, $h\nu_0 > E_G$, the electron-hole pair generation takes place within only a few μm, i.e., within a very thin layer compared to λ_{THz}. Therefore, phase matching is not an issue in this mixing process, in contrast to the $\chi^{(2)}$ process mentioned in the introduction, where interaction lengths have to be much larger than λ_{THz}. Electrons and holes are separated by a built-in field (of a p-i-n junction, for example) or by an external field due to a DC bias. The resulting current contains a THz component due to the periodic modulation of the carrier generation rate. The device is connected to an antenna that converts the AC current into THz radiation. The (ideally) emitted power is given by the simple expression

$$P_{THz}^{AE} = \frac{1}{2} R_A I_{THz}^2 \leq \frac{1}{2} R_A \left(\frac{eP_{L,0}}{h\nu_0}\right)^2, \tag{9}$$

as shown in the introduction. The scaling factor R_A is the radiation resistance of the antenna. It is proportional to the wave impedance, $Z = \sqrt{\mu_0\mu_{\text{eff}}/(\epsilon_0\epsilon_{\text{eff}})} = Z_0\sqrt{\mu_{eff}/\epsilon_{eff}}$ (for nonmagnetic materials, $\mu_{\text{eff}} = 1$), with the vacuum impedance $Z_0 = \sqrt{\mu_0/\epsilon_0} = 377\ \Omega$.

Due to the large dielectric constant of semiconductors ($\epsilon_{sc} \approx 13$ for GaAs), the antenna will emit most of the power toward the substrate. Its wave impedance, $Z = Z_0/\sqrt{\epsilon_{sc}} = 377\,\Omega/3.6 \approx 104\ \Omega$, is much smaller than that of air, with $Z = Z_0$. The effective wave impedance of an antenna on an air–semiconductor interface is $Z_0/\sqrt{\epsilon_{\text{eff}}}$ with $\epsilon_{\text{eff}} = (\epsilon_{sc} + 1)/2$. A typical value for the impedance of an ideal, self-complementary antenna is $Z_0/(2\sqrt{\epsilon_{\text{eff}}}) \approx 72\ \Omega$.[60] For other types of antennas or nonideal performance, the real part of the antenna, R_A, strongly depends on the antenna design. Antenna layouts will be further discussed in Sec. II B 2.

The maximum value in Eq. (9) is only achieved for an ideal responsivity $\mathcal{R}^{id}$ of the emitter, $\mathcal{R} = I/P_L = e/(h\nu_0)$. In this case, each electron-hole pair generated by an incoming photon fully contributes to the THz current, I_{THz}. In Sec. II B we will see that in all AEs based on photoconductors, the responsivity is far from ideal, $\mathcal{R} \ll \mathcal{R}^{id}$. Values close to $\mathcal{R}^{id}$ can only be achieved in p-i-n photodiodes. At higher THz frequencies, the THz power is reduced in both photoconductor and p-i-n photodiode–based AEs for two reasons: The finite capacitance of the device is parallel to the radiation resistance of the antenna, yielding an "RC roll-off." The finite transport time of the photogenerated carriers creates a "transport-time

roll-off." As we will show in Sec. II B 1, for both roll-off contributions, the THz power decreases as v^{-2} above the respective 3 dB frequency. Thus, key tasks for the design of AEs consist in achieving large responsivities and high 3 dB frequencies. At the same time, the photomixer should tolerate a high laser power as $P_{THz} \sim P_L^2$. We will learn that the best values obtained so far refer to p-i-n–based "uni-traveling-carrier" (UTC) devices. At 100 GHz, a power of $P_{THz} = 20$ mW was observed[54] at a photocurrent of 25 mA. At 0.914 THz a THz power of 25 μW has been achieved with traveling wave photomixers.[55,61]

2. Large area emitter (LAE)

In the LAE [see Fig. 1(a)], the dimensions of the area illuminated by the two collimated laser beams are comparable to or even much larger than the THz wavelength. Therefore, the spatial phase modulation of the incoming optical beam and the generated THz beam has to be taken into account. The interference of the radiation emitted by the elementary dipoles occurs in the far field. Assuming the same polarization and electric field amplitude E_0, and also the same orientation $\vec{e}_k$ of the wave vectors $\vec{k}_\pm = \vec{e}_k(k_0 \pm 0.5\, k_{THz})$, with $k_{THz} = 2\pi/\lambda_{THz}$, the superposition of the two laser beams yields

$$E(r,t) = E_0 \exp[i(\vec{k}_+ \circ \vec{r} - \omega_+ t)] + E_0 \exp[i(\vec{k}_- \circ \vec{r} - \omega_- t)] = 2E_0 \exp[i(\vec{k}_0 \circ \vec{r} - \omega_0 t)] \cos\left(\frac{\vec{k}_{THz} \circ \vec{r} - \omega_{THz} t}{2}\right). \tag{10}$$

With the geometry depicted in Fig. 1(a), we get $\vec{k}_0 = (k_0 \sin\alpha, 0, k_0 \cos\alpha)$. The laser intensity is modulated in the x-direction according to

$$I_L(x,t) = \frac{P_{L,0}}{L_x L_y}[1 + \cos(k_{THz,x} x - \omega_{THz} t)], \tag{11}$$

with $k_{THz,x} = (2\pi/\lambda_{THz})\sin\alpha$ and $P_{L,0}$ the sum of the two laser powers. The carrier generation appears within a few μm below the surface, i.e., $\vec{r} = (x, y, z_i \approx 0)$, and will follow the spatial and temporal phase modulation of the optical beams. An electric field, $\vec{E}_{DC}$, will induce an acceleration of the carriers. The field may be applied in-plane (as is typical in photoconductors) or normal to the surface. An electron-hole pair generated in a finite volume element at $\vec{r}_i = (x_i, y_i, z_i \approx 0)$ at the time t' will generate electromagnetic "quasidipole" radiation during a period $t' < t < t' + \tau_t$, where the acceleration $\vec{a}_i(x_i, y_i, t) = d\vec{v}_i(x_i, y_i, t)/dt$ is parallel to $\vec{E}_{DC}$. The transport time τ_t stands typically for either a "(ballistic) transport time" or the "carrier lifetime." They are comparable to typical THz periods $T_{THz} = \nu_{THz}^{-1}$ and are in the sub-picosecond (ps) range. Both cases will be discussed in detail in Secs. II B 1 and II F. For a simple estimate of the output intensity, we assume a harmonic single-cycle charge motion with $\omega_{THz} = 2\pi/\tau_t$ of a free electron with effective mass m_e. The contribution of holes would be much smaller due to their larger effective mass and will be neglected in the following. For the time dependence of the position, $\vec{s}(t)$, we get

$$\vec{s}(t) = \frac{e\vec{E}_{DC}}{\omega_{THz} m_e}\{(t - t') - \omega_{THz}^{-1} \sin[\omega_{THz}(t - t')]\} \tag{12}$$

This corresponds to a THz-current $I_e = e_0 \nu_{THz}$ in a dipole of length $l_0 \approx 2s_0$ with $s_0 = eE_{DC}/(m_e\omega_{THz}^2)$, and a dipole moment of $d_0 = el_0 = 2e^2E_{DC}/(m_e\omega_{THz}^2)$. For a free electron in InGaAs with $m_e = 0.041m_0$ at $\nu_{THz} = 1$ THz and $E_{DC} = 10$ kV/cm, this gives a dipole length of $l_0 = 217$ nm. The total power emitted by such an "elementary Hertzian dipole" is given by the expression on page 155 in Balanis:[60]

$$P_{THz} = \sqrt{\frac{\mu_0}{\epsilon_0 \epsilon_{\text{eff}}}} \cdot \frac{\pi}{3} \cdot \frac{l_0^2 I_e^2}{\lambda_{THz}^2}. \tag{13}$$

Introducing the dipole radiation resistance,

$$R_{dip} = \frac{2P_{THz}}{I_e^2} = (2\pi/3)\sqrt{\frac{\mu_0}{\epsilon_0\epsilon_{\text{eff}}}} \cdot (n_{THz} l_0/\lambda_{THz,0})^2 = \frac{2\pi Z_0 \sqrt{\epsilon_{\text{eff}}}}{3}(l_0/\lambda_{THz,0})^2, \tag{14}$$

we can write the radiated THz power

$$P_{THz} = \frac{1}{2} R_{\text{dip}} I_e^2 = \frac{1}{2} \cdot 789\ \Omega \cdot \sqrt{\epsilon_{\text{eff}}}(l_0/\lambda_{THz,0})^2 \cdot I_e^2. \tag{15}$$

For our example with $l_0 = 217$nm at 1 THz, and $\epsilon_{\text{eff}} = 7$ we get $R_{\text{dip}} = 1.1 \cdot 10^{-3}\ \Omega$.

In contrast to LAEs, AE emitters usually provide a radiation resistance in the range from 20 Ω to 70 Ω. As a consequence, small dipoles represent much less efficient emitters for a given current [see Eq. (15)], as compared to dipole antennas with a dipole length comparable to $\lambda_{THz,0}$ in Eq. (9).

We will first consider the emission of an illuminated area, which is small enough that any spatial phase shifts can be neglected ($L_x, L_y < \lambda_{THz}/5$, for example). In this case, all the parallel elementary dipoles emit coherently. In the ideal case, all the incoming laser power P_L will be absorbed within the area $L_x \times L_y$, generating a total of $dN/dt = (P_L/h\nu_0)$ electron-hole pairs per second. With our previous assumption of $\tau_t = 1/\nu_{THz}$ this implies that the current of one dipole $I_e = e\nu_{THz}$ from Eq. (15) is now multiplied by the number of simultaneously participating electron-hole pairs. This provides a total current of $I = NI_e$, representing coherently oscillating dipoles. The emitted power is

$$P_{THz}^{LAQD} = \frac{1}{2} R_{\text{dip}} (NI_e)^2 = \frac{1}{2} R_{\text{dip}} \left(\frac{eP_{L,0}}{h\nu_0}\right)^2, \tag{16}$$

and for our specific example

$$P_{THz}^{LAQD}(1\text{THz}) = \frac{1}{2} \cdot 789\ \Omega \sqrt{\epsilon_{\text{eff}}} \left(\frac{l_0}{\lambda_{THz,0}}\right)^2 \cdot \left(\frac{eP_{L,0}}{h\nu_0}\right)^2 = \frac{1}{2} \cdot 1.1 \cdot 10^{-3}\ \Omega \cdot \left(\frac{eP_{L,0}}{h\nu_0}\right)^2. \tag{17}$$

The superscript "LAQD" stands for "large area quasidipole." Equation (17) for the LAQD differs from Eq. (9) for the AE formally only by the 4 orders of magnitude lower radiation resistance. Nevertheless, LAQDs are attractive because of the

much larger active area for carrier generation, allowing for much higher currents and, consequently, higher laser power P_L. As mentioned in the concluding remarks of the section on AEs, the maximum theoretical THz power achieved in AEs so far was limited to $P_{THz,AE} < 24\,\mu$W close to 1 THz. For LAEs the optical power P_{opt} can be distributed over a much larger area. Assuming a laser power of $P_{L,0} = 0.5$ W at $h\nu_0 = 0.8$ eV yields $P_{THz}^{LAQD} = 210\,\mu$W at 1 THz. For the area $A = L_x \times L_y = [\lambda_{THz,0}/(5n_{\text{eff}})]^2 = 23\,\mu\text{m} \times 23\,\mu\text{m}$, the thermal load $P_L/A = 95\text{kW/cm}^2$ should not impose a limit. Although we assumed an idealized case of free electrons in the semiconductor with ballistic acceleration and neglected any deceleration due to scattering of the carriers, we will see in Sec. II B 1 and II D that such conditions can be approximately met in p-i-n diodes. In a pulsed experiment with photoconductive LAE emitters by Beck *et al.*,[53] an optical to THz conversion efficiency of $\eta = 2 \times 10^{-3}$ was obtained (we will explain this experiment in detail in Sec. II F 1). This even exceeds the conversion efficiency of this CW example with $\eta = 210\,\mu\text{W}/0.5\text{W} = 4.2 \times 10^{-4}$.

So far we have only discussed the total THz radiation emitted into the 4π solid angle with the typical angular distribution of a dipole, assuming phase coherence within the whole illuminated area. In the far field, the angular distribution of the THz power emitted into the solid angle $d\Omega$ depends on the angle θ between the wave vector $\vec{k}_{THz}$ and the dipole $\vec{d}_0 || \vec{E}_{DC}$ according to

$$dP_{THz}^{LAE} \sim \sin^2\theta d\Omega \tag{18}$$

With increasing size of the illuminated area the spatial phase coherence will play an increasingly important role. For an area of dimensions $L_x, L_y \gg \lambda_{THz}/5$ constructive interference of all the microscopic THz field contributions, with the spatial and temporal phase modulation $\cos(k_{THz,x}x_i - \omega_{THz}t)$ given by Eq. (11), will persist only for two directions: The waves that propagate into air under the reflection angle $\alpha' = -\alpha$ with wave vector $\vec{k}_{THz,0} = (k_0 \sin\alpha, 0, -k_0 \cos\alpha)$, and the other propagating in the semiconductor under the refraction angle according to Snellius's law $\sin\beta = \sin\alpha/n_{THz}$, with wave vector $k_{THz,sc} = (n_{THz}k_0 \sin\beta, 0, n_{THz}k_0 \cos\beta)$, as shown in Fig. 1. For a deviation δ from the angles α' and β, the THz intensity decreases due to destructive interference. The larger the dimensions of the illuminated area, the faster the intensity decreases to zero with increasing δ. Specifically, two parallel collimated incoming laser beams with a diameter much larger than the THz wavelength will again generate collimated THz beams of comparable diameter propagating along $\vec{k}_{THz,0}$ and $\vec{k}_{THz,sc}$. At the same time, the intensity emitted in other directions approaches zero. Such a radiation pattern is certainly very appealing, as it allows the use of very simple optics for LAEs. At the same time, LAEs also require much less demanding processing procedures for their fabrication as compared to most AEs. A detailed discussion of the THz emission by LAEs, the radiation efficiency and angular pattern, and the dependence on design parameters will be presented in Sec. II F.

B. Basic theoretical considerations of antenna-based emitters

1. Transport and RC roll-off

Antenna-based photomixers can be classified into photoconducting and p-i-n–based THz emitters as schematically depicted in Fig. 2. Our goal for the following discussion is to show what the two kinds of mixers have in common and where they differ from each other regarding their high-frequency performance. For simplicity, we will focus on CW (or quasi-CW) operation. The general results, however, will also apply to operation with sub-ps pulses.

For both photoconductors and p-i-n–based emitters, the absorption of the two laser beams with frequencies $\nu_\pm = \nu_0 \pm 1/2\nu_{THz}$ results in an electron-hole pair generation rate of dN/dt modulated with the beating laser power $P_L(t)$, according to Eq. (7) and Eq. (8). The generation rate in an absorbing layer with thickness d, absorption coefficient α, and a surface reflection coefficient R is given by the product of incident photons per second, $P_L(t)/(h\nu_0)$ and the external quantum efficiency, η_{ext},

$$\frac{dN(t)}{dt} = \eta_{\text{ext}} \frac{P_L(t)}{h\nu_0}, \tag{19}$$

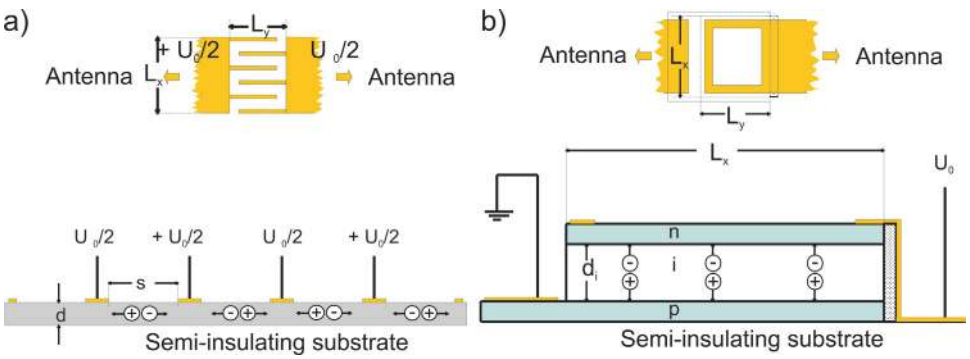

FIG. 2. (Color online) (a): Photoconductive mixer. The absorbing layer of thickness d (typically on the order of 1 μm) is deposited on a semi-insulating substrate. It consists of a semiconductor with a high density of intentionally introduced recombination centers, causing extremely short electron and hole recombination lifetimes in the sub-ps range. The photogenerated carriers travel in-plane toward the coplanar contacts under the influence of the bias U_{ext}, applied between the antenna arms. Their drift length is much smaller than the contact separation, s. (b): p-i-n–diode photomixer. A mesa with the dimensions L_x, L_y, is lithographically defined by etching an epitaxially grown (double-hetero) p-i-n layer structure. It is connected to the antenna arms by ohmic contacts to the highly-doped p- and n-layer. The top contact has an optical window, as indicated in the inset.

with

$$\eta_{\text{ext}} = (1-R)(1-\exp^{-\alpha d}). \tag{20}$$

The external quantum efficiency is the ratio of incident and absorbed photons. Specifically, if the two beams have the same polarization and the same power $P_{L,0}/2$, the generation rate is fully modulated according to Eq. (7),

$$\frac{dN(t)}{dt} = \eta_{\text{ext}} \frac{P_{L,0}}{h\nu_0}[1+\cos(\omega_{THz}t)]. \tag{21}$$

In the case of photoconducting emitters, the carriers are generated in a quasi-intrinsic semiconducting material containing a high density of intentionally introduced near-midgap recombination centers. As a result, this material exhibits a negligibly small dark conductivity and extremely short carrier recombination time τ_{rec}. τ_{rec} is typically in the sub-ps range (the advantages of these short carrier recombination times will be discussed below). In order to absorb a major fraction of the penetrating laser power, the semiconductor is typically at least 1 μm thick [$\exp(-\alpha d) \approx 1/e$]. An external bias, U_{ext}, is applied to metal contacts on the semiconductor. This results in a current essentially parallel to the surface, $I(t)$, due to electrons and holes drifting toward the contacts. The contact widths and spacings are typically on the order of $w \approx 0.2\,\mu$m and $s \approx 2\,\mu$m. The total device area, A, is typically on the order of $10 \times 10\ \mu\text{m}^2$.

In p-i-n diode emitters, the electrons and holes are generated in or close to the intrinsic layer. They propagate normal to the surface toward the p- and n-doped layers due to the built-in field, U_{bi}/d_i, with d_i the length of the intrinsic layer and $U_{bi} \approx E_G/e$. This results in a photocurrent, $I(t)$. The built-in field may be modified (for various reasons discussed below) by an additional external DC voltage, U_{ext}.

In both emitter types, the goal is to obtain a large AC component of the photocurrent. Ideally, each photogenerated electron-hole pair contributes an elementary charge, e, to the photocurrent, i.e., the photocurrent is $I(t) = e[dN(t)/dt]$. To prevent destructive interference of carriers generated at different times, each photogenerated carrier should reach the contact or disappear by recombination within a transport time τ_t that is short compared to the THz period $T_{THz} = 1/\nu_{THz}$ (a detailed discussion of this requirement will be given in Appendix A). In this case, the AC component of the current is

$$I_{THz} = I_0 \cos(\omega_{THz}t). \tag{22}$$

The DC and AC amplitudes, I_0, are the same,

$$I_0 = \frac{eP_{L,0}}{h\nu_0}\eta_{\text{ext}} = I_0^{id}\eta_{\text{ext}}, \tag{23}$$

with $I_0^{id} = eP_{L,0}/(h\nu_0)$. The THz power emitted by an antenna with radiation resistance R_A corresponds to the expression Eq. (9) in the introduction, except for the reduction factor η_{ext}^2 that accounts for the external quantum efficiency:

$$P_{THz}^{id} = \frac{1}{2}R_A(I_0^{id})^2\eta_{\text{ext}}^2. \tag{24}$$

The external quantum efficiency [Eq. (20)] depends only on the photon frequency ν_0 as both α and R depend on ν_0, but not on the THz frequency ν_{THz}. The external quantum efficiency can approach unity if antireflection coating is used and the absorbing layers are sufficiently thick. Another option is to place the absorbing layer into a suitably designed resonant cavity.

Apart from the reduction of the actual THz power resulting from $\eta_{\text{ext}} < 1$, the power at higher THz frequencies in real AEs is reduced by two frequency dependent roll-off factors $\eta_t(\nu_{THz})$ and $\eta_{RC}(\nu_{THz})$. They reflect the nonideal transport and the influence of the device capacitance and antenna impedance, respectively.

In photoconductive devices, the relatively large separation of the coplanar contacts implies large transit times,

$$\tau_{tr} = s/\nu_{dr}, \tag{25}$$

with ν_{dr} the average drift velocity. Assuming $s = 2\,\mu$m and a drift velocity at the electron high-field saturation value $\nu_{dr} = \nu_{\text{sat}} = 10^7\,\text{cm/s}$, e.g., we obtain $\tau_{tr} = 20\,\text{ps}$. Such long transit times correspond to many THz periods ($1\ \text{THz}^{-1} = 1\,\text{ps}$, e.g.). They are, however, short compared to typical electron-hole recombination times τ_{rec}^i in standard intrinsic semiconductors. In such materials, all the photogenerated carriers would be collected at the contacts. The displacement current at the contacts at time t would include all carriers generated at earlier times $t - \tau_{tr} < t' < t$ at positions $\nu_{dr} \cdot (t-t') < s$ away from the contact. This results in a mostly destructive interference of the carrier contributions and will provide only a small AC current modulation, even for a fully modulated generation rate [Eq. (21)]. This scenario can be drastically improved if only those carriers significantly contribute to the current that have been generated during the past THz period or less. This can be achieved by artificially reducing the carrier lifetime to values $\tau_{\text{rec}} < T_{THz} \ll \tau_{\text{rec}}^i$. For instance, deep traps can act as electron and hole recombination centers. The rate of carriers arriving at the contacts at time t no longer includes all the carriers generated previously during the transit time τ_{tr}, but only those generated very recently at times $t' < t$ with an exponential weight of $\exp[-(t-t')/\tau_{\text{rec}}]$. For a material with $\tau_{\text{rec}} \ll \tau_{tr}$ we obtain for the photocurrent

$$I(t) = I_0^{id}\frac{1}{\tau_{tr}}\int_{-\infty}^{t}\exp^{-(t-t')/\tau_{\text{rec}}}[1+\cos(\omega_{THz}t')]dt'. \tag{26}$$

After introducing the time delay, $\tau = t - t'$, the photocurrent becomes

$$I(t) = I_0^{id}\frac{1}{\tau_{tr}}\int_{0}^{\infty}\exp^{-\tau/\tau_{\text{rec}}}\{1+\cos[\omega_{THz}(t-\tau)]\}d\tau. \tag{27}$$

Integrating Eq. (27) and using trigonometric addition theorems yields

$$I(t) = I_0^{id}\frac{\tau_{\text{rec}}}{\tau_{tr}}\left(\frac{1}{\sqrt{1+(\omega_{THz}\tau_{\text{rec}})^2}}\sin[\omega_{THz}t+\varphi]+1\right). \tag{28}$$

Equation (28) shows that the destructive interference with the phase-shifted contributions from earlier times yields a

"lifetime roll-off" with $|I_{THz^2}| \sim [1+(\omega_{THz}\tau_{\rm rec})^2]^{-1}$. The lifetime 3 dB frequency is

$$\nu_{\rm rec} = \frac{1}{2\pi\tau_{\rm rec}}. \tag{29}$$

In addition, a strong overall reduction of both DC and AC current by a factor of

$$g = \frac{\tau_{\rm rec}}{\tau_{tr}} \ll 1 \tag{30}$$

is found. This ratio is known as the "photoconductive gain,"[57] given by the ratio of carriers collected at the contacts to the total number of photogenerated carriers, $I = gI_0^{id}$. Substituting I_0^{id} of Eq. (24) for the AC amplitude from Eq. (28) we get a transport-related reduction factor of

$$\eta_{t,pc} = \left(\frac{\tau_{\rm rec}}{\tau_{tr}}\right)^2 \frac{1}{1+(\nu_{THz}/\nu_{\rm rec})^2} \tag{31}$$

for the THz power expected in photoconductive mixers due to nonideal transport. Equation (31) yields, for the low-frequency limit,

$$\eta_{t,pc}(\nu_{THz}) \to \left(\frac{\tau_{\rm rec}}{\tau_{tr}}\right)^2 = g^2. \tag{32}$$

In the high frequency range,

$$\eta_{t,pc}(\nu_{THz}) \to \left(\frac{\tau_{\rm rec}}{\tau_{tr}}\right)^2 \frac{1}{(2\pi\tau_{\rm rec}\nu_{THz})^2} \sim \nu_{THz}^{-2}, \tag{33}$$

turns out to be no longer dependent on the recombination lifetime $\tau_{\rm rec}$. At this point, one might come to the conclusion that short recombination lifetimes are counterproductive. They derogate the THz output at low frequencies and appear to be of no use in the high-frequency range. In our detailed discussion of photoconductive AEs in Sec. II C we will see, however, that short recombination lifetimes are crucial, but for other reasons. Short recombination lifetimes drastically reduce both electric energy dissipation by the photogenerated carriers and screening by space charge accumulation between the contacts at the required high laser power densities.

In p-i-n–based AEs, recombination plays a negligible role. Standard semiconductor material with recombination lifetimes in the nanosecond ns-range is used. Practically all photogenerated carriers reach the contacts, hence, $g = 1$. The finite transit time through the intrinsic layer, d_i, still introduces a roll-off. It can approximately be described by a reduction factor of the THz power of

$$\eta_{t,\rm pin}(\nu_{THz}) = \frac{1}{1+(\nu_{THz}/\nu_{tr})^2}. \tag{34}$$

The 3 dB frequency of this "transit time roll-off" depends on the details of the transport, as will be further discussed in the sections on p-i-n–based AEs (Secs. II D 2 and Appendix A). It can be approximately related to the transit time of the carriers through the intrinsic layer τ_{tr} by

$$\nu_{tr} \approx \frac{1}{2\tau_{tr}}. \tag{35}$$

In principle, very short transit times and, hence, high values of ν_{tr} can be achieved by making d_i short [see Fig. 2(b)] and/or by taking advantage of ballistic electron transport. The latter allows for average electron velocities much larger than the saturation velocity.

A second limitation for both types of photomixers at high frequencies arises from the RC time constant between the radiation resistance R_A of the antenna and the device capacitance C_{pm}, which are connected in parallel to the current source. The current reaching the antenna is reduced by a factor of $[1+i2\pi\nu_{THz}\tau_{RC}]^{-1}$. The THz power is reduced by the RC roll-off factor

$$\eta_{RC}(\nu_{THz}) = \frac{1}{1+(\nu/\nu_{RC})^2}, \tag{36}$$

with the RC 3 dB frequency

$$\nu_{RC} = 1/(2\pi\tau_{RC}) \quad \text{and} \quad \tau_{RC} = R_A C_{pm}. \tag{37}$$

As an example, for a radiation resistance of $R_A = 70\,\Omega$ and a desired RC 3 dB frequency of 1 THz, a value of $C_{pm} = 2.3$ fF is required.

The capacitance of coplanar finger contact structures [usually referred to as metal-semiconductor-metal (MSM) structures] as used for CW photoconductive AEs has approximately been calculated by Soole and Schumacher.[62] For a finger structure (finger width w, spacing s) with period $p = s + w$ and area $L_x L_y = A$ on a semiconductor with a dielectric constant ϵ_{sc}, the capacitance is

$$C_{pc} = \frac{K(\kappa)}{K(\kappa')}\epsilon_0(1+\epsilon_{sc})\frac{A}{p}, \text{ with} \tag{38}$$

$$\kappa = \tan^2[\pi w/(4p)], \quad \kappa' = \sqrt{1-\kappa^2} \tag{39}$$

$$K(\kappa) = \int_0^{\pi/2} \frac{1}{\sqrt{1-\kappa^2\sin^2\varphi}}\,d\varphi. \tag{40}$$

The quantities κ and κ' depend only on the ratio w/p. For a fixed ratio w/p, capacitance scales with A/p, similar to a plate capacitor. For typical values of $L_x = L_y = 10\,\mu$m, p $= 2\,\mu$m and $w = 0.2\,\mu$m, the capacitance is 1.5 fF for GaAs and InGaAs with $\epsilon_{sc} \approx 13$. Optimum values for various design frequencies can be found in Ref. 58. For $\nu_{RC} = \nu_{tr} = 1$ THz, values of $s = 1\,\mu$m, $w = 0.07\,\mu$m and $A = 73\,\mu$m^2 can be found for LT-GaAs with $R_A = 70\,\Omega$, for instance.

A good approximation for the capacitance of p-i-n diode–based mixers with $L_x, L_y \gg d_i$ is a good approximation for the capacitance of a plate capacitor

$$C_{\rm pin} = \epsilon_0\epsilon_{sc}A/d_i, \tag{41}$$

where $A = L_x L_y$ and d_i is the intrinsic layer length. For GaAs and InGaAs, an area of A $= 100\ \mu$m^2 and $d_i = 0.5\,\mu$m provides $C_{pm} = 23$ fF. The desired value of 2.3 fF can only be achieved for extremely small cross sections or very large values of d_i. The latter, however, would degrade the transit time performance.

Summarizing this general discussion on AE mixers we find for photoconducting AEs

$$P_{THz} = \frac{1}{2} R_A (I_0^{id})^2 \eta_{\text{ext}}^2 \eta_{t,pc}(\nu_{THz}) \eta_{RC}(\nu_{THz}) \tag{42}$$

$$P_{THz} = \frac{1}{2} R_A (I_0^{id})^2 \eta_{\text{ext}}^2 \left(\frac{\tau_{\text{rec}}}{\tau_{tr}}\right)^2 \frac{1}{1+(\nu_{THz}/\nu_{\text{rec}})^2} \times \frac{1}{1+(\nu_{THz}/\nu_{RC})^2}, \tag{43}$$

with $\eta_{\text{ext}}, \nu_{\text{rec}}, \nu_{RC}$ given in Eqs. (20), (29), and (37), respectively. For p-i-n–based AEs, we obtain a formally similar expression

$$P_{THz} = \frac{1}{2} R_A (I_0^{id})^2 \eta_{\text{ext}}^2 \eta_{t,\text{pin}}(\nu_{THz}) \eta_{RC}(\nu_{THz}) \tag{44}$$

$$P_{THz} = \frac{1}{2} R_A (I_0^{id})^2 \eta_{\text{ext}}^2 \frac{1}{1+(\nu_{THz}/\nu_{tr})^2} \cdot \frac{1}{1+(\nu_{THz}/\nu_{RC})^2}, \tag{45}$$

with $\eta_{t,\text{pin}}$ and ν_{tr} from Eqs. (34) and (35). They differ, however, in the photoconductive gain, which is much smaller for photoconductors, and in the transit time or lifetime of the carriers.

Secs. II C and II D deal with the realization of photoconductive and p-i-n–based AEs. We will find that it is difficult to achieve small enough capacitances in both photoconductors and p-i-n AEs if, at the same time, the transport-related reduction factors $\eta_{t,pc}(\nu_{THz})$ or $\eta_{t,\text{pin}}(\nu_{THz})$ should remain large. The desired large values of $\eta_{t,pc}(\nu_{THz})$ and $\eta_{t,\text{pin}}(\nu_{THz})$ favor small contact separation s or thin intrinsic layers d_i. A reduction of s or d_i, however, implies an increase of C_{pm}. The other option to achieve sufficiently small values for C_{pm} is a small device area A. Pursuing this option, on the other hand, is bound by the fact that dissipating the total laser power P_L within an extremely small area A may yield very high power densities. This may lead to thermal breakdown of the device at relatively low values of $P_{L,0}$ and, consequently, low photocurrents and THz power.

2. Antennas

A very crucial point regarding the performance of a photomixer is the antenna. Most conveniently, planar antennas are used that are directly deposited onto the contacts of the photomixer. Broadband logarithmic spirals as depicted in Fig. 3(a) are frequently used to take advantage of the large tuning range. In fact, the tuning range of the photomixer is mainly limited by the antenna design. The lower cutoff frequency is approximately where the overall arm length $L \approx (r_{2,\max} + r_{1,\max})/(2\cos\Psi)$ reaches one wavelength,[60,63] $\lambda_0/\sqrt{\epsilon_{\text{eff}}}$, with the radii as indicated in Fig. 3(a). The upper cutoff frequency strongly depends on the device geometry. In many cases, such antennas are designed to be self-complementary. According to Babinet's principle their radiation resistance is then

$$R_A = \sqrt{\mu_0/(4\epsilon_0\epsilon_{\text{eff}})} = \frac{Z_0}{\sqrt{4\epsilon_{\text{eff}}}} \approx 60\pi/\sqrt{\epsilon_{\text{eff}}} \approx 72\,\Omega \tag{46}$$

for the whole frequency range, where $\epsilon_{\text{eff}} = (1+\epsilon_{sc})/2$ for antennas on a semiconductor–air interface (with $\epsilon_{sc} = 13$).

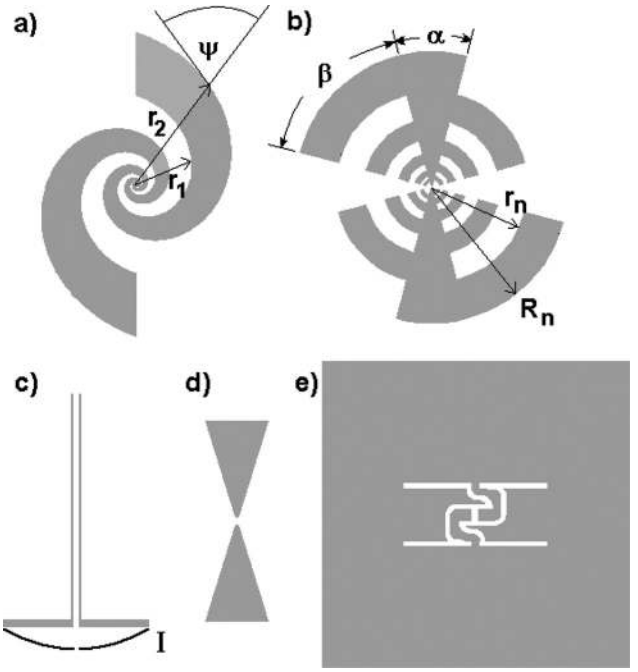

FIG. 3. (a) Logarithmic spiral antenna. (b) Logarithmic-periodic antenna. (c) Half-wavelength dipole antenna. The current distribution is indicated. (d) Bow-tie antenna. (e) Double slot antenna. Antennas are not to scale.

Logarithmic spirals provide circularly polarized radiation in the specified frequency range. At frequencies smaller than the lower cutoff frequency, the radiation becomes elliptically polarized.[63] Spirals are nonresonant antennas and provide a very smooth frequency characteristics. To enhance the output power, resonantly enhanced broadband antennas can be used such as the logarithmic-periodic antenna in Fig. 3(b). It consists of a bow-tie antenna with attached resonant arms. The arm is resonant at $\nu_n = (2c)/[\pi(R_n + r_n)\sqrt{\epsilon_{\text{eff}}}]$, enhancing the power output at this frequency.[64] The operation bandwidth is determined by the smallest and the largest arm. In practice, the smallest resonance is limited by the gap defined by the photomixer, typically limiting the maximum frequency to about 4–5 THz. There is no fundamental design limit for the low-frequency cutoff, however, the space requirement of the antenna on the chip increases proportional to the wavelength. Thus, the low-frequency cutoff is typically chosen not much less than 100 GHz for sub-mm sized antennas. The resonant enhancement is visible in the frequency characteristics, which is therefore not as smooth as that of the spiral antenna.

If maximum power output at a given frequency is required, resonant antennas would be the choice. The simplest resonant antenna is a half-wavelength dipole, with $l \approx \lambda/2$ [Fig. 3(c)]. The reactance of the antenna features a zero-crossing at the resonance frequency. Its radiation resistance is $R_A \approx 71\,\Omega/\sqrt{\epsilon_{\text{eff}}} \approx 27\,\Omega$. The actual resonance frequency and radiation resistance depend on the complete system including the photomixer as well as parasitics. Therefore, simulations are essential to achieve emission at the target frequency. Note that the radiation resistance of a dipole is typically much less than that of a broadband antenna. The RC roll-off will be less severe and appears at higher frequencies. Therefore, higher output power levels at 1 THz (and

above) as well as higher RC 3 dB frequencies are obtained with resonant antennas. For further improvement of the impedance matching, double dipoles or their inverted structure, the double slot antenna [Fig. 3(d)], can be used. These structures require careful simulations. The electric path length of each antenna arm has to be matched for broadside emission. Emission at the target frequency and the desired radiation resistance not only depend on the dipole length but also on the distance of the two dipoles. Well-designed resonant structures typically offer more output power at their respective design frequency. Furthermore, they may be designed to have a much smaller radiation resistance than broadband antennas, shifting the RC 3 dB frequency to higher values. This leads to higher output levels for dipole resonances above the RC 3 dB frequency of the same photomixer equipped with a broadband antenna.

In contrast to photoconductive switches, the p-i-n diode and n-i-pn-i-p photomixer devices are not planar. They also contain (nonmetallic) conducting layers such as the top and bottom contact semiconductor layer. Both the device geometry and the reduced conductance of these layers reduce the performance and cause parasitics. Therefore, p-i-n–based AE devices are more difficult to design and to process than their photoconductive counterparts. These deviations need to be accounted for in the simulations. The geometrical effects on the antenna performance, for example, may be reduced by depositing a flattening insulation layer below the antenna, matching the height of the mesa.

C. Photoconductive mixers with antennas

1. Thermal and electrical optimization

To work out the details of the performance of photoconductive mixers, the thermal load of the device, space charge screening, and electrical breakdown have to be considered as well. We have seen in Sec. II B 1, Eqs. (29) and (43) that a short carrier lifetime, τ_{rec} is required to shift the 3 dB frequency of the lifetime roll-off, $\nu_{\mathrm{rec}} = (2\pi\tau_{\mathrm{rec}})^{-1}$, to higher frequencies. However, Eq. (43) shows that a short lifetime reduces the THz power output at low frequencies, as $P_{THz} \propto g^2 \propto \tau_{\mathrm{rec}}^2$ for $\nu_{THz} < \nu_{\mathrm{rec}}$ and does not seem to be of any use at high frequencies, at first glance. This picture changes if we also take thermal failure and electrical breakdown into account. The total energy dissipated in the AE is the sum of electrical and absorbed optical power. For very small gain and nonradiative decay of electron-hole pairs, basically the whole absorbed optical power, $\eta_{\mathrm{ext}} P_{L,0}$ is transformed into heat. The dissipated electrical power in the photoconductor is given by the product of the (dc) photocurrent, $I_{DC} = I_0 \tau_{\mathrm{rec}}/\tau_{tr} = g I_0$ with $I_0 = \eta_{\mathrm{ext}} e P_{L,0}/(h\nu_0)$, and the applied voltage, U_{ext}. This yields for the dissipated power

$$P_{\mathrm{dis}} = I_{DC} U_{\mathrm{ext}} + \eta_{\mathrm{ext}} P_{L,0} = \left(g \frac{e U_{\mathrm{ext}}}{h\nu_0} + 1 \right) \eta_{\mathrm{ext}} P_{L,0}. \quad (47)$$

As eU_{ext} is typically much larger than $h\nu_0$ (for operation at 800 nm, $eU_{\mathrm{ext}} \approx 30\, h\nu_0$ at a typical bias of 40 V, for example) the electric contribution dominates, unless the photoconductive gain is small enough ($<1/30$, for example). For a contact separation of 2 μm this condition is fulfilled for $\tau_{\mathrm{rec}} > 0.7$ ps. A short recombination time reduces the dissipated power. This allows for higher laser power, $P_{L,0}$.

We have seen in the discussion of Eq. (43), that the emitted THz power scales with τ_{rec}^2 for $\nu_{THz} < \nu_{\mathrm{rec}} = (2\pi\tau_{\mathrm{rec}})^{-1}$ but for $\nu_{THz} > \nu_{\mathrm{rec}}$, the lifetime-dependence vanishes. In this high-frequency limit, the THz power exhibits a roll-off of $P_{THz} \sim (\nu_{THz}\tau_{tr})^{-2}$. For a given design THz frequency ν_{THz}^{opt}, a recombination lifetime which provides $\nu_{\mathrm{rec}} \approx \nu_{THz}^{\mathrm{opt}}$ represents a good compromise. This value allows for obtaining 1/2 of the maximum power (ν_{rec} is the 3 dB frequency of the lifetime roll-off) and also allows for high laser power at the same time according to Eq. (47), when the device is operated at its maximum thermal load. Verghese *et al.*[65] determined the maximum temperature rise for low temperature grown (LT) GaAs against its thermal bath to be about 120 K (measured at 77 K and 290 K bath temperature for $\tau_{\mathrm{rec}} \approx 0.2 - 0.3$ ps.) before thermal breakdown occurs. This corresponded to a maximum optical power in the range of 100 mW for LT-GaAs on GaAs.

Another aspect favoring short recombination times is related to the electrical breakdown. When electrons and holes are optically generated between the metal electrodes, they will drift toward the respective electrodes in the electric field induced by the external bias. The separation of electrons from holes causes field enhancement in the contact regions due to the accumulation of space charges and causes field screening in between the contacts. The space charge close to the contacts originates from trapped carriers that do not find a recombination partner of opposite sign due to the carrier separation.[66] The larger the recombination time, the further the center of mass of electrons will move apart from the center of mass of holes. This effect is well known for standard GaAs photomixers,[67] where carrier lifetimes are larger than the transit times through the gap. As a consequence, the material charges up and the external bias will be severely screened. Most of the external bias drops within a very short distance, d_{scr}, close to the electrode, resulting in locally very high field strengths of $E_{\mathrm{loc}} = U_{\mathrm{ext}}/d_{\mathrm{scr}}$ but a weak field in the active structure. To restore the latter, more and more bias will have to be applied at high optical power levels until E_{loc} reaches the breakdown field of the material, causing electrical failure. The breakdown fields of the most prominent photoconductive material of LT-GaAs is typically in the range of 500 kV/cm,[51] but may extend up to 1000 kV/cm,[57] which exceeds that of semi-insulating GaAs by a factor of ≈3. Optimum values for the lifetime versus design frequency are presented by Brown.[57]

For a more detailed treatment of this problem, however, we would also have to distinguish between trapping and recombination. Trapped charge carriers are responsible for space charge screening but do not contribute to the THz current. There is evidence that the recombination takes place on a much longer time scale (i.e., 10 ps to several ns[66,68]) than the trapping time, which is shorter than 1 ps for high-quality material. Within the fs and THz community, however, the trapping time is referred to as τ_{rec} as it is responsible for reducing carrier contributions to the current. We also refer to τ_{rec} within this paper.

Finally, it should be noted that feedback of the emitted THz field on carriers in the photoconductive material causes an effective degradation of the THz signal.[69] Such effects, however, appear only at high-THz field strength under pulsed operation and should be negligible for continuous-wave operation.

2. Low-temperature grown GaAs photoconductors

By growing GaAs at low temperatures (LT-GaAs), short recombination lifetimes in the range of $\tau_{rec} \sim 150$ fs to a few ps are obtained. The low temperature ($\sim$200 °C) is responsible for nonstoichiometric growth including up to 1.5% excess arsenic. *In situ* annealing at 500–600 °C is necessary to initiate the high resistivity of the material by forming antisite defects As_{Ga} acting as deep double donors, and also quasimetallic arsenic clusters. The room temperature bandgap of GaAs is at 870 nm (1.42 eV). LT-GaAs photomixers can thus be optically driven with Ti:sapphire laser systems and (Al)GaAs-based diode lasers.

Photoconductors are not very difficult to process. Metal electrodes are directly deposited on the LT-GaAs material without any further annealing. A thin layer of optically transparent dielectric may additionally be deposited on the structure for passivation and antireflection coating. To prevent electric field peaks originating from rough electrode edges, the metal contacts are usually defined by electron beam lithography. For CW operation, the electrodes are usually designed as finger structures [Fig. 4(a)] with a gap in the range of 1–2 μm. The electrodes are typically biased with less than 60 V. The narrow gaps are required to achieve a short transit time for increasing the photoconductive gain g [Eq. (30)] at a fixed photocarrier lifetime τ_{rec}. Narrow gaps, however, increase the device capacitance according to Eq. (38). The optimum finger distance is a compromise between transit time/lifetime, RC optimization, and heat dissipation. Optimum values depend on the THz frequency and were calculated for resonant and broadband antennas in the review by Brown.[57] For 1 THz, the optimum finger distance turned out to be 1μm, providing a capacitance of 2.2 fF for a 9 μm $\times$ 9 μm active area, and hence, an RC 3 dB frequency of about 1 THz with a broadband 70 Ω antenna. The ideal recombination time is about 0.3 ps. Record values of 2 μW (1 μW) at 1 THz have been achieved with LT-GaAs continuous wave photomixers with a resonant (broadband) antenna.[57] LT-GaAs photoconductors are the most frequently used type of photomixer. In particular, pulsed THz time-domain systems became an excellent tool for spectroscopic applications.

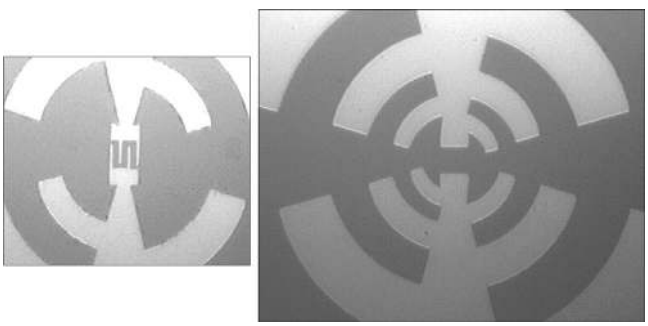

FIG. 4. (Left) Finger contacts on LT-GaAs in a logarithmic-periodic broadband antenna. The area is 10 μm $\times$ 10 μm. (Right) Same antenna with fingerless gap for pulsed operation.

3. Novel materials for photoconductors

An alternative method to implement short carrier lifetimes has been developed with the growth of ErAs layers embedded in GaAs. ErAs has a rock salt lattice but nearly the same lattice constant as GaAs. Constraining to a thickness of less than 1.8 monolayers of ErAs allows for high quality material growth.[70] The ErAs layer forms elongated islands and provides a quasimetallic behavior leading to excellent recombination performance. Photogenerated carriers can be efficiently captured in adjacent ErAs layers. Recombination times between 120 and 190 fs have been reported for 60 periods of 1.2 monolayers of ErAs and 20 nm of GaAs.[71,72] The resistivity of ErAs:GaAs depends strongly on the ErAs deposition amount and on the epitaxial growth temperature.[74] It typically does not reach as high values as LT-GaAs but is sufficient to provide high quality photoconductors with several MΩ resistance for typical finger structures.[57,71,73] For CW operation, THz power levels of 0.5–2 μW at 1 THz were achieved,[74] depending on the operation mode, which is comparable to LT-GaAs photomixers.

In recent years, several groups have also focused on 1550 nm-based photomixers to take advantage of the fast development of the telecom sector. Reduced costs for optical elements and lasers allow for cheaper THz systems. Furthermore, the photon energy at 1550 nm is almost half of that at 800 nm (LT-GaAs). The responsivity of the devices, e/hv, increases by almost a factor of two and, consequently, the optical to THz conversion efficiency by a factor of four. The standard material for telecom frequency operating lasers is $In_{0.53}Ga_{0.47}As$ grown lattice matched on InP substrates. Unfortunately, growing InGaAs at low temperatures does not provide deep trap levels or short recombination times, but leaves n-background doping[75] with the Fermi level close to the conduction band edge.

As InAlAs layers (with a similar bandgap as GaAs) grown at low temperatures provide deep recombination centers similar to LT-GaAs, an alternative method implements a superlattice of InGaAs well layers and InAlAs barrier layers, both grown at low temperatures.[76] To compensate for n-conductivity in the InGaAs layer, an appropriate p-doping density is chosen. Absorption takes place in the LT-InGaAs layers. The layer thickness is chosen to be comparable to the exciton radius, allowing for tunneling of the carriers into the InAlAs layers with recombination centers. The reported design consisted of 8 nm wide InAlAs barriers and 12 nm wide InGaAs well layers. The resulting effective bandgap energy of the superlattice is only slightly higher (at shorter wavelengths). Recombination times of 750 fs have been achieved and first THz experiments were carried out with a completely fiber-based system under pulsed operation.[76] A packaged example of such a device is shown in Fig. 19.

Another very successful approach uses standard InGaAs material with little background conductivity and long

recombination times. Deep centers are created by heavy ion bombardment. One method is implantation of iron in the InGaAs material, which causes deep traps. Irradiation with 2 MeV Fe^+ ions resulted in resistivities in the range of a few 100 Ωcm and carrier lifetimes of 0.3 ps.[77] Instead of implanting ions, irradiation of Br^+ ions with a higher kinetic energy of 11 MeV causes the ions to penetrate through the active layer and damage the lattice, providing deep trap states. Only very few ions stay in the active layer of the device for the ion energies used.[78,79] This way, recombination times of 0.2–0.3 ps have been achieved. Under pulsed operation, 0.8 μW of total THz power could be extracted. Continuous-wave operation reached 10 nW at 1 THz.[80] A resistivity of 5 Ωcm[81] and a carrier mobility of 490 $cm^2/(Vs)$ were reported.[78]

As a promising third method, embedded ErAs nanoparticles in standard InGaAs material can be used, in a similar manner as that described for GaAs. The difference in the lattice constant is now larger, as it was for the growth on GaAs. However, deposition of 1–2 ErAs monolayers[82] allows for ErAs island formation with quasimetallic properties and epitaxial overgrowth of the islands by high quality InGaAs material.[70] To allow for an efficient capture process of photogenerated carriers, an ErAs:InGaAs superlattice as in the ErAs:GaAs system is used. Short periods allow for short recombination times in the range of 300 fs as reported for a period of 5 nm.[82] For ErAs layers in GaAs, it was observed that the semimetallic ErAs inclusions act as trapping sites with an intrinsic capture time well below 190 fs.[72] In the InGaAs material, however, the Fermi energy of the ErAs layers is close to the conduction band, effectively providing n-doping.[82] Therefore p-doping is used for compensation to achieve a high dark resistance.[82] as shown in Fig. 5. The best values so far have been achieved with delta doping as high as 5×10^{13} cm^{-2} where a resistivity of 343 Ωcm was reported.[83]

For further reading, a seminal review on photoconducting mixers is given by Brown.[57] For additional information on InGaAs photoconductors we refer to Brown *et al.*[84]

4. THz detection using photoconductors

An important advantage of photoconductors is that they can also be used as THz detectors. They operate in the current mode without external bias for a THz signal originating from another photomixer. The detector antenna receives the THz field which biases the MSM junction. The same optical signal that was previously used to generate the THz wave is used to create free carriers that are separated by the THz bias. In pulsed systems, the THz wave is temporally much broader than the optical pulse due to the finite lifetime and RC time constant of the sender. The THz field strength can thus be scanned with an optical pulse by introducing a small delay between the THz and the optical wave in the range of the pulse duration. Such systems are termed THz time-domain (TDS) systems. They are the workhorses in many spectroscopic applications.[9,85]

For CW detection, the heterodyned laser signal and, consequently, carrier generation in the detector is modulated with the THz frequency. The photocurrent is proportional to the product of the optical envelope and THz field. The junction rectifies the signal, given that both signals are in phase. This phase may again be chosen by a delay stage. For frequency-independent operation, the detector and sender path length have to be matched to achieve zero delay and zero phase difference at any frequency.

High resistivity of the material is particularly important for detection. Due to the zero bias operation, small stray fields or static charging may introduce a parasitic (dark) current and excess noise. For low-resistivity junctions, this may mask the actual photocurrent. LT-GaAs exhibits very high resistivities of the order of 10^7 Ωcm[86] providing an excellent detector, even for very small THz signals.

D. p-i-n Diode-based AEs

1. Optimization of device parameters

In the previous section we have seen that photoconducting AEs are quite easy to fabricate, but they suffer from a number of deficiencies when compared with p-i-n–based AEs.

- Regarding the optical-to-THz conversion efficiency, photoconductive AEs are limited by a low photoconductive gain, $g \ll 1$, whereas p-i-n–based AEs exhibit unity gain, as each photogenerated carrier reaches the contact.
- The high external voltage (typically about 30 V) required in photoconducting AEs for optimum performance implies a significant electrical thermal load. This limits the maximum tolerable power. In p-i-n–based AEs, the electric field originating from the built-in voltage U_{bi} or a small reverse bias $|U_{\mathrm{ext}}| < 3\mathrm{V}$ is sufficient to reach the optimum carrier velocities. The electrical thermal load $e(U_{bi} + U_{\mathrm{ext}})$ is much smaller.
- As a result of the high electric fields and current density near the edges of the contacts in photoconducting AEs, maximum power dissipation takes place at these edges and tends to cause fatal device failure due to electro-migration of the contact metal, for example. In p-i-n–based AEs, in contrast, this problem does not exist, as the voltage drop and, hence, the energy dissipation at the (ohmic) contacts to the highly doped p- and n-layers is negligible.

In contrast to their photoconductive counterparts, p-i-n AEs can exhibit ideal performance at sufficiently low frequencies. At higher frequencies, however, they suffer from both transit time and RC roll-off. Therefore, we will first discuss how far the influence of these power roll-offs can be overcome, or, at least, minimized. Experimental realizations of p-i-n diode–based AEs will be presented in Secs. II D 5 (UTC diodes) and II D 6 (n-i-pn-i-p THz emitters).

a. Trade-off between transit time and RC roll-off. In Sec. II B 1 we had found the expression Eq. (45) for the THz power of a p-i-n–based AE

$$P_{THz} = \frac{1}{2} R_A (I_0^{id})^2 \eta_{\mathrm{ext}}^2 \frac{1}{1 + (\nu_{THz}/\nu_{tr})^2} \cdot \frac{1}{1 + (\nu_{THz}/\nu_{RC})^2}. \tag{48}$$

Inserting the transit time for electrons propagating with an average velocity $\bar{v}$ through the i-layer of thickness d_i into the

expression for the transit time roll-off frequency, Eq. (35), yields

$$v_{tr,\mathrm{pin}} = \frac{\bar{v}}{2d_i} \propto d_i^{-1}. \tag{49}$$

With Eq. (41) for the capacitance of a p-i-n–based photomixer, we get the RC 3 dB frequency of

$$v_{RC} = \frac{d_i}{2\pi\epsilon_0\epsilon_r AR_A} \propto d_i. \tag{50}$$

A comparison of Eqs. (49) and (50) clearly exhibits the trade-off between optimizing either the transit time or the RC roll-off when choosing a suitable value for d_i. The best choice is given when the two roll-off 3 dB frequencies become the same, i. e.,

$$d_i^{(\mathrm{opt})} = \sqrt{\pi\epsilon_0\epsilon_{sc}AR_A\bar{v}}, \tag{51}$$

providing a common 6 dB frequency of

$$v_{6dB}^{(\mathrm{opt})} = \sqrt{\frac{\bar{v}}{4\pi\epsilon_0\epsilon_{sc}AR_A}}. \tag{52}$$

Equation (48) can then be replaced by

$$P_{THz} = \frac{1}{2}R_A I_{ph}^2 \left(\frac{1}{1+(v_{THz}/v_{\mathrm{opt}}^{6dB})^2}\right)^2, \tag{53}$$

where we also substituted the photocurrent, $I_{ph} = I_0^{id}\eta_{\mathrm{ext}}$.

As an example, we choose $R_A = 70\ \Omega$, a reasonable cross section of $A = 35\ \mu\mathrm{m}^2$, $\epsilon_{sc} = 13$, and for $\bar{v}$ a typical value for the electron high-field saturation velocity $v_{\mathrm{sat}} = 10^7$ cm/s. This yields

$$d_i^{(\mathrm{opt})} = 300\,\mathrm{nm}, \quad \text{and} \tag{54}$$

$$v_{6dB}^{(\mathrm{opt})} = 0.166\ \mathrm{THz}. \tag{55}$$

From Eq. (53) and the example just presented we learn that there is not much room left for improvement of $v_{6dB}^{(opt)}$ by a better geometrical layout of the p-i-n diode. Even a reduction of the cross section area by a factor of 10 (which becomes challenging in terms of processing and optical coupling to the structure) would only result in $v_{6dB}^{(opt)} \approx 0.52$ THz.

From Eqs. (51) and (52) it is obvious that a higher carrier velocity $\bar{v}$ could improve the performance by shifting the 6 dB frequency to higher values. So far we have assumed carrier transport with the saturation velocity. If the influence of scattering on transport can be minimized, transport may become ballistic, i.e. $v = at$, with an acceleration by the electric field of

$$a = \frac{e|\vec{E}|}{m^*}. \tag{56}$$

At high fields, two main scattering mechanisms are relevant. First is the (longitudinal optical) phonon scattering: This reduces the absolute value of electron acceleration but leaves the direction of transport nearly unchanged.[87,88] The typical

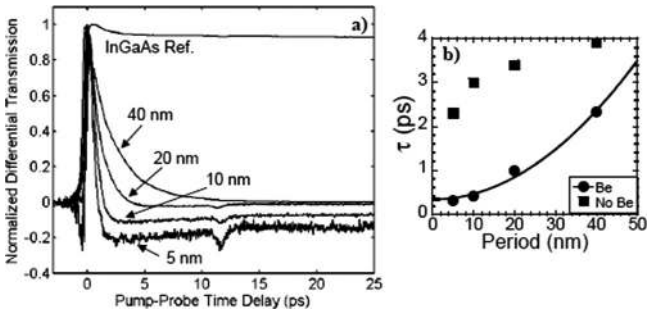

FIG. 5. Left: Normalized differential optical transmission versus pump-probe time delay for Be-doped InGaAs samples with superlattices of 0.8 monolayers ErAs deposition per period and superlattice periods from 5 nm to 40 nm. The photocarrier lifetime decreases significantly with decreasing ErAs layer spacing. Right: Measured photocarrier lifetimes versus period for structures with and without Be doping. Reprinted with permission from D. C. Driscoll, M. P. Hanson, A. C. Gossard, and E. R. Brown, Appl. Phys. Lett. **86**, 051908 (2005). © 2005 American Institute of Physics.

scattering time is $\tau_{LO}^{sc} \approx 100$ fs. Second, the inter-valley scattering: As illustrated in Fig. 6, electrons in the Γ valley can be scattered into side valleys once they have reached the energy of the inter-valley gap, $\Delta_{\Gamma L}$. Phonon scattering into the L side valleys is very efficient because there are 8 of them with a much higher density of states as in the Γ valley. This scattering mechanism with scattering times in the range of ≈ 50 fs strongly randomizes the direction of motion. The electron velocity finally reaches the saturation value. Electrons with energies below $\Delta_{\Gamma L}$, however, experience continual acceleration. This is commonly denoted as quasiballistic transport.[89] The transport in $Al_xGa_{1-x}As$ and $In_{0.53}Ga_{0.47-x}Al_xAs$ p-i-n diodes has been described by realistic Monte Carlo simulations.[87] Fig. 7 shows the simulated average speed and the covered distance as a function of time. These transport regimes have been proven experimentally in specially designed GaAs p-i-n structures.[45]

The first kink in the velocity graphs (only visible for fields lower than 20 kV/cm) is attributed to the onset of LO-phonon scattering. The electron velocity continues to increase linearly, however, with a reduced acceleration. The onset of inter-valley scattering appears at the peak of the velocity and strongly decelerates the electrons which finally reach saturation velocity. This phenomenon is well known as

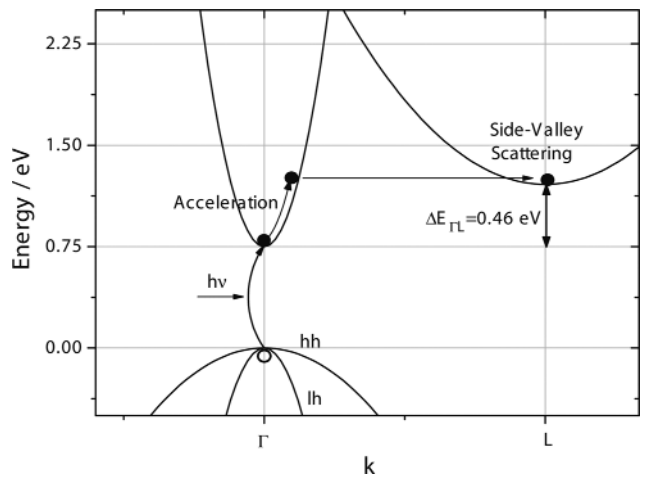

FIG. 6. Schematic four-valley approximation of InGaAs.

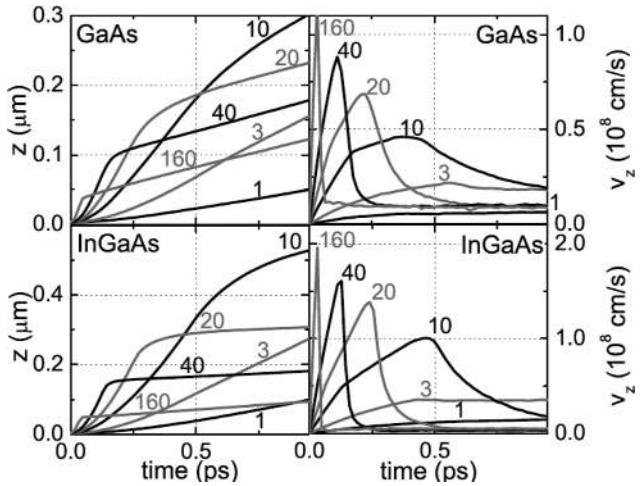

FIG. 7. Average speed and distance of an electron ensemble accelerated by a constant electric field in GaAs and InGaAs.[87] The fields are in units kV/cm. 1 THz corresponds to a transit time of 0.5 ps. Please note the different velocity scales for GaAs and InGaAs. Electrons in InGaAs are accelerated more easily due to their smaller effective mass.

velocity overshoot in direct bandgap semiconductors. Quasiballistic transport with velocities much larger than v_{sat} can be realized as long as the electron energy is (well) below the threshold energy for inter-valley scattering. Accordingly, the distance traveled by the electrons can reach a few hundreds of nm if the electric field is chosen properly. In a p-i-n diode, electrons can travel ballistically across the intrinsic layer if the potential drop, $e|\vec{E}|d_i$, is (approximately) equal to the threshold energy $\Delta_{\Gamma L}$ for inter-valley scattering (Fig. 6). From Fig. 7, optimum transport fields of 10–20 kV/cm and a transport length 180 nm for GaAs and 300 nm for InGaAs are found to provide a transit time 3 dB frequency of $1/(2\tau_{tr}) = 1$ THz. For holes with a much higher effective mass, the acceleration will be accordingly lower and no noteworthy velocity overshoot is observed as no side valleys are available for holes. As we will see later, basically all high speed p-i-n diode–based concepts are therefore designed to allow for electron transport only.

If the high-field transport with saturation velocity, $\bar{v}_z = v_{sat} = 10^7$ cm/s, is replaced by ballistic transport, the average velocity $\bar{v}$ can become 1/2 of the maximum "overshoot velocity", v_{bal}^{max}. With an intrinsic layer length of 300 nm, an InGaAs-based device can even reach a transit time 3 dB frequency of 1 THz at sufficiently low transport fields around 20 kV/cm. This allows for some flexibility in the device design, as longer intrinsic layers can be used to match transit- and RC 3 dB frequencies. According to Eqs. (51) and (52), a higher mean velocity allows for a considerably higher 6 dB frequency compared to the calculated 0.166 THz for high-field transport with the saturation velocity in a 300 nm intrinsic layer.

2. Realistic transit time roll-off of p-i-n diodes

We will show in this section that the transit time roll-off for p-i-n diodes in Eqs. (34) and (35) is a good approximation only below the respective 3 dB frequency. Major deviations will appear above this frequency, depending on the layout of the absorbing regions and the nature of the transport. In contrast, the expression for photoconductors in Eq. (29) is exact.

To replace the simple estimate by a rigorous calculation we take into account that the current in the contact layers is actually the displacement current originating from all the electron-hole pairs generated within the i-layer. Each photogenerated carrier contributes an elementary current $ev(t-t')/d_i$ during its whole transit time through the intrinsic layer. Here, $v(t-t')$ is the velocity of a carrier at time t, but generated at time t'. The expressions for the resulting currents and resulting roll-off behavior are derived for different scenarios in Appendix A, regarding the transport regime (drift current with constant drift velocity or ballistic transport) and the spatial distribution of the absorption within the intrinsic layer (uniform or nonuniform absorption, i.e., spatially constricted absorption).

In the following, we provide a discussion of the transport-related roll-off term of the THz power resulting from the expressions derived in Appendix A. In all cases, a fully modulated laser power according to Eq. (7) has been assumed. In all scenarios, the transit time roll-off factor is unity at sufficiently low frequencies. We will use the same sample geometry ($A = 35\ \mu m^2$, $d_i = 300$ nm) throughout this section in order to represent the differences in performance associated with the different transport scenarios. We will neglect the RC roll-off, which is considered to be the same for all the scenarios.

a. Standard p-i-n diode. For the case of a standard p-i-n diode with uniform absorption in the intrinsic layer, the THz power is due to equal contributions of the electrons and holes to the total current at frequencies much lower than 1/2 of the inverse transit times $\tau_{tr,e} = d_i/v_e$ and $\tau_{tr,h} = d_i/v_h$. In Appendix A it is shown that the roll-off behavior of the electron and hole current is formally the same, but the 3 dB roll-off frequency scales with the inverse of the respective transit times. For our example we have assumed that electrons are traveling at their high-field saturation velocity, i.e. $v_e \sim v_{sat} = 10^7$cm/s, and that the hole velocity is proportional to the electric field, $|\vec{E}|$, according to $v_h = \mu_h|\vec{E}|$. The roll-off of the hole contribution is shifted by a factor $\tau_{tr,e}/\tau_{tr,h}$ to lower frequencies mainly because of the lower hole velocity due to larger effective hole mass. This implies that the hole contribution to the AC current is small in the THz frequency range. Consequently, the THz power is solely determined by the electron current amplitude and its roll-off at the frequencies of interest. Compared to its ideal value, it is shifted to lower power values by a factor of 4 as only the electron part (i.e. 1/2 of the generated current) contributes. Fig. 8 depicts the THz power versus THz frequency in a double logarithmic plot for the case $v_h = \beta v_{sat}$ with $\beta = 0.1$ and 0.3 as full lines. The THz power rolls off according to

$$P_{THz}(\nu) = \frac{1}{2}R_A|I_e^{AC}(\nu) + I_h^{AC}(\nu)|^2 \text{with} \tag{57}$$

$$I_{e,h}^{AC}(x_{e,h}) = I_0\frac{1}{x_{e,h}^2}\sqrt{(\sin x_{e,h} - x_{e,h})^2 + (\cos x_{e,h} - 1)^2} \cdot \sin(\omega_{THz}t + \varphi_{e,h}) \quad \text{and} \tag{58}$$

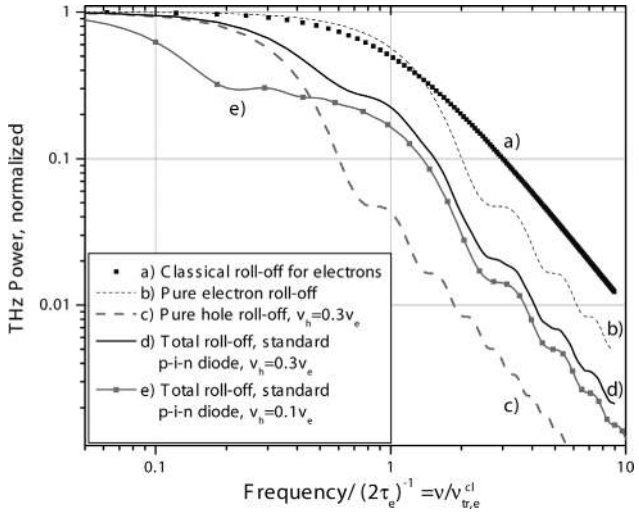

FIG. 8. Transit time roll-offs for (a) electrons according to Eq. (34) with a 3 dB frequency of $v_{tr} = v_{tr,e}^{cl} = 0.5 \cdot (\tau_{tr,e})^{-1}$. (b) Normalized pure electron performance of a standard p-i-n diode according to Eq. (58) exhibiting a 3 dB frequency of $v_{tr} = 0.55(\tau_{tr,e})^{-1}$. (c) Normalized pure hole performance exhibiting $v_{tr} = 0.55 \cdot (\tau_{tr,h})^{-1}$ and $v_h = 0.3v_e$. (d) Combined transit time roll-off of electrons and holes according to Eq. (57) with $v_h = 0.3v_e$. (e) Same as (d) but for slower holes with $v_h = 0.1v_e$.

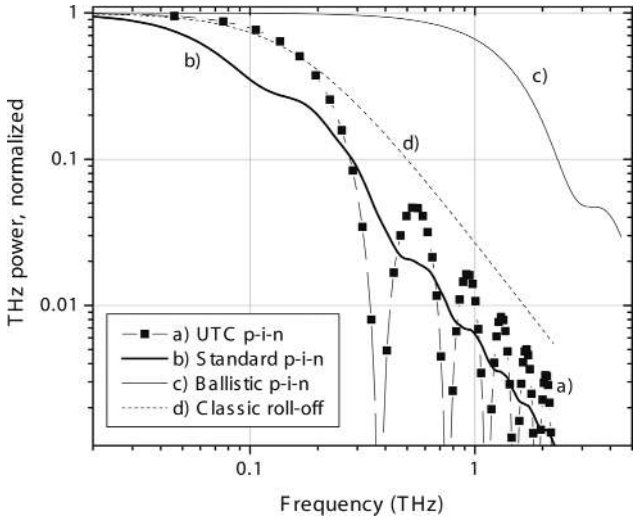

FIG. 9. Transit time performance of (a) an InGaAs UTC diode as described in the text with $d_i = 300$ nm intrinsic layer length. Transport at the saturation velocity was assumed with a 3 dB frequency of 166 GHz. For comparison, the classical expression with a transit time roll-off of $\eta_t = [1 + (2\tau_{tr}v_{THz})^2]^{-1}$ is also shown (d). (b) Standard p-i-n diode with same dimensions. The hole velocity is assumed to be $0.3v_e$. (c) Ballistic p-i-n diode ($d_i = 300$ nm) as described in the text. A ballistic 3 dB frequency of 1.28 THz can be achieved with the same device dimensions.

$$\varphi_{e,h} = \arctan\left(\frac{\cos x_{e,h} - 1}{\sin x_{e,h} - x_{e,h}}\right), \tag{59}$$

with $I_0 = \eta_{\text{ext}} e P_{L,0}/(h\nu_0) = I_e^{DC} + I_h^{DC}$ and $x_{e,h} = x_{e,h}(\nu_{\text{THz}}) = \omega_{\text{THz}}\,\tau_{e,h} = 2\pi\nu_{\text{THz}}\tau_{e,h}$.

In order to visualize the individual contributions due the electrons and holes alone, we have also included the corresponding graphs of $P_{e,THz}(\nu_{\text{THz}}) = \frac{1}{2}R_A|I_e(\nu_{\text{THz}})|^2$ and $P_{h,THz}(\nu_{\text{THz}}) = \frac{1}{2}R_A|I_h(\nu_{\text{THz}})|^2$ as dashed lines. The 3 dB frequency for these individual contributions corresponds to

$$\nu_{tr,(e,h)}^{\text{pin}} = 0.55\tau_{tr,(e,h)}^{-1}. \tag{60}$$

For comparison, the roll-off expression from Eq. (34) with the 3 dB frequency, $\nu_{tr} = 1/2\tau_{tr}$[Eq. (35)] is also shown.

It should be noted that v_h may approach v_{sat} at fields on the order of 100 kV/cm (corresponding to a reasonable voltage of $U = 3V - (E_G/e)$ applied to a p-i-n diode with $d_i = 300\,\text{nm}$). In this case, the transit time performance of holes approaches that of electrons. As a consequence, the roll-off of the total THz power at intermediate frequencies also becomes much less pronounced. However, such high biases have a strong negative impact on the lifetime of the device and also cause excessive heating.

b. Diodes with electron transport only. The situation at intermediate frequencies becomes more favorable if the photocurrent generation is restricted to a narrow region Δz close to the p-contact. This concept is used in the two approaches discussed in Secs. II D 5 and II D 6, uni-traveling-carrier (UTC) photodiodes[90] and n-i-pn-i-p superlattice photomixers with ballistic electron transport.[91] In both cases only electrons contribute to the current [strictly speaking, the fraction $(1 - \Delta z/2d_i)$], and the hole contribution (strictly speaking, the fraction $\Delta z/2d_i$) becomes negligible. For this reason, this design is expected to provide higher THz power at intermediate frequencies for the case $\bar{v}_h < \bar{v}_e$. Again, we assume that the electrons are traveling with a constant velocity of $\bar{v} = v_{\text{sat}}$. In this case, the AC amplitude of the photocurrent depends on the frequency as

$$I^{AC}(x) = I_0\,\text{sinc}(x/2), \tag{61}$$

with $x = 2\pi v_{THz}\tau_{tr}$. The results following from Eq. (61) are depicted in Fig. 9. Obviously, the THz power exceeds that of the standard p-i-n photomixer for $v_h = 0.3v_{\text{sat}}$ at intermediate frequencies [see curves (a) and (b) in Fig. 9]. Comparing these results with the carrier transit time of a standard p-i-n diode, we notice that the 3 dB roll-off frequency is found to be significantly lower, i.e.,

$$v_{tr} = 0.44\tau_{tr}^{-1}. \tag{62}$$

However, the transit time of electrons is much shorter (except at very high electric fields) than that of holes, providing higher THz output at high frequencies. The response goes to zero at $v_{THz} = \tau_{tr,e}^{-1}$ as a result of the $\text{sinc}^2(\pi v_{THz}\tau_{tr,e})$ frequency dependence of the transit time roll-off. This, however, is an artifact from neglecting the dispersion of the transit times and the assumed delta-shaped absorption region. A pronounced minimum at this frequency is, nevertheless, expected. A major advantage of the UTC concept will become clear later on in our discussion of the saturation and quasiballistic effects in Sec. II D.

c. Ballistic p-i-n diode. The transit time performance of p-i-n diode photomixers improves drastically if the electrons are not only generated within a narrow region of width Δz close to the p-contact layer, but if, in addition, the transport becomes ballistic. In this case, electrons are constantly

accelerated during the ballistic transit time, τ_{bal}. This scenario is realized in the n-i-pn-i-p-AEs (Sec. II D 6). The roll-off behavior of the AC current is derived in Appendix A, yielding

$$I_{AC}^{\mathrm{bal}} = I_0 \frac{2\sqrt{(\sin x - x\cos x)^2 + (x\sin x + \cos x - 1)^2}}{x^2}, \quad (63)$$

with $x = 2\pi v_{THz}\tau_{\mathrm{bal}}$. Fig. 9 also depicts the calculated roll-off of the THz power under optimized ballistic transport conditions ($e|\vec{E}|d_i = \Delta_{\Gamma L}$) in InGaAs for the same intrinsic layer length $d_i = 300$ nm as before. As expected, it is shifted to significantly higher frequencies, approximately by the factor $\bar{v}_{\mathrm{bal}}/v_{\mathrm{sat}} = 6.1$, 8.0, or 10 for GaAs, InP, and InGaAs, respectively, due to the shorter transit times. More realistically, the reduced acceleration due to LO phonon scattering results in about 35% smaller values. The linear increase of the velocity with time of flight further results in changes of the shape of the frequency dependence. It implies also a further increase of the 3 dB frequency to

$$v_{tr}^{\mathrm{bal}} = 0.55(\tau_{tr}^{\mathrm{bal}})^{-1}. \quad (64)$$

In summary, the detailed considerations on the transport in p-i-n diodes yield 3 dB frequencies close to $v_{tr} = (2\tau_{tr})^{-1}$, thus justifying using this simpler expression, provided that the appropriate transit times are used ($\tau_{tr,e}, \tau_{tr,h}, \tau_{tr}^{\mathrm{bal}}$, respectively). Interestingly, the transit time 3 dB frequencies of p-i-n diodes are about a factor of π larger than the RC 3 dB frequency, $v_{RC} = (2\pi\tau_{RC})^{-1}$ and the lifetime 3 dB frequency of photoconductors, $v_{\mathrm{rec}} = (2\pi\tau_{\mathrm{rec}})^{-1}$ as a result of the missing factor π.

3. Influence of screening at high current densities

Next, we discuss the influence of space charge accumulation in p-i-n-diodes. Qualitatively, it is clear that the current resulting from electron-hole generation within the absorption region changes gradually from pure hole current $I_h(z)$ on the p-doped (left) side to pure electron current $I_e(z)$ on the n-doped (right) side with $I_h(z) + I_e(z) = I = \mathrm{const}$. Assuming a uniform field, the carrier velocities v_e and v_h of the electrons and holes are constant but the hole charge density $e \cdot p(z)$ decreases from $|\bar{j}/v_h|$ at the left to $p = 0$ at the right hand side of the absorption region, while the electron charge density, $-e \cdot n(z)$, increases from $n = 0$ to $-|\bar{j}/v_e|$. As the space charge density increases with the current density, its influence is negligible at low photocurrents. It may, however, drastically deteriorate the performance at large current densities, i.e., at high laser power and small device cross section, A.

The effect of high space charge densities due to screening of the original field is schematically depicted in Fig. 10 for the case of a standard p-i-n diode, a UTC-diode, and a ballistic p-i-n diode, respectively.

In Appendix B we show how quasistationary space charge densities in the intrinsic region may change the band profile of the p-i-n diode in an unfavorable way at high current densities. It is rather tedious to quantify the changes in transport resulting from screening, in particular, when hole transport plays a significant role as in standard p-i-n AEs. A nonuniform electric field leads to spatial variations of the hole velocities and to an increase of the transit times, as

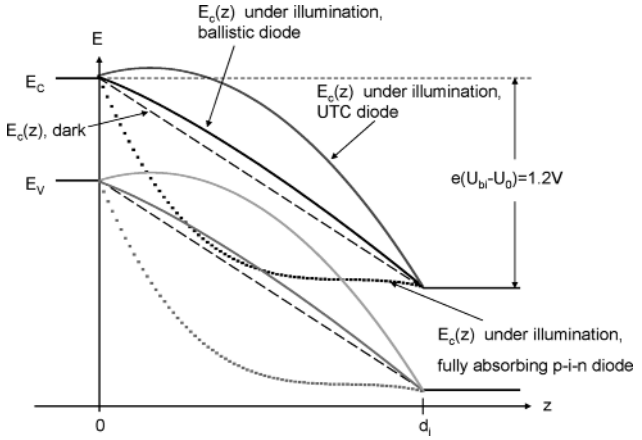

FIG. 10. Screening effects in p-i-n diodes at high current densities for a standard p-i-n diode (dotted, I = 16 mA, non-self-consistent approximate), a UTC diode (gray solid line, I = 16 mA) and a ballistic p-i-n diode (black solid line, I = 40 mA) for a total voltage drop of 1.2 V for the conduction band. The band diagram under dark conditions is shown for comparison in dashed lines. In the standard p-i-n diode, holes are mainly responsible for saturation effects as they become very slow in low field regions of the intrinsic layer. In UTC diodes, field screening due to electrons is responsible for current blocking, constraining electrons from entering the transport layer. Screening has the least impact on ballistic diodes. For better comparison, the saturation effects for a hypothetical diode with $\Delta_{\Gamma L} \geq U_{\mathrm{tot}} = 1.2$ V with ballistic transport all across d_i is shown here. In realistic devices, however, ballistic operation can only be maintained for small field variations within the transport layer (for a 3 dB frequency of 1 THz in InGaAs and GaAs, the maximum field variation is ≈10 kV/cm; see Fig. 7, e.g.), which also imposes a limit on the maximum current.

discussed in Appendix B in more detail. Self-consistent numerical calculations are presented in Refs. 92 and 93. Qualitatively, it is safe to say that current densities, which induce space charge fields close to complete screening of the original uniform field under dark conditions, have to be avoided. They deteriorate the performance dramatically, leading to low-field areas in the diode with practically no or little carrier transport. Simplified model calculations of the influence of screening due to photoinduced space charges and of its influence on the band profiles are presented in Appendix B for the same p-i-n diodes as discussed in Sec. II D 2. It is found that the space charge potential difference between the p- and n-contact layers, ΔV_{sc}, scales according to

$$\Delta U^{sc} \propto \bar{j} d_i^2. \quad (65)$$

If ΔU^{sc} becomes comparable to the potential drop $(U_{bi} + U_0)$, the performance of the mixer becomes affected by the space charge–induced screening of the uniform built-in field in the i-layer. In this case, the THz power can be increased only if the increase of $\bar{j}$ by a factor β is compensated by a reduction of $d_i^{(\mathrm{opt})}$ from Eq. (51) by $\sqrt{\beta}$. This results in an increase of the transit time roll-off frequency by a factor of $\sqrt{\beta}$ at the expense of a decrease of the RC roll-off frequency by the same factor. This change of design affects the performance significantly only at frequencies $v_{THz} < \sqrt{\beta} v_{\mathrm{opt}}$. For $v_{THz} > \sqrt{\beta} v_{\mathrm{opt}}$ one can still take full advantage of the gain in THz power by a factor β^2 associated with the current increase by the factor of β.

a. Standard p-i-n diode. Saturation effects due to the high hole space charge density are apparent at relatively low

current densities in standard p-i-n diodes with low applied voltage. The screening potential of the holes increases linearly with the current, and with the square of the thickness of the intrinsic layer. For an InGaAs diode with our standard geometry ($A = 35\ \mu m^2$, $d_i = 300\,nm$), a photocurrent of $I \geq 13$ mA, and a total bias of $E_G/e - U_0 = 1.2$ V, the electric field in the i-layer becomes strongly inhomogeneous. In particular, the field close to the n-layer is strongly reduced. [This situation is elaborated in more detail in Appendix B, paragraph (c), Fig. 47]. As long as $|\vec{E}| > 3$ kV/cm, the electron transport would not be much affected, as $v_e \geq v_{sat}$, but the hole velocity would be reduced significantly. This implies an increase of positive space charge and an enhanced screening. Therefore, high currents can only be tolerated if the applied voltage is high enough to sustain a finite field at the n-layer. At high reverse bias, however, the heat dissipation due to ohmic losses, $P = IU_0$, becomes much stronger than the heating due to absorbed optical power by a factor of eU_0/E_G. Now, thermal failure of the device limits the acceptable voltage. A better option would be to keep U_0 constant and to compensate for the increase of current by a reduction of d_i as discussed before. As an example, an increase of current by a factor of $\beta = 2$ requires a reduction of the intrinsic layer length by a factor of $\sqrt{\beta}$. Compared to our previous example with $d_i = 300\,nm$, the intrinsic layer should now become 212 nm. At frequencies higher than $\sqrt{\beta} \cdot 0.166\ THz = 0.235\ THz$, the power output of the device increases by a factor of $2^2 = 4$.

b. UTC diode. The problems associated with space charge build-up in the intrinsic layer in p-i-n diodes are drastically reduced when carrier generation is restricted to a narrow region Δz at the p-contact layer. Now, in nearly the whole intrinsic region, only the space charge of the electrons has to be considered, which is inversely proportional to the carrier velocity. The velocity is constant at the high-field saturation velocity v_{sat} in the major part of the i-layer. Apart from the opposite sign, it is also significantly smaller compared to the (positive) space charge density of holes in the standard p-i-n diode where the smaller, field-dependent hole velocity dominates. The resulting space charge potential is depicted in Fig. 10 for the same sample geometry and operation parameters. The effect of the space charge potential on the performance is not detrimental in this case. The space charge creates a current blocking potential close to the p-contact, which can be removed by an increased reverse bias or, alternatively, by introducing background n-doping in the i-layer. Apart from that, the field remains $|\vec{E}| > 3$ kV/cm throughout the intrinsic layer, implying $v_e \geq v_{sat}$. UTC diodes[90] have been operated with current densities around $100\,kA/cm^2$, about an order of magnitude higher than conventional p-i-n diodes.[94]

c. Ballistic diode. In the case of ballistic transport in the i-region, the high carrier velocities prevent a space charge accumulation in the intrinsic zone [see also Appendix B, paragraph (b)]. It is therefore important to maintain ballistic transport throughout the i-layer at high currents. Generally speaking, semiconductors with a high inter-valley separation $\Delta_{\Gamma L}$ like InP and InGaAs, will provide a high (ballistic) carrier velocity.

However, ballistic transport requires optimum field conditions all across the intrinsic layer. Monte Carlo simulations presented in Fig. 7 indicate that fields between 10 and 20 kV/cm are required for optimum operation around 1 THz. Some band bending can be tolerated but for a worst case approximation, we assume a maximum field change in the intrinsic layer of $\delta E = 10$ kV/cm. For a sheet carrier density generated by a THz half wave per unit area, the Poisson equation provides

$$\delta E = \frac{N_s}{\epsilon_0 \epsilon_{sc}}. \tag{66}$$

With $j^{bal} = 2ev_{THz}N_s$ we get

$$j_{max}^{bal} = 2 \cdot \delta E e v_{THz} = 23\ \ kA/cm^2, \tag{67}$$

with $\epsilon_{sc} = 13$. For lower frequencies, the situation is more relaxed as larger field variations, δE, can be tolerated. The maximum ballistic current density j_{max}^{bal} is not expected to drop for lower frequencies. Although this current density is about a factor of 5 smaller than the highest current densities reported for UTC diodes, the strong improvement in the transit time 3 dB frequency of a factor of 6–10 makes ballistic devices very attractive. Even for currents above j_{max}^{bal} the transport will at least be partially ballistic and still improves the device performance compared to operation at the saturation velocity.

Up to now, we have assumed purely intrinsic i-layers in the p-i-n diodes. We have disregarded potential improvements of the performance by tailoring the field in the (quasi) intrinsic region by appropriate doping. For example, a well chosen n-doping allows compensation (or even overcompensation) of field screening by quasistationary electrons in the i-layer. This way it is possible to obtain parabolic band profiles which yield even shorter transit times than those from the estimates for ballistic transport.

4. Heat dissipation

Heating of the sample may also become a challenge in p-i-n diode AEs, in spite of the strongly reduced voltage compared with photoconductive AEs. The most significant temperature-dependent change of the material properties is bandgap shrinking (typically about 0.5 meV/K around 300 K) with increasing lattice temperature. As a consequence, the absorption at a fixed photon energy above the bandgap increases, as does the photocurrent. The thermal conductivity λ_{Th} of GaAs, InGaAs, and InP becomes smaller with increasing temperature. For instance, λ_{Th} of InGaAs and InP decreases with increasing temperature[95] as

$$\lambda_{Th}(T) \approx k(T_0)\left(\frac{T}{T_0}\right)^c, \tag{68}$$

with $c = 1.375$ for lattice-matched InGaAs on InP and $c = 1.55$ for InP. At high thermal load, this effect causes heat accumulation and finally leads to thermal damage of the device.

The risk of thermal destruction is particularly pronounced for InGaAs photomixers because of its low thermal

conductance of 0.05 W/(cm K) compared to 0.68 W/(cm K) for InP and 0.55 W/(cm K) for GaAs.[96] A model calculation for a cylindrical, absorbing InGaAs mesa with thermal transport along the mesa axis is given by Williams and Esman.[97] In that paper, a maximum dissipated power of approximately 45 mW was calculated for a mesa cross section of 79 μm^2 and mesa height of 1 μm, assuming a maximum heating to 120°C as specified by Brown *et al.* for LT-GaAs.[65] This example indicates that thick InGaAs layers in a device structure may lead to serious problems with heating even at moderate laser powers. These values, however, may be overestimated as all the heat was assumed to be transported along the mesa into the substrate. Thermally conductive (but insulating) materials can help to remove heat laterally. Additionally, gold plating on top of the mesa can be applied to waveguide-fed or back-side-illuminated emitters. UTC diodes with an InP transport layer and only thin InGaAs absorption layers benefit from the about 12 times higher heat conductivity of InP of approximately 0.68 W/(cmK).

5. Uni-traveling-carrier diode designs

The (InGaAs) absorption region in UTC diodes[90] is confined close to the p-contact. In order to reduce space charge effects, the absorbing layer is also moderately p-doped on the order of $p = 1 - 10 \cdot 10^{17}\,\mathrm{cm}^{-3}$. A higher bandgap (InP) intrinsic transport layer (see Fig. 11) is attached to allow for electron transport only. Electrons enter into the i-region by diffusion while holes, as majority carriers, stay at the generation region. As only electrons are moving across the intrinsic layer, the device is called a uni-traveling-carrier (UTC) diode. Care is taken to remove the electron barrier in the conduction band at the InGaAs-InP heterojunction. A thin InGaAsP layer between the InGaAs absorber and the InP collection/transport layer divides the single step into two. The transit time 3 dB frequency is given by the (slow) diffusion process through the absorption layer of width w_A and the transit time through the intrinsic layer of width d_i. The transit time performance of a UTC p-i-n diode with a very thin absorption layer was estimated in Sec. II D 2 [see Eq. (61)]. For a sufficient responsivity, however, realistic devices require an absorption layer of the order of 80–100 nm length. Electrons have to diffuse to the transport layer with $v_{\mathrm{diff}} \ll v_{\mathrm{sat}}$. The slow drift and diffusion cause a reduction of the transit time

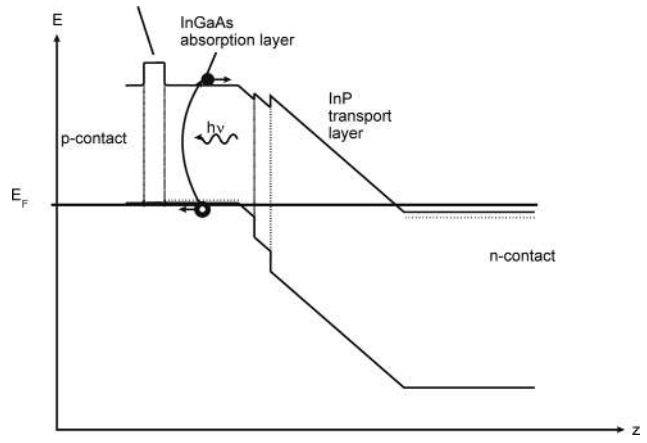

FIG. 11. Band diagram of a uni-traveling-carrier photodiode.

3 dB frequency and was identified as major limiting mechanism.[98] The transit time τ_A through the finite absorption region w_A is approximately given by Shimizu *et al.*[99] as

$$\tau_A = \frac{w_A^2}{2D_e} + \frac{w_A}{v_{th}}, \tag{69}$$

from the drift-diffusion model. Assuming drift with the saturation velocity in the transport layer, v_{sat}, the transit time 3 dB frequency of a device is approximately

$$v_{tr} \approx \frac{1}{2(\tau_A + d_i/v_{\mathrm{sat}})} = \frac{1}{w_A^2/(2D_e) + w_A/v_{th} + d_i/v_{\mathrm{sat}}} \tag{70}$$

where $D_e = \mu_e k_B T/e$ is the electron diffusion constant. At high optical power levels and only moderate doping of the absorbing layer, a small space charge field evolves due to excess holes in the absorbing layer (self-induced bias effect[100]). This field accelerates the electrons and consequently reduces the diffusion/drift time through w_A. Partial ballistic transport of the electrons across the intrinsic layer further improves the 3 dB frequency as was already demonstrated by Ito and Ishibashi.[101] To further reduce space charge effects, the transport layer is often slightly n-doped[102] on the order of a few $10^{16}\,\mathrm{cm}^{-3}$. At typical operating conditions (i.e., current densities up to $j = 100\,\mathrm{kA/cm}^2$), the high absorbed optical power results in space charge effects, usually requiring a small reverse bias in the range of less than 3 V to restore the transport field.

The transport/collection layer length can be chosen according to the required transit time. In the UTC concept, the transit time and RC 3 dB frequency are coupled via the intrinsic layer length d_i as discussed in Sec. II D 1. A compromise between the two limiting roll-off factors has to be found. The UTC approach by Ito and coworkers resulted in an overall 3 dB frequency of 125 GHz[90] ($v_{RC} = 0.21$ THz, $v_{tr} = 0.17$ THz, Fig. 12) at an intrinsic layer length of 282

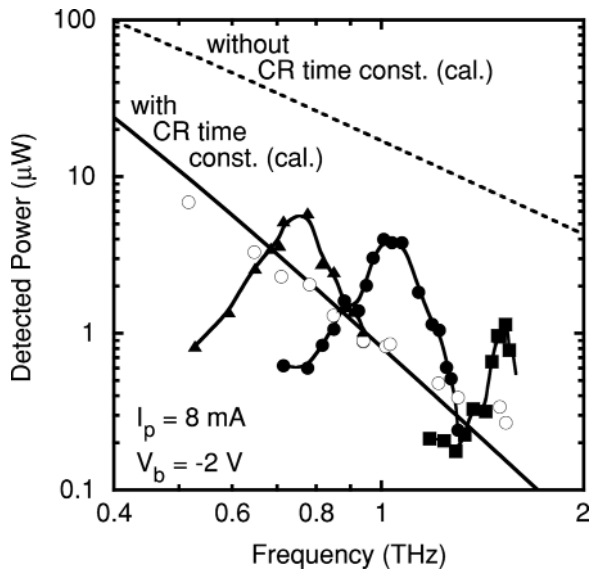

FIG. 12. THz spectrum of a logarithmic-periodic antenna compared to resonant twin dipole antennas. The lower radiation resistance of the twin dipole and its resonant behavior reduce the negative effect of the RC roll-off. Reprinted with permission from F. Nakajima, T. Furuta, and H. Ito, Electron. Lett. **40**, 1297 (2004). © 2004, Institution of Engineering and Technology.

nm, an absorption layer length of $w_A = 98$ nm, and an area of 13 μm^2 with a device optimized for 1 THz, connected to a logarithmic-periodic broadband antenna ($R_A \approx 70\,\Omega$). An output power of 2.6 μW at 1 THz could be demonstrated. A similar device with a resonant antenna provided a maximum power of 10.9 μW at 1 THz, almost 1 order of magnitude more than the best results reported from LT-GaAs switches. For comparison to conventional photodiodes, the UTC device performance saturates at about an order magnitude higher photocurrent.[94]

Even higher absolute power outputs have been achieved with a waveguide-fed approach by Renaud *et al.*[55,103] This device provided a transit time 3 dB frequency of 0.34 THz and an RC 3 dB frequency of 0.254 THz with a resonant antenna. The output power level reached 24 μW at 0.914 THz.

For efficient operation at high frequencies, the device area A can be reduced to increase the RC 3 dB frequency. This also reduces the maximum THz output of the device, $P_{\max} = 1/2R_A I^2$, as the maximum current scales with the area, $I_{\max} = j_{\max} \cdot A$, where $j_{\max}$ is the damage threshold current density. However, a reduction of the device area improves the optical-to-THz conversion efficiency at high frequencies: the RC 3 dB frequency is shifted to higher values as $\nu_{RC} = 2\pi R_A C \sim A$. At frequencies $\nu_{THz} \gg \nu_{RC}$ the THz power is independent of the device area for operation at the maximum current density:

$$P_{THz} = \frac{1}{2} R_A (j_{\max} A)^2 \cdot \frac{1}{1 + (2\pi R_A \epsilon_0 \epsilon_r A / d_i \cdot \nu_{THz})^2} \approx \frac{1}{2} R_A j_{\max}^2 \left(\frac{d_i}{2\pi R_A \epsilon_0 \epsilon_r \cdot \nu_{THz}} \right)^2. \quad (71)$$

This fact led to the development of extremely small photomixers: Record optical-to-THz conversion efficiencies of $9.2 \cdot 10^{-6}$ at 1.04 THz have been reported by Beck and coworkers[105] using a device with only 2 μm diameter and an optical power of only 50 mW ($P_{THz} = 0.46$ μW). For very small device capacitances, parasitic effects prohibit further RC reduction.

At frequencies below their respective 3 dB frequency, UTC diodes have proven to be extremely efficient. Ito and coworkers[54] could demonstrate an output power of 20 mW at 100 GHz by integration in a resonant matching circuit to tune out the imaginary part of the diode impedance. This way, the RC roll-off could be almost eliminated. The responsivity was 0.07 A/W. Prototype devices have already been tested for telecom applications to further increase the data transfer rate,[106] one of the key applications of photomixers. Such applications require a high diode responsivity to circumvent the need for additional amplifiers to reduce the costs. A high responsivity is usually achieved by implementing thick absorber layers such that the transmission is lowered to $T = \exp(-\alpha d) \approx 0$. According to Eq. (70), thick absorbers, however, result in low transit time 3 dB frequencies. This is particularly the case for UTC diodes, where electrons have to diffuse out of the (almost) flat absorber layer. The dilemma of responsivity versus transit time (and operation bandwidth) optimization results in a second tradeoff, in addition to the already mentioned transit and RC limitations. An excellent review of this issue is given in Ref. 94. Photon recycling, e.g., by implementing mirrors or optically resonant cavities to increase the effective optical path length in the device, still allows for high responsivities, even for short absorption layers. Ways to increase the absorption while maintaining short absorption layers will be briefly discussed in Sec. II E. Applications of photomixers to telecom technology will be further discussed in Sec. III D.

Another possible way to reduce the diffusion time of electrons in the absorbing layer could be a negative type II band offset in the conduction band, as proposed by Dyson *et al.*[98] The electrons will then get an initial kick and be accelerated to approximately $\sqrt{2\Delta E/m^*}$, where ΔE is the conduction band offset. Indeed, an increase of the transit time 3 dB frequency of 35% had already been demonstrated by Shimizu *et al.*[99] Here, the band offset was achieved by band filling. The doping was abruptly changed from $2 \cdot 10^{18}\,cm^{-3}$ to $2 \cdot 10^{17}\,cm^{-3}$, resulting in a conduction band offset of 60 meV. An excellent review of UTC diodes is given by Ito *et al.*[90]

6. The n-i-pn-i-p photomixer

The trade-off problem associated with RC and transit time roll-off optimization in p-i-n diodes can be overcome using the n-i-pn-i-p superlattice concept. The capacitance of the device is reduced by growing a stack of N periods of transit time optimized p-i-n diodes with the absorption layer close to the p-layer, connected in series with pn-tunnel junction diodes.[94] The device capacitance simply reduces to $C = C_{\text{pin}}/N$. The transit time and RC optimization are completely decoupled. The connecting np-junction between subsequent p-i-n diodes has to supply an efficient recombination channel to allow for a steady-state current flow through the whole device. Otherwise, photogenerated space charge would build up at the junction and screen the field in the i-layer completely. The band structure of the device in the ground state is shown in Fig. 13.

For an efficient performance, reasonable photocurrents in the mA range have to be carried across the pn junction. For an accordingly small device area this corresponds to current densities of tens of kA/cm^2 at a moderate forward bias of the pn-junction. Such values are quite challenging for pn-diodes and can only be achieved when the carriers can efficiently recombine via midgap states in the bandgap. In the case of GaAs

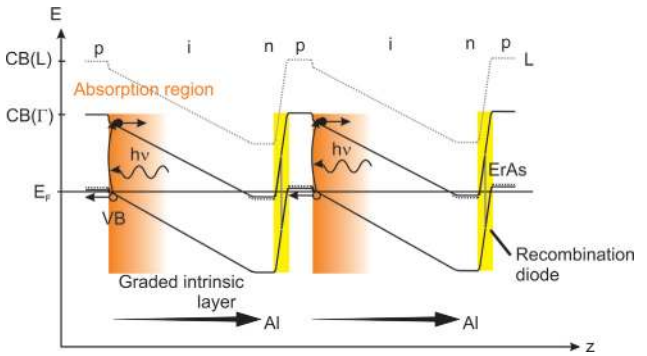

FIG. 13. (Color online) Band structure in the ground state. Yellow: Recombination diode, light orange: Absorption area. The aluminum content of the intrinsic InAlGaAs layer is graded to achieve a confinement of the absorption region close to the p-contact.

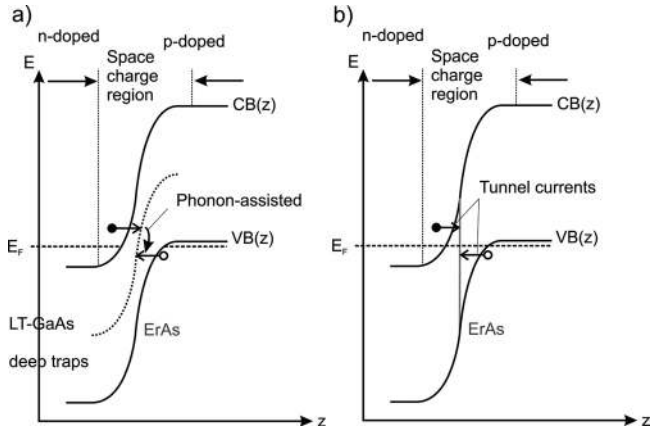

FIG. 14. a) LT-GaAs based recombination diode. b) ErAs-enhanced recombination diode. The tunnel currents are indicated.

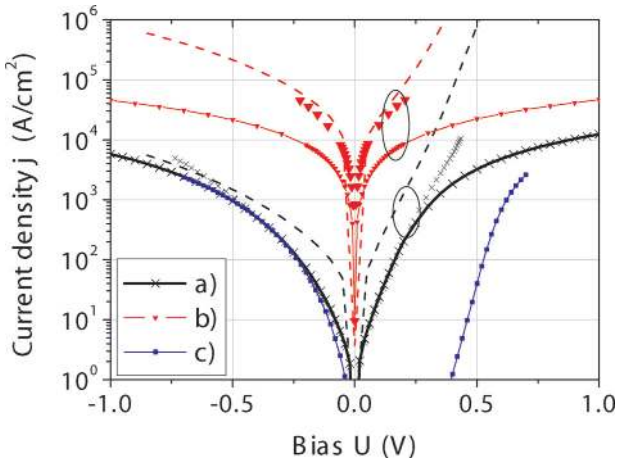

FIG. 15. (Color online) IV characteristics of $In_{0.53}Al_xGa_{0.47-x}As$ recombination diodes with nominal doping levels of (a) $N_D = 5 \times 10^{18}$ cm^{-3}, $N_A(Be) = 7 \times 10^{18}$ cm^{-3} ($x = 0.1$, 1.2 ML ErAs), and (b) $N_D = 10^{19}$ cm^{-3}, $N_A(C) = 2 \times 10^{19}$ cm^{-3} ($x = 0.08$, 1.7 ML ErAs). Lines with symbols: IV characteristics as measured; symbols only: Corrected for a series resistance of 62 Ω [sample (a)] and 22 Ω [sample (b)], respectively. Dashed lines: Calculation. For comparison, the IV characteristics of an aluminum-free pn diode with $N_D = 5 \times 10^{18}$ cm^{-3}, $N_A(Be) = 5 \times 10^{18}$ cm^{-3}, is also shown (c). The ErAs-free diode shows orders of magnitude smaller forward current densities and just reaches similar values in reverse direction as the ErAs-enhanced diode (a) with similar doping levels, despite the lower bandgap [0.75 eV of diode (c) compared to 0.86 eV of diode (a)]. Reprinted with permission from S. Preu, S. Malzer, G. H. Döhler, H. Lu, A. C. Gossard, and L. J. Wang,Semicond. Sci. Technol. **25**, 115004 (2010). © 2010, IOP Publishing Ltd.

emitters, such recombination mechanisms are realized by implementing low-temperature-grown layers (LT-GaAs) between the n- and p-doped layers. LT-GaAs-based recombination diodes provide states close to the middle of the bandgap. To satisfy energy and momentum conservation, phonons are required for carrier tunneling in the LT-GaAs pn-junctions.[107] The use of 1–2 ErAs monolayers (for example in an n-ErAs-p diode) however, turned out to be more efficient. The ErAs-layer supplies quasimetallic states across the bandgap.[107] Electrons and holes can directly tunnel into the ErAs layer and recombine, increasing the maximum recombination current as compared to LT-GaAs-based recombination diodes. A schematic of the band structures of LT-GaAs- and ErAs-based recombination diodes is depicted in Fig. 14. The highest doping levels of the pn junction and narrow bandgaps are key aspects to reduce the tunnel barrier in both cases.[108]

Another advantage of ErAs is that it can also be used in InGaAs-based emitters where growth at low temperatures would not provide efficient recombination diodes. Fig. 15 depicts typical jV characteristics for two recombination diodes with different n- and p-doping levels. Clearly, the reduced tunneling barrier due to higher doping levels improves the tunnel current. For comparison, the theoretical diffusion current of an ErAs-free diode is also depicted.

As a result of the decoupling of transit and RC time, the n-i-pn-i-p concept takes full advantage of ballistic transport. Monte Carlo simulations presented in Fig. 7 predict that intrinsic layers for the InGaAs (GaAs) material system of up to 300 nm (180 nm) are sufficiently short to allow for electron transit time 3 dB frequencies of $1/(2\tau_{tr}) = 1$ THz. Experimentally, however, the need for a confined absorption region close to the p contact requires a graded interface between pure InGaAs (GaAs) and the transport layer with a small amount of aluminum (up to $x = 10\%$ in $In_{0.53}Ga_{0.47-x}Al_xAs$). This results in a higher effective electron mass and a reduced inter-valley gap with increasing Al content. Nevertheless, transit time 3 dB frequencies around 1 THz could be demonstrated in (Al)GaAs structures with intrinsic layers of 150 nm length.[109] In In(Al)-GaAs samples, intrinsic layers around 200 nm (150 nm graded from x = 0 to 8%, followed by 50 nm at x = 8% aluminum) provided transit time 3 dB frequencies around 0.7–1 THz. The band structure of such a sample design is shown in Fig. 13.

Under ballistic transport conditions, the THz power is very sensitive to the external voltage[110] for frequencies higher than the 3 dB frequency obtained by transport with the saturation drift velocity of electrons. The optimum bias point of the emitter is determined by measuring the THz power versus applied voltage. The THz power peaks at the optimum bias, i.e., the optimum transport field strength as depicted in Fig. 16. A too high voltage increases inter-valley scattering and lower biasing results in diminished carrier acceleration. Both cases increase the electron transit time and, hence, reduce the THz power at high frequencies. For optimum transport conditions, a small (typically <1 V per period) external reverse bias (with respect to the p-i-n diode) has to be applied. The optimum bias also depends approximately logarithmically on the optical power as photogenerated carriers induce a forward bias to both the recombination diode and the p-i-n diode. The field in the p-i-n diode decreases and a higher external bias is required to restore the optimum field.

The implementation of a high number of periods, N, allows for larger device cross sections at constant device capacitance. Higher absolute photocurrents at a given maximum current density can be used, strongly increasing the THz power as $P_{THz} \sim I^2$, as long as thermal effects do not limit the power levels. To date the highest output power achieved at 1.02 THz with a broadband antenna ($R_A \approx 70\,\Omega$) is 0.65 μW ± 0.15 μW(corrected for 30% reflection of the silicon lens) with a 3 period InGaAs device with a cross section of 82 μm^2 at an optical power of 190 mW and a photocurrent of 9.5 mA. The intrinsic layer consisted of a 150 nm thick layer with linear Al grading and a 50 nm $In_{0.53}Ga_{0.39}Al_{0.08}As$ layer. The recombination diodes contained 1.2 ML of ErAs and were doped with Si

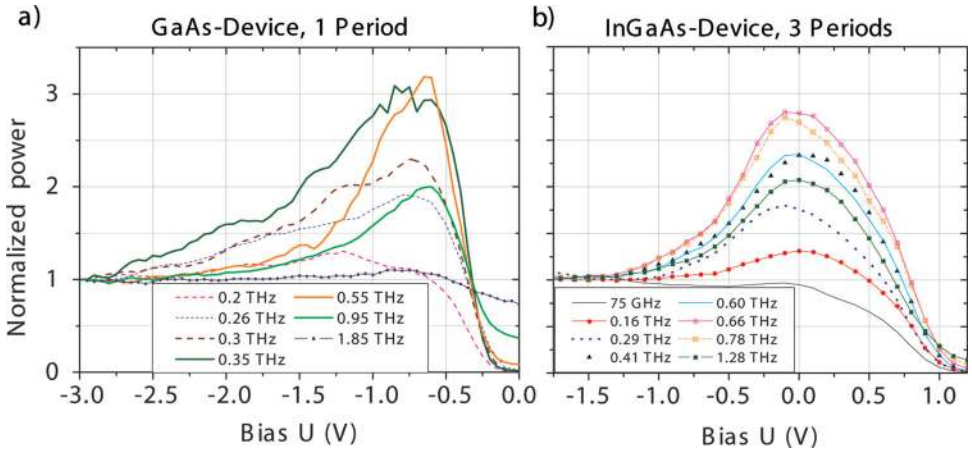

FIG. 16. (Color online) THz power output normalized to the output at −3 V for (a) a GaAs-based device and (b) an InGaAs-based device, normalized at −1.7 V.

($n = 1 \times 10^{19}\,\mathrm{cm}^3$) and Be ($p = 2 \times 10^{19}\,\mathrm{cm}^3$). The transit time 3 dB frequency of this device was close to 1 THz, obtained from the fit in Fig. 17. The Golay cell detector used in these experiments was calibrated with a frequency multiplied Gunn diode at 150 GHz referenced to a Thomas–Keating detector. A second calibration at higher frequencies was referenced to a commercial pyroelectric detector. The calibration resulted in a V_{rms} responsivity of 5900 V/W.

The RC 3 dB frequency of the emitter was calculated from geometry to 0.14 THz when attached to a broadband spiral antenna. The total 3 dB frequency is comparable to that of the UTC diode given by Ito *et al.*,[90] which is a factor of 6 smaller. Using improved recombination diodes, such as the one shown in Fig. 15, and better thermal management should allow for much higher current densities and, subsequently, for a strong increase of THz power. Using a larger number of periods N will allow a shift in the RC 3 dB frequency toward 1 THz. However, care has to be taken to evenly distribute optical power among the periods, which still provides an experimental challenge for a large number of periods.

All p-i-n AEs described in Secs. II D 5 and II D 6 benefit from ballistic transport, particularly the n-i-pn-i-p AEs. Table I summarizes experimental results on p-i-n diode–based AEs found in the literature.

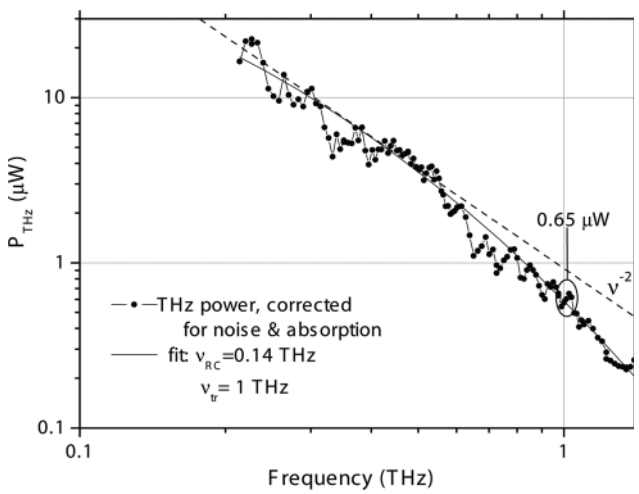

FIG. 17. Output power of a 3 period n-i-pn-i-p photomixer with a broadband spiral antenna, corrected for 30% reflection of the silicon lens. The RC 3 dB frequency is calculated from geometry to 0.14 THz, assuming no parasitic contributions to the antenna or device impedance. The amplitude and the transit time 3 dB frequency are fitted to the data using the expression Eq. (45). The dashed line represents a pure RC roll off.

E. Device layout of AEs

1. Direction of illumination

The direction of laser irradiation is an important aspect of the device layout with respect to the responsivity. GaAs samples are typically grown on a GaAs substrate, which is opaque to photomixing lasers. Such samples can only be illuminated from the top or from the side by a planar waveguide. Illumination from the top requires an optical window in the electrical top contact as depicted in Fig. 18(a). The generated photocurrent has to be transported across the semiconductor layers to the metal top contact. The resistance of the unmetallized optical window is higher and causes ohmic losses (resulting in heat) and inhomogeneous biasing of the photomixer. In photoconductors, the finger electrode structure shadows part of the active area. Thin fingers (less than 1μm) are typically used. For increasing the device responsivity under top illumination, the photomixer can be grown on a Bragg reflector.[111]

InGaAs-based emitters are grown on InP, which is transparent at the mixing wavelength around 1550 nm. This allows for illumination from the backside of the device with several advantages: First, the top metal contact can cover the whole mesa [see Fig. 18(b)] in p-i-n–based AEs, reducing the resistance and heating of the device. Second, the metallic top contact can be used as a mirror, recycling the optical power. Consequently, the absorption profile of the sample needs to be adapted to the resulting optical standing wave pattern. Third, a weakly reflecting Bragg mirror grown below the photomixer would result in an asymmetric Fabry–Perot cavity together with the top metal mirror. In principle, close to 100% of the optical power could be absorbed in the active structure while keeping the intrinsic layer short and the device area small. This would result in an extremely high optical-to-THz conversion efficiency.

Another way to absorb most of the optical power are waveguide-fed photomixers. By connecting the emitter to an on-chip waveguide [either by feeding the optical power sideways into the mesa into the active structure, as illustrated in Fig. 18(c) or by placing the emitter on top of a waveguide,

TABLE I. Highest output powers around 1 THz for p-i-n diode based AEs found in the literature. The implemented antenna type is also shown as resonant antennas typically emit more efficiently than broadband antennas and provide higher RC 3 dB frequencies (cf. Ref. 90 for instance). WG: waveguide design, NA: value not specified by the authors for the given configuration

Type	w_A/d_i [nm]	$A[\mu m^2]$	ν_{tr} [THz]	ν_{RC} [THz]	Antenna	P_{THz} [μW]	Ref.
n-i-pn-i-p	0	82	0.85 ± 0.15	0.14	Log-spiral	0.65	this work
	3×200				($R_A \approx 70\ \Omega$)	(1.02 THz)	
UTC	100	~ 3	NA	NA	TEM-Horn	1.13	[105]
	137				($R_A \sim 50\ \Omega$)	(0.94 THz)	
UTC	98	13	0.17	0.21	Log-periodic	2.6	[90]
	282				($R_A \approx 70\ \Omega$)	(1.04 THz)	
UTC	90	13	≈ 0.17	NA	Twin dipole	10.9	[90]
	282				NA	(1.04 THz)	
UTC	120	60	NA	NA	Resonant slot	24	[54, 103]
	330	(WG)			($\sim 100\ \Omega$)	(0.914 THz)	

Fig. 18(d)][55,94,112] the power is absorbed along the active structure. The mesa length along the optical axis determines the overall absorption. A responsivity as large as 0.2 A/W has been reported[55] for a UTC traveling wave THz photomixer. An excellent review on the responsivity-related layout issues is given by Beling and Campbell.[94] They also included a discussion on traveling wave photomixers, the interconnect between LAE and AE emitters.

2. Packaging

As a result of their sub-mm size, photomixers and antennas can be easily packaged. Several groups provided pigtailed THz heads, fully packaged and not much larger than a matchbox. Some packaging examples are shown in Fig. 19. The photomixing lasers are thus separated from the actual THz head, allowing for handheld operation.

F. Detailed discussion of large area emitters

In Sec. II A we outlined the concept of large area emitters (LAEs). We have shown that LAEs suffer intrinsically from low conversion efficiencies compared to AEs, due to the much smaller radiation resistance. However, the quadratic dependence of THz power on laser power promises high THz power at high laser power. High total laser power does not represent a problem for LAEs if the optical power is distributed over a sufficiently large area. The intensity is then low enough to avoid excessive heating. If the dimensions of the LAE are large compared to λ_{THz}, LAEs have the advantage that all the THz power is emitted into (basically) one direction as a highly collimated beam without the need

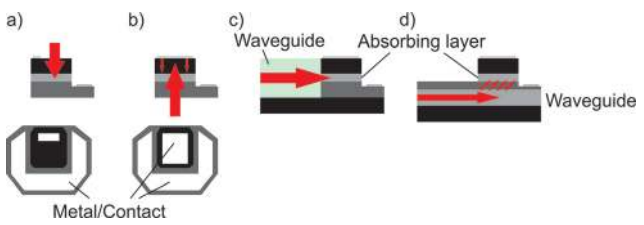

FIG. 18. (Color online) (a) Sample for top-side illumination with optical window. (b) Back-side illuminated sample with a top contact across the whole mesa. (c) and (d) Waveguide-fed deivices.

for any optics. Another important advantage of LAEs is the absence of the RC roll-off due to the much smaller radiation resistance.

In this section, we will discuss the radiation pattern and device efficiency of LAEs in more detail. For most of this discussion, we will focus on CW operation. In this case, we may neglect any feedback of the emitted THz field on the photocurrent of the device, because the emitted THz fields are small compared to the DC fields in the LAE. For pulsed operation, however, the radiated field may cause strong screening of the accelerating DC field.[68,114] In the schematic shown in Fig. 1(a), the direction of the DC electric field in the active layer responsible for the acceleration of the photogenerated carriers had not been specified. As in the case of the antenna emitters discussed in Sec. II B, the electric fields will be typically either in-plane or normal to the surface. The operation of LAEs strongly varies depending on this field orientation. Therefore we will discuss these two cases separately.

1. LAEs with surface-parallel electric field

The geometry depicted in Fig. 20 is the most appealing one with respect to the expected performance. The microscopic dipoles are in the LAE plane, providing optimum emission perpendicular to the surface. Normal incidence of the collimated laser beam [see Fig. 1(a) for $\alpha = 0°$], generates a more or less collimated THz beam (depending on the ratio of beam diameter, ρ_0, to the THz wavelength), propagating mostly into the substrate.

Significant problems arise regarding the implementation of suitable in-plane fields for p-i-n diodes or n-i-pn-i-p structures that have proven to be very efficient as AEs. Due to the vertical growth direction, they are difficult to fabricate in a lateral orientation with reasonable technological effort. Photoconducting emitter concepts have consequently been used for LAEs with in-plane DC fields. The metal electrodes can be patterned on a large area with a single processing step. The electrode spacing s is usually 10 μm or less in order to allow for sufficiently high in-plane electric fields $|\vec{E}| = U_{ext}/s$. The contact fingers can be long (with L_y in the mm range). Gold fingers with a few μm width w are sufficiently large to keep the voltage drop along the electrodes

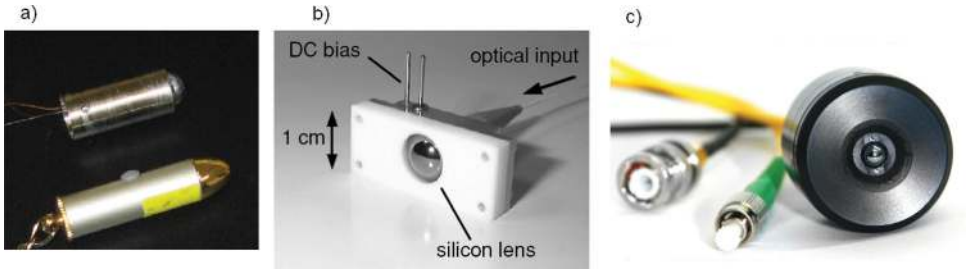

FIG. 19. (Color online) Examples for packaged telecom wavelength–compatible THz photomixers: (a) Pigtailed THz n-i-pn-i-p emitter. A laser pointer is shown for scale. (b) Integrated UTC photodiode sender module, reprinted with permission from H. Ito, F. Nakajima, T. Furuta, K. Yoshino, Y. Hirota, and T. Ishibashi,Electron. Lett. **39**, 1828 (2003). © 2003, Institution of Engineering and Technology. (c) Integrated sender/receiver with a MQW-LT-InGaAs head, courtesy of Fraunhofer-Institut für Nachrichtentechnik, Heinrich-Hertz-Insitute, B. Sartorius, © 2010 Heinrich-Hertz Institute.

small compared to the external bias U_{ext}, which is in the range of a few tens of volts. Unfortunately, neighboring areas of interdigitated contacts yield currents of opposite sign under illumination, as shown schematically in Fig. 20(a). This destroys any THz far field by interference. One possibility to achieve constructive interference in the far field is to block every second gap between the contact stripes by an optically opaque material.[53,115,116] Alternatively, the photoconductive material of every second gap can be etched away.[51] If the substrate material is transparent to the incident optical beam no current will be generated in the etched gaps. Both schemes are depicted in Fig. 20.

To maintain a large active area, the blocked or etched gaps (of width s_{bl}) can be designed much smaller than the active gaps (of width s_a). As no photocurrent is generated in the blocked gaps and the dark currents are very low or even absent in case of etched gaps, negligible electrical power is dissipated. The increase of the electric field $|\vec{E}| = U_{\text{ext}}/s_{bl}$ due to a small gap size, s_{bl}, does not cause problems as long as the breakdown field strength of the photoconductor or substrate is not exceeded.

For calculating the emitted power and its angular distribution, we assume normal incidence of the laser beam of power $P_L(t)$ with a Gaussian intensity distribution

$$I_L(t,\rho) = \frac{P_L(t)}{\pi\rho_0^2}\exp[-(\rho/\rho_0)^2] \tag{72}$$

with $\rho = \sqrt{x^2+y^2}$.

The intensity in the semiconductor decreases exponentially according to $I_L(t,\rho,z) = I_L(t,\rho)\exp(-\alpha z)$, where α is the absorption coefficient. The absorption length Δz (typically $< 1\,\mu m$) is much smaller than the pitch of the contact structure, p, and the THz wavelength λ_{THz}. The (three-dimensional) carrier generation rate $dn(t,\rho,z)/dt \sim I_L(t,\rho,z)/h\nu_0$, as well as the resulting carrier density and current densities can be replaced by the corresponding (two-dimensional) sheet densities. Therefore, the in-plane sheet current densities induced by the electric field can be expressed as $j_{x,s}(t,\rho) = eN^{(2D)}(t,\rho)v_x(t)$. The current sheet density exhibits the same spatial in-plane dependence as the laser intensity, $I_L(t,\rho)$ and can be expressed as

$$\begin{aligned} j_{x,s}(t,\rho) &= eN_0(t)v_x(t)\frac{\exp[-(\rho/\rho_0)^2]}{\pi\rho_0^2} \\ &= j_{s,0}(t)\exp[-(\rho/\rho_0)^2], \end{aligned} \tag{73}$$

with the number of photogenerated carriers given as $N_0(t)$. Both $N_0(t)$ and $v_x(t)$ depend on the details of the system and will be discussed later.

The current density in the individual active gaps s_a is phase coherent within the illuminated area. We now only treat the case of harmonic excitation with $P_L(t) = P_{L,0}[\cos(\omega_{THz}t)+1]$. According to elementary electrodynamics and the Green's function formalism,[117] the THz field generated at a distant point $\vec{r}$ ($r \gg \lambda_{THz}$, i.e., in the far field) depends on the time derivative of the photogenerated current density, according to

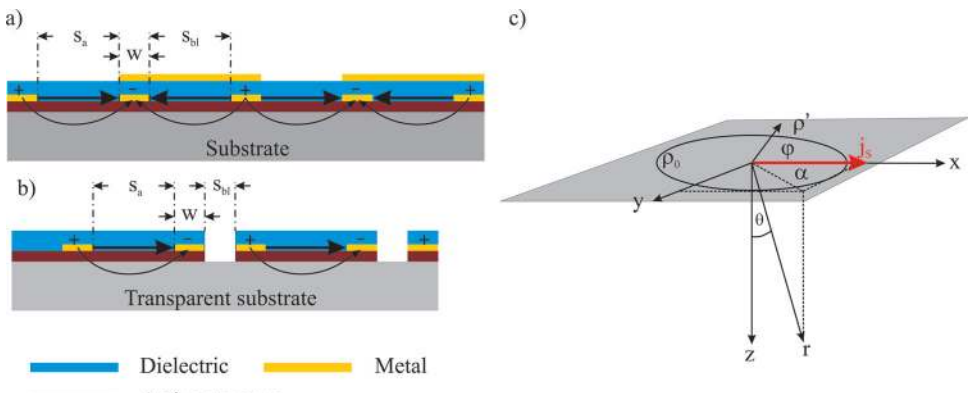

FIG. 20. (Color online) (a) Schematic of the design used by Dreyhaupt *et al.*[53,115,116] The gaps with accelerating fields (indicated by arrows) from right to left are blocked by a metal layer on top of a dielectric spacer. (b) Schematic of the design used by Awad *et al.*[51] The active structure in the odd gaps is etched away. (c) Coordinate system used throughout the calculations.

$$\vec{E}(t,\vec{r}) = -\frac{Zn_{THz}}{4\pi c_0}\int \frac{\vec{r}-\vec{\rho}'}{|\vec{r}-\vec{\rho}'|}\times\left[\frac{\vec{r}-\vec{\rho}'}{|\vec{r}-\vec{\rho}'|}\times\frac{\partial\vec{j}_{x,s}(t,\rho')}{\partial t}\right] \cdot\frac{\exp(ik_{THz}|\vec{r}-\vec{\rho}'|)}{|\vec{r}-\vec{\rho}'|}d^2\rho', \tag{74}$$

where the spherical wave, $[\exp(ikr)]/r$, is the Green's function to the Helmholtz equation and $Z=\sqrt{\mu_0\mu_r/\epsilon_0\epsilon_r}$ is the wave impedance. For calculating the radiated power in the far field, we use the common far field approximation of $\vec{r}-\vec{\rho}'\approx\vec{r}$ for amplitudes. Furthermore, $\vec{k}||\vec{r}$ in the far field such that we can approximate the spherical wave phase fronts as plane waves, i.e., $[\exp(ik_{THz}|\vec{r}-\vec{\rho}'|)]/|\vec{r}-\vec{\rho}'| \approx \{\exp[i\vec{k}\circ(\vec{r}-\vec{\rho}')]\}/|\vec{r}|$. The integral in Eq. (74) simplifies to

$$\vec{E}(t,\vec{r}) = -\frac{Zn_{THz}}{4\pi c_0 r^3}\int \vec{r}\times\left(\vec{r}\times\frac{\partial\vec{j}_{x,s}(t,\rho')}{\partial t}\right) \cdot\exp(i\vec{k}_{THz}\circ(\vec{r}-\vec{\rho}'))d^2\rho'. \tag{75}$$

We introduce polar coordinates for $\vec{r}=r(\sin\theta\cos\varphi,\sin\theta\sin\varphi,\cos\theta)$ and keep $\vec{\rho}'=(x',y',0)$. We get, for the electric field amplitude,

$$|\vec{E}(t,\vec{r})| = \frac{Zn_{THz}}{4\pi rc_0}\cdot|D(t)|\cdot\frac{1}{\pi\rho_0^2}\sqrt{1-\sin^2\theta\cos^2\varphi} \cdot\exp(i\vec{k}_{THz}\circ\vec{r})\cdot\int_{-\infty}^{\infty}\exp\frac{-(x'^2+y'^2)}{\rho_0^2} \cdot\exp(-ik_{THz}x'\sin\theta\cos\varphi - ik_{THz}y'\sin\theta\sin\varphi)dx'dy'. \tag{76}$$

where we introduce the ρ-independent source term $D(t)=\pi\rho_0^2\delta j_{s,0}/\delta t$ which is the time derivative of the integral of Eq. (73), $D(t)=\partial/\partial t\int j_{s,x}(t,\rho')d^2\rho'=\partial/\partial t\,[eN(t)v_x(t)]$. Interpretations of this term will follow later and will also be discussed in detail in Appendix C. This integral is analytically solvable, yielding

$$|\vec{E}(t,\vec{r})| = \frac{Zn_{THz}}{4\pi rc_0}\cdot|D(t)|\sqrt{1-\sin^2\theta\cos^2\varphi} \cdot\exp\left(-\frac{\rho_0^2k_{THz}^2\sin^2\theta}{4}\right). \tag{77}$$

The THz energy flux density is given by the Poynting vector $|\vec{S}_{THz}(\vec{r})|=\frac{1}{Z}|\vec{E}(\vec{r})|^2$. It is parallel to the $\vec{k}$-vector in the far field. We obtain

$$|\vec{S}(t,\vec{r})| = \frac{Zn_{THz}^2}{16\pi^2r^2c_0^2}\cdot|D(t)|^2\cdot(1-\sin^2\theta\cos^2\varphi) \cdot\exp\left(-\frac{\rho_0^2k_{THz}^2\sin^2\theta}{2}\right). \tag{78}$$

The term $(1-\sin^2\theta\cos^2\varphi)=(1-x^2/r^2)=(1-\cos^2\alpha)=\sin^2\alpha$ in Eq. (78) reflects the $\sin^2\alpha$ dependence of the dipole radiation, where α is the angle between $\vec{r}$ and the dipole orientation along the x-axis [see Fig. 20(c)]. This expression, however, is strictly valid only for a dipole in a homogeneous medium. For an emitter placed at an interface between a high refraction index semiconductor and air, the continuity condition for the field components at the boundary leads to a modified angular dependence. The index of refraction n_{THz} must be replaced by a θ-dependent effective index of refraction. Further details are given by Jackson and Alexopoulos.[119] For simplicity, we will continue treating the case of radiation within a homogeneous medium. But we have to keep in mind that the total emitted power has to be modified by an effective dielectric constant. Furthermore, the power will be emitted mainly toward the substrate.

The exponential term in Eq. (78) reflects the destructive interference of contributions from different points (x',y') of the illuminated area at distant points r. Along the z-axis, i.e., at $\theta=0°$, interference effects vanish. This is the direction of maximum power flow. With increasing angle θ, interference effects are more and more important, in particular if $\rho_0k_{THz}>1$. This reflects the fact that the emission becomes more and more directional if the illumination spot size becomes comparable to the wavelength or even larger. The combined effect of the two angular-dependent terms in Eq. (78) is depicted in Fig. 21 for different values of ρ_0/λ. For $\vec{r}$ in the (x,z)-plane, i.e., $\varphi=0°$, the intensity becomes zero at $\theta=\pm90°$, independent of ρ_0, because of the $\sin^2(\theta)$ dependence of the dipole radiation. For $\vec{r}$ in the (y,z)-plane, i.e. $\varphi=90°$, the emission is perpendicular to the current direction and, hence, does not vanish at any angle θ. The angular dependence of the intensity here stems only from the exponential interference term in Eq. (78). For $\rho_0/\lambda\leq0.1$ the intensity distributions differ only slightly from those of an ideal Hertzian dipole.

The total power emitted into the substrate is obtained by integrating the Poynting vector over a hemisphere in the substrate. As the Poynting vector is parallel to the $\vec{r}$ direction, this can be expressed as

$$P_{THz} = \int_0^{\pi/2}\int_0^{2\pi} S(\vec{r})r^2\sin\theta\,d\theta\,d\varphi. \tag{79}$$

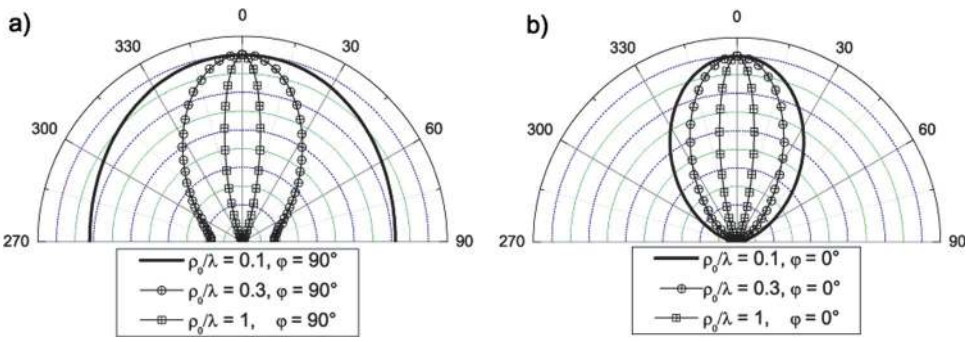

FIG. 21. (Color online) Poynting vectors for (a) out-of-plane ($\varphi=90°$) and (b) in-plane ($\varphi=90°$) polarizations for several values of ρ_0/λ, where $\lambda=\lambda_0/n_{\text{eff}}$ is the wavelength in the medium.

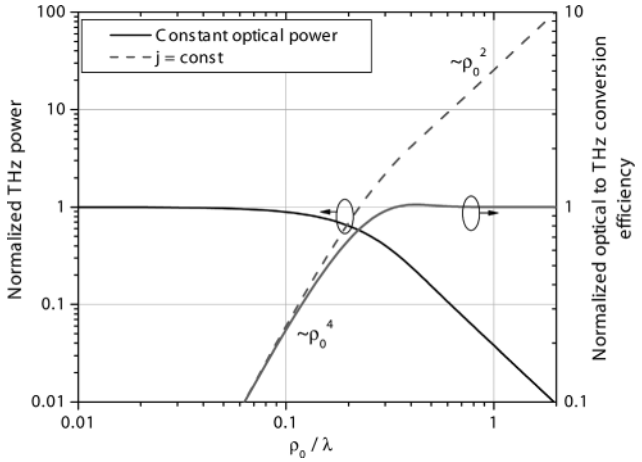

FIG. 22. Normalized THz power for $P_{opt}=$ const and $j_s=$ const for an ideal LAE (left axis). The optical to THz conversion efficiency is also plotted (right axis), normalized to the efficiency at large values of $k_{THz}\rho_0$. The maximum conversion efficiency is already reached at ρ_0/λ=1/3.

Numerical solutions of Eq. (79) are depicted in Fig. 22 as a function of ρ_0/λ_{THz}. The THz power follows approximately a roll-off behavior of

$$P_{THz}(\rho_0/\lambda_{THz}) \approx P_{THz}^{LAQD}\frac{1}{1+\left[b\left(\frac{\rho_0}{\lambda}\right)\right]^2} = P_{THz}^{LAQD}\frac{1}{1+\left[\omega/\omega_\rho\right]^2} \tag{80}$$

with $b=4\pi/\sqrt{6}\approx 5.13$, obtained from the analytical solution of Eq. (79) for $\rho_0 \gg \lambda_{THz}$, and $\omega_\rho = 2\pi c_0/(bn_{THz}\rho_0)$.

The term

$$P_{THz}^{LAQD} = \frac{1}{2}\cdot\frac{Zn_{THz}^2}{6\pi c_0^2}|D(t)|^2, \tag{81}$$

is the power emitted from an LAE in the limit of small spot sizes, ρ_0. For CW operation, we show in Appendix C that the source term $D(t)$ can be interpreted as the time derivative of the dipole current, i.e., the second time derivative of the dipole moment, $p(t)=l_0 q$ with $l_0=gs_a$ and $\partial q(t)/\partial t = I_0^{id}(t)$ with the photoconductive gain g. Eq. (81) then corresponds formally to the power emitted by this Hertzian dipole.[60] We therefore label the power "LAQD" for large area quasidipole.

The discussion so far relates to fixed laser power P_L focused on a spot of varying diameter. We have seen that the total emitted THz power decreases with increasing ρ_0/λ_{THz} as depicted in Fig. 22. In this scenario, the incident optical intensity and the generated current densities at the spot center scales with $1/\rho_0^2$. For maximizing the THz power, however, the intensity at the spot center should remain constant, i.e., at the level of the maximum tolerable intensity. This implies that both the laser power P_L and the photocurrent amplitude I_0^{id} increase with ρ_0^2. The power of the LAQD increases as $P_{THz}^{LAQD}\sim(I_0^{id})^2\sim\rho_0^4$. The maximum THz power vs. ρ_0/λ_{THz} scales as the former expressions multiplied by $(\rho_0/\lambda_{THz})^4$. The emitted total power scales approximately as

$$P_{THz}(\rho_0/\lambda_{THz}) \sim \rho_0^4 \sim P_{L,0}^2 \quad \text{for } \rho_0/\lambda_{THz} \ll b^{-1}\approx 0.2 \tag{82}$$

$$P_{THz}(\rho_0/\lambda_{THz}) \sim \rho_0^2 \sim P_{L,0} \quad \text{for } \rho_0/\lambda_{THz} \gg b^{-1}\approx 0.2 \tag{83}$$

Although in the regime $\rho_0/\lambda_{THz}\gg b^{-1}$ the THz power no longer increases quadratically, but only linearly with the laser power, the power limitation of individual AEs can principally be overcome.

In order to compare the results for LAEs with those of antenna emitters, the source term $D(t)$ in Eq. (81) needs further consideration. We make the same assumptions for the transport as in Sec. II B 1 for photoconductive AEs (i.e., short electron-hole recombination lifetime τ_{rec} and only contributions from the (light) electrons, traveling with constant high-field saturation drift velocity $v_{sat}=10^7$ cm/s). For the details of the calculation, we refer to Appendix C. We find

$$\begin{aligned} D(t) &= \frac{\partial j_{s,0}(t)}{\partial t}\pi\rho_0^2 \\ &= ieN_{av}v_{sat}\omega_{THz}\frac{1}{\sqrt{1+(\omega_{THz}/\omega_\tau)^2}} \\ &\quad\cdot\sin(\omega_{THz}t+\varphi_{THz}). \end{aligned} \tag{84}$$

$N_{av}=\eta_{ext}[P_L,0/(h\nu)]\tau = I_0^{id}\tau$ is the time average of the number of all photogenerated electrons in the sample, with $\tau=\tau_{rec}$ or τ_{tr}, whatever is shorter, and ω_τ is the corresponding 3 dB frequency [either $\omega_\tau=1/\tau_{rec}$ or $\omega_\tau=\pi/(\tau_{tr})$]. $I_0^{id}=\eta_{ext}\ eP_{L,0}/(h\nu_0)$ is the ideal amplitude of the photogenerated THz current at $\omega_{THz}\ll 1/\tau$. We have introduced again the external quantum efficiency $\eta_{ext}=(1-R)s_a/(2w+s_a+s_{bl})$. The amplitude of the THz power of a large area quasidipole becomes

$$P_{THz}^{LAQD} = \frac{1}{2}\cdot\frac{Zn_{THz}^2}{6\pi c_0^2}[v_{sat}\tau\omega_{THz}]^2(I_0^{id})^2\frac{1}{1+(\omega_{THz}/\omega_\tau)^2}, \tag{85}$$

with the LAQD radiation resistance of

$$R_{rad}^{LAQD} = \frac{Z}{6\pi}\left[n_{THz}\frac{v_{sat}\tau\omega_{THz}}{c_0}\right]^2. \tag{86}$$

To obtain the power emitted by the whole LAE, we substitute the expressions for the LAQD, Eqs. (85) and (86), in Eq. (80) to obtain

$$P_{THz}^{LAE} = \frac{1}{2}R_{rad}^{LAE}(I_0^{id})^2\frac{1}{1+(\omega_{THz}/\omega_\tau)^2}, \tag{87}$$

with the formal radiation resistance of the large area array of

$$\begin{aligned} R_{rad}^{LAE} &= R_{rad}^{LAQD}\cdot\frac{1}{1+[bn_{THz}/(2\pi c_0)]^2\cdot[\omega_{THz}\rho_0]^2} \\ &= \frac{Zn_{THz}^2}{6\pi c_0^2}\cdot\frac{(v_{sat}\tau\omega_{THz})^2}{1+(\omega_{THz}/\omega_\rho)^2}. \end{aligned} \tag{88}$$

We will show in Appendix C that an alternative representation of the LAQD radiation resistance in Eq. (86) is in fact the radiation resistance of a Hertzian dipole of length $l_0=gs_a=v_{sat}\tau$. The LAQD radiation resistance and the array radiation resistance in Eq. (88) can be written as

$$R_{rad}^{LAQD} = \frac{Z}{6\pi}\cdot(gsk)^2 \tag{89}$$

$$R_{\mathrm{rad}}^{LAE} = \frac{Z}{6\pi} \cdot \frac{(g s_a k_{THz})^2}{1 + [0.82 k_{THz} \rho_0]^2} \tag{90}$$

Remembering that the total current is the sum of M parallel connected gaps, with an average current of $I_J = I_0^{id}/M$ and, hence, $D_J(t) = D(t)/M$, we can rewrite Eq. (80) as

$$P_{THz}^{LAE}(\rho_0/\lambda_{THz}) = P_{THz}^{J} \frac{M^2}{1 + [b(\frac{\rho_0}{\lambda})]^2} \tag{91}$$

with

$$P_{THz}^{J} = \frac{1}{2} \cdot \frac{Z}{6\pi} (g s_a k_{THz})^2 I_J^2 \cdot \frac{1}{1 + (\omega_{THz}/\omega_\tau)^2} \tag{92}$$

representing the average THz power emitted by a single gap. P_J is the textbook formula[60] for the emitted power of an infinitesimal (Hertzian) dipole of length gs_a with an AC current $I = I_J/\sqrt{1 + (\omega_{THz}/\omega_\tau)^2}$. We can understand Eq. (91) as the power of a single gap times an array factor, $M^2/(1 + [b(\frac{\rho_0}{\lambda})])^2)$ that takes the Gaussian current distribution into account.

The expressions in Eqs. (88) and (90) formally resemble those of the photoconductive AE, but actually differ in the following points:

- The radiation resistance of the LAQD in Eq. (86) increases with ω_{THz}^2. This can be interpreted in terms of a THz-periodic quasiacceleration of the photogenerated carriers with $a = v_{\mathrm{sat}} \omega_{THz}$ for a time $t = \tau$. For material with short lifetime, $\tau = \tau_{\mathrm{rec}}$ and $\omega_{THz}\tau_{\mathrm{rec}} > 1$, this compensates for the lifetime-roll-off.
- The radiation resistance of the LAE from Eq. (88) additionally contains an interference roll-off with a 3 dB frequency of $v_\rho = c_0/(b n_{THz} \rho_0)$. It appears for larger spot sizes where the emission becomes increasingly directional, causing destructive interference off-axis. The radiation resistance saturates at high frequencies to a constant resistance of approximately $30/n_{THz} \cdot (v_{\mathrm{sat}}\tau/\rho_0)^2$ Ω which is considerably smaller than the radiation resistance of antenna-based emitters. Any RC roll-off will be negligible.
- We see from Eqs. (87) and (88) that the THz power does not explicitly depend on the photoconductive gain g (we will discuss the formal appearance of g in the equivalent representation in Eq. (90) in Appendix C). The photoconductive gain, $g = \tau_{\mathrm{rec}}/\tau_{tr}$, typically $g \ll 1$, reduces the THz power of photoconductive AEs by g^2. The THz power emitted by an LAE is only proportional to τ^2, which is either the transit or the recombination time, but not to their ratio g.

For CW operation, materials with short lifetime, τ_{rec} should be used for the same reasons as for AE devices, namely to minimize the power dissipation within the sample and to allow for substantially higher optical driving fields. However, we note that the situation considerably changes for pulsed operation as we will show in connection with an experimental example from Beck *et al.*[53] below. For material with short lifetime, we can set $\tau = \tau_{\mathrm{rec}}$ in all equations. The frequency dependence of a CW-LAE at a fixed spot size, ρ_0, can then be summarized as

$$P_{THz}(v_{THz}) \sim v_{THz}^2 \quad \text{for } v_{THz} < \min(v_\rho, v_{\mathrm{rec}}) \tag{93}$$

$$P_{THz}(v_{THz}) = \mathrm{const}, \quad \text{for } v_{THz} \in [v_\rho, v_{\mathrm{rec}}] \tag{94}$$

$$P_{THz}(v_{THz}) \sim v_{THz}^{-2} \quad \text{for } v_{THz} > \max(v_\rho, v_{\mathrm{rec}}) \tag{95}$$

For comparison with an AE, we estimate the power which may be achieved with a large area photoconducting emitter at 1 THz in the range where the conversion efficiency of the LAE saturates (see Fig. 22). We assume a spot radius of $\rho_0 = \lambda_{\mathrm{eff}}/2 = 58$ μm with $n_{\mathrm{eff}} \approx 2.6$ for most semiconductor materials. This corresponds to an area more than 200 times larger than that of a typical photoconducting antenna emitter, which tolerates about $P_L^{AE} \approx 50$ mW on an area of about 50 μm^2. Assuming further that 75% of the incident radiation is reflected by the contact structure, an optical power of $P_0 = 40$ W can be tolerated. For LT-GaAs, an optical excitation at $h\nu_0 = 1.4$ eV, $\upsilon_{\mathrm{sat}} = 10^7 \mathrm{cm/s}$, and $\tau_{\mathrm{rec}} = \omega_{THz}^{-1} = 160$ fs, then Eqs. (87) and (88) yield, at $\nu_{THz} = 1$ THz,

$$P_{THz} = 10\,\mu\mathrm{W}. \tag{96}$$

This value is already in the range of the best results obtained with AE devices. We should note that, according to our discussion above, this value does not represent an upper limit. Increasing the area while keeping the laser intensity constant will result in a linear increase of the total emitted THz power.

So far there have been no reports on CW-THz generation with LAEs. This may be due to the extremely low conversion efficiency. In the CW example above, the conversion efficiency is only $2.5 \cdot 10^{-7}$. Results for LAEs with in-plane electric fields under pulsed excitation, however, exist. With 50 fs pulses at 800 nm in SI-GaAs, Beck *et al.*[53] have very recently reached a record THz amplitude of 36 kV/cm and a record average THz power of 1.5 mW, emitted from an illuminated area of approximately 1 mm diameter. The average laser power was 800 mW with a repetition rate of $\nu_{\mathrm{rep}} = 250$ kHz. The broadband response peaked at about 0.9 THz. With reference to the energy of the incident laser pulses, they achieved an optical-to-THz power conversion efficiency of $2 \cdot 10^{-3}$, neither taking into account the reflection losses nor the 75% loss of the remaining pulse energy due to the mask.

These values appear surprisingly high compared with the previous estimates for the THz power emitted by CW-LAEs. They result from two favorable factors, which increase the source term, $D(t)$, in Eq. (81). Instead of Eq. (84) we have to use

$$D(t) = \frac{\partial j_{s,0}(t)}{\partial t} \pi \rho_0^2 = e N_{\mathrm{pls}} \frac{\partial v_x}{\partial t} = e N_{\mathrm{pls}} a(t) \tag{97}$$

where N_{pls} is the number of electrons generated (quasi-instantaneously) by each pulse with their subsequent acceleration by $a = \partial v_x/\partial t$. First, N_{pls} may exceed the average number of electrons tolerable for a given spot size under CW operation, N_{av}, by orders of magnitude without causing heating problems. Second, the acceleration a may exceed the quasiacceleration, $v_{\mathrm{sat}}\omega_{THz}$, introduced in our discussion of Eq. (86). N_{pls} is given by

$$N_{\mathrm{pls}} = \frac{\eta_{\mathrm{ext}}}{\nu_{\mathrm{rep}}} \cdot \frac{\bar{P}_0}{h\nu_0}. \tag{98}$$

For the average laser power used by Beck *et al.*[53] ($\bar{P}_L =$ 800 mW, $h\nu_0 =$ 1.4 eV, $\eta_{\mathrm{ext}} = 0.25$, $\nu_{\mathrm{rep}} = 250$ kHz, and $\tau_{\mathrm{pls}} \approx 50$ fs), we obtain $N_{\mathrm{pls}} = 3.6 \cdot 10^{12}$ electrons per pulse. For the semi-insulating GaAs used in by Beck *et al.*,[53] we may assume that the transport of these electrons is quasiballistic. A reasonable approximation for the description of this transport is

to assume quasiballistic acceleration of the electrons by the electric field, $a = e|\vec{E}_x|/m^* = 1.8 \cdot 10^{21}\,\mathrm{cm/s^2}$ for $|\vec{E}_x| = 70\,\mathrm{kV/cm}$ to a maximum ballistic velocity of $v_{\mathrm{bal}} = \sqrt{2\Delta_{\Gamma L}/m^*} \approx 10^8\,\mathrm{cm/s}$. At this velocity, the electron has reached the kinetic energy to enable side valley scattering, which strongly decelerates the electrons. These values are slightly overestimated as LO phonon scattering was neglected. More realistic values for GaAs are presented in Refs. 87 and 120 with $v_{\mathrm{bal}} = 6 \cdot 10^7$ cm/s and $a = v_{\mathrm{bal}}/\tau_{\mathrm{bal}} = 5 \cdot 10^{20}\,\mathrm{cm/s^2}$ with a ballistic flight time of about $\tau_{\mathrm{bal}} = 120$ fs. The acceleration is a factor of 8 larger than the value of the quasiacceleration, $v_{\mathrm{sat}}\omega_{THz} \approx 2\pi \cdot 10^{19}\,\mathrm{cm/s^2}$ in our estimate for the CW-LAE.

For simplicity, we assume that the deceleration takes place on the same time scale, providing

$$\begin{aligned} a &= 5 \cdot 10^{20}\,\mathrm{cm/s^2}, \ \text{for } 0 < t < \tau_{\mathrm{bal}} \\ a &= 5 \cdot 10^{20}\,\mathrm{cm/s^2}, \ \text{for } \tau_{\mathrm{bal}} < t < 2\tau_{\mathrm{bal}} \end{aligned} \tag{99}$$

The current transient yields a broadband single-cycle THz pulse. An ideal photoconductor excited by the acceleration/deceleration pulse described by Eq. (99) yields, for the THz power spectral density in the frequency domain, a Fourier spectrum with a ν^2 increase below its peak at a frequency of $\nu_{THz,p} \approx 3.1$ THz, as depicted in Fig. 23(c). If the sample could be considered to be an LAQD, we would expect a power of $P_{THz}^{LAQD} = [Zn_{THz}^2/(12\pi c_0^2)] \cdot (eN_{pls}a)^2 \tau_{bal} \nu_{rep} = 130$ W. However, the LAE radius is approximately $\rho_0 = 0.5$ mm and it cannot be considered an LAQD. The interference roll-off strongly reduces the emitted power. According to Eq. (88), we expect a ν^2 roll-off with a 3 dB frequency of only $\nu_\rho = c_0/(bn\rho_0) \approx 50$ GHz. Combining the interference roll-off with the Fourier spectrum we would expect a quadratic regime with $P_{THz}^{LAE} \sim \nu_{THz}^2$ for $\nu_{THz} < 50$ GHz and $P_{THz}^{LAE} \sim$ const for 50 GHz $< \nu <$ 3.1 THz, with a strong roll-off above 3.1 THz as depicted in Fig. 23(d). The emitter would provide a total power of approximately 40 mW.

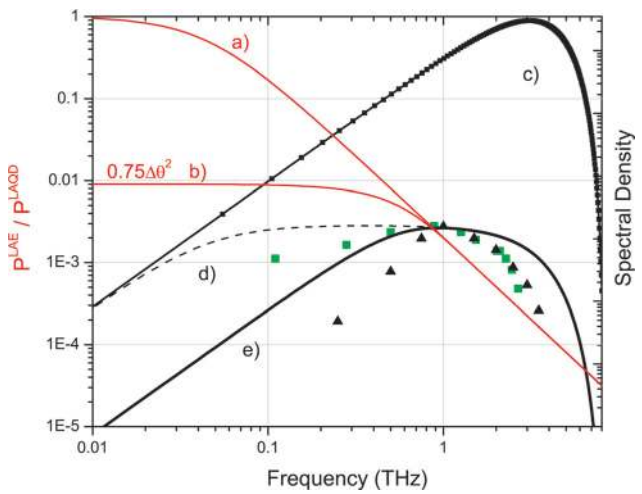

FIG. 23. (Color online) (a) Interference roll-off term for emission into the full 4π solid angle. (b) Power collected by a detector aperture with an aperture of $2\gamma = 46°$, peaking at 0.9 THz. (c) Spectral density of an ideal photoconductor excited by the pulse given in Eq. (99). (d) Spectral density if all power can be collected [i.e., the product of curve (a) and (c)]. (e) Realistic spectral density for an aperture of $2\gamma = 46°$. All spectral densities have been calculated assuming $n_{\mathrm{eff}} = 2.6$. Symbols: Experimental data extracted from Ref. 53 (squares) and from Ref. 115 (triangles), scaled to curve (e).

For comparison with the experiment reported by Beck *et al.*[53] we have, however, to take into account that no focusing optics have been used there. In fact, this does not affect the measured data, as long as the THz beam emitted by the LAE is highly directional. For frequencies smaller than 0.3 THz, the LAE is subwavelength sized with low directivity. The detector will only receive the power emitted into a small volume element of width $\Delta\theta$. However, the authors did not quote the angle of the aperture at which their power spectrum was analyzed. We can estimate the aperture angle, $\Delta\theta$, by matching the experimental peak frequency of 0.9 THz [see Fig. 23(e)]. This provides a value of $\Delta\theta \approx 6.3°$ within the semiconductor. We get the corresponding angle in a vacuum from Snellius's law, of $\gamma = 23°$. The total power obtained by integrating overall frequency components is approximately 35 mW, close to the reported 1.5 mW average power. For the intensities and carrier densities the authors used, we also expect some degradation of the THz power due to feedback of the local THz field on the current (radiation screening)[68] and Coulomb screening,[114] explaining the remaining difference.

Various layouts of LAE emitters have been tested: Matthäus *et al.*[121] used a hexagonal microlens array that focused the THz power only on every second gap of a specifically designed electrode structure. Therefore, no shadowing was required, increasing the external quantum efficiency, η_{ext}. Kim *et al.*[122] used only a single line of an array by applying cylindrical lenses. This, however, results in an asymmetric beam pattern also requiring cylindrical silicon lenses for outcoupling the THz radiation. Nagel *et al.*[51] achieved THz emission from a 1.3 μm thick LT-GaAs layer that was lifted off the SI-GaAs substrate and glued on sapphire. Instead of masking the odd junctions, trenches were etched, removing the photoconductor.

Recently, the LAE emitter concept was also applied to the InGaAsN material system.[123]

2. LAEs with electric field normal to the surface

The origin of the stationary electric field in the z-direction for the acceleration of the photogenerated carriers can be the built-in electric field of a single p-i-n- or n-i-pn-i-p structure, possibly modified by a (small) external bias. For the dynamics of the photogenerated carriers, the considerations for the p-i-n and n-i-pn-i-p AEs as presented in Sec. II D 2 and Appendix A apply. The saturation effects discussed in Appendix B, however, can be principally avoided in LAEs by increasing the illuminated area.

For the extreme case of LAEs with dimensions much larger than λ_{THz}, the wave front of the coherently emitted THz intensity propagates either in the direction of specular reflection or in the direction of refraction [see Fig. 24(a)]. A fundamental disadvantage of the configuration with field normal to the surface is the unfavorable angular dependence of the THz field in the far field. As the velocity and acceleration of the photogenerated carriers is oriented along the z-direction, the intensity of the THz field coherently created within the p-i-n or n-i-pn-i-p structure increases with $\sin\beta$ [Fig. 24 (a)]. If no additional outcoupling optics such as silicon lenses are used, it

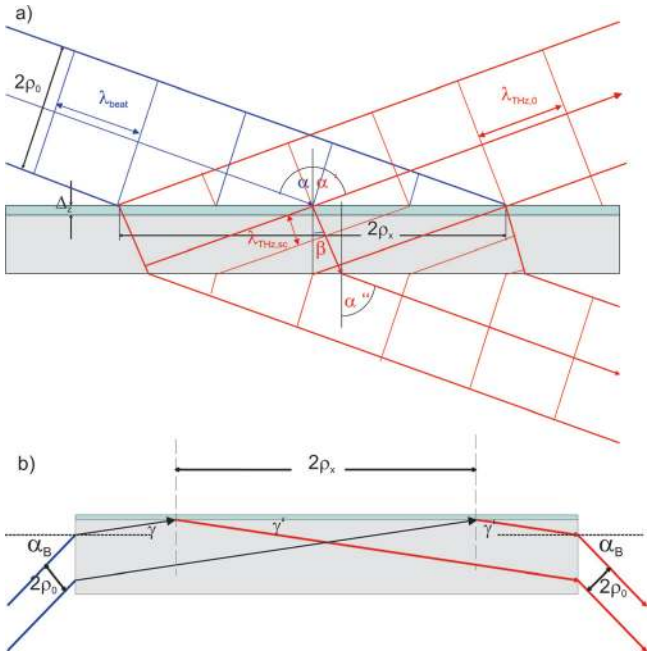

FIG. 24. (Color online) (a) Top-illumination of an LAE. The LAE of thickness Δz generates a THz beam according to Snellius's law. (b) Incidence through a cleaved edge of the semiconductor. The incidence angle on the edge may be chosen to match the Brewster angle, α_B, for improved optical coupling.

is advisable to use the Brewster angle for incidence, i.e., $\arctan \alpha_B = n_{sc} \approx 3.6$, for typical III–V semiconductors. Hence, $\alpha_B = 74.5°$, and $\beta_B = \arcsin(1/n_{sc} \sin \alpha_B) \approx 16.8°$. In this case, a collimated Gaussian beam of width ρ_0 will illuminate an elliptical area with the intensity distribution,

$$I_L(x,y) = \frac{P_L(t)}{\pi \rho_x \rho_y} \exp(-x^2/\rho_x^2) \cdot \exp(-y^2/\rho_y^2), \qquad (100)$$

with the main axes $\rho_y = \rho_0$ and $\rho_x = \rho_0 \tan \alpha_B$, replacing Eq. (72) of the previous section. The total coherently emitted THz intensity attains only $\sin^2 \beta_B \approx 0.08$, i.e., 8% of its optimum value due to the projection of $\vec{k}_{THz}$ on the dipole axis. This applies for both the radiation emitted into air under the reflection angle α' and under the refraction angle β. This disadvantage is at least partially compensated for by a fundamental advantage of photomixers with normal electric fields: The accelerating electric field is oriented in the same direction (i.e., the z- direction) all across the LAE, in contrast to in-plane accelerating fields, where adjacent gaps provide fields with opposite sign (i.e. in $\pm x$-direction). Shadowing masks to remove destructive interference effects of currents with opposite sign are not required. The calculation of the emitted THz power is basically analogous to the procedure presented in the previous section, but the mathematics becomes more complex, due to the more complicated geometry originating from $\alpha \neq 0$.

Therefore, we will confine our discussion of the radiated power to a few simple cases under CW operation.

a. Dimensions $\rho_0 \gg \lambda_{THz}$ for illumination under the Brewster angle. Similar to Sec. II F 1, the emission is strongly directional in the far field $r \gg \lambda_{THz}$. Collimated THz beams will be generated that propagate along the reflection angle α' into air, and the refraction angle β into the substrate. As the THz radiation is p-polarized and leaves the sample again under the Brewster angle, there will be no reflection losses at the interface to the ambient air (assuming that $n_{\text{opt}} \approx n_{THz}$). The angular intensity distribution exhibits circular symmetry relative to the wave vector $\vec{k}_{THz}$. As in the corresponding case for the in-plane LAE with normal incidence (see previous section), the THz beam is slightly divergent. The divergence angle δ decreases with increasing ρ_0. Defining δ as the deviation from the directions of $\vec{k}_{THz}$, we obtain for the angular dependence of the THz fields

$$|\vec{E}_{THz}| = E_{0,THz} \cdot \exp[-(k_{THz}\rho_0/2 \cdot \sin \delta)^2], \qquad (101)$$

analogous to Eq. (77). We note that the illuminated area is increased by the factor $\tan \alpha_B \approx n_{\text{opt}}$ due to the inclined incidence of the optical beam. This implies that the tolerable power for the LAE at a given laser beam radius ρ_0 is increased by a factor n_{opt}, compared to the in-plane LAE. Furthermore, no shadowing masks are required, providing $\eta_{\text{geo}} = 1$. For a comparison between the maximum THz power for the two kinds of LAEs, we assume a fixed optical spot size ρ_0 and operation at the maximum current density, $j_{\max}$. The Poynting vector for the normal field LAE is basically the same as for the in-plane LAE [Eq. (78)], however, with θ replaced by δ and a reduced amplitude of $\sin^2 \beta_B$ due to the inclination angle between the current and the emission axis:

$$\vec{S}(k\rho_0) = \vec{e}_k \frac{Z n_{THz}^2}{16\pi^2 r^2 c_0^2} \cdot |D(t)|^2 \cdot \sin^2(\beta_B + \delta) \cdot \exp[-2(k_{THz}\rho_0/2 \cdot \sin \delta)^2]. \qquad (102)$$

As a result of the requirement of shadowing every second gap in the case of the in-plane LAE, the THz power was reduced by a factor of η_{geo}^2. For the LAE with normal electric field, the power emitted toward the substrate is reduced by $\sin^2 \beta_B \approx 0.28^2 = 0.08$. However, by a factor of $\tan \alpha_B \approx 3.5$, higher optical power may be used due to the larger illuminated area. The product $(\sin \beta_B \cdot \tan \alpha_B)^2 \approx 0.96$ has to be compared to $\eta_{\text{geo}}^2 (\approx 0.062$ in Beck *et al.*,[53] e.g.). This comparison clearly favors the case of emitters with surface-normal acceleration fields, as η_{geo} can hardly reach values close to unity by a sophisticated contact design. Furthermore, p-i-n or n-i-pn-i-p photodiodes may be used as surface-normal field emitters. In Sec. II B 1, we have also seen that p-i-n–based photomixers allow for substantially higher responsivities than LT-GaAs emitters with in-plane fields. In analogy to the previous section, the THz power at constant optical power will drop with ρ_0^{-2}, as a result of destructive interference of emission from different points of the array.

b. Dimensions $\rho_0 \leq \lambda_{THz}/3$. Second, we will again discuss the THz emission for the case of an area which is large compared with the active area of an antenna emitter (AE), but sufficiently small to avoid significant destructive interference of radiation emitted from different points. For the scenario discussed in Sec. II F 1 we had found that the conversion efficiency for the total THz power is significantly

higher than for the extreme case of LAEs with dimensions $\rho_0 \gg \lambda_{THz}$. This also applies to the case of LAEs with currents in the z-direction. For the case of a tilted incidence of the optical beam under an angle α, the argumentation of the last paragraph applies as well, however, with α_B and β_B replaced by α and β. As we have seen in Sec. II F 1, an illuminated area of $\rho_0 \leq \lambda_{THz}/3$ generates a divergent THz beam. A silicon lens is required for efficient outcoupling of the THz radiation.

In the case $\rho_0 \ll \lambda_{THz}$, normal incidence of the laser beam may be the most reasonable choice. Although the power emitted in the z-direction is zero, integration over a hemisphere yields the same power as for the case of in-plane motion of the carriers, as long as destructive interference effects within the LAE remain small. As a result of the orientation of current parallel to the z-direction, we have to keep in mind that most of the power will be emitted parallel to the LAE plane. Therefore, sophisticated optics will be required to collect these contributions efficiently. Due to the radial symmetry, we can restrict our considerations to THz wave vectors in the (x, z)-plane, i.e., $\vec{k}_{THz} = k_{0,THz}(\sin\theta, 0, \cos\theta)$. In analogy to the derivations in Sec. II F 1, we get, in the far field,

$$|\vec{E}(\vec{r})| = \frac{Zn_{THz}}{4\pi r c_0} \cdot |D(t)| \sin\theta \cdot \frac{1}{\pi\rho_0^2} \int \frac{\exp(ik\rho\sin\theta)}{\rho} \cdot \exp\left(-\frac{\rho^2}{\rho_0^2}\right) \rho d\rho d\varphi \tag{103}$$

We see that because of the simpler geometry of $\vec{j} \| \vec{e}_z$, the THz energy flux density at distance r depends only on θ, but not on φ. Eq. (103) can be analytically solved, providing

$$|\vec{E}(r,\theta)| = \frac{Zn_{THz}}{4\pi r c_0} \cdot |D(t)| \sin\theta \exp\left(-\frac{k_{THz}^2 \rho_0^2 \sin^2\theta}{4}\right) \tag{104}$$

for the THz field. Hence, the total power emitted through the substrate into a hyper-hemispherical lens, e.g., is

$$P_{THz} = \frac{Zn_{THz}^2}{8\pi} \cdot |D(t)|^2 \int \sin^3\theta \exp\left(-\frac{k_{THz}^2 \rho_0^2 \sin^2\theta}{2}\right) d\theta. \tag{105}$$

This expression differs from the corresponding Eqs. (78) and (79) for in-plane currents by the different weighting factor for the destructive interference. In the former case, maximum intensity is emitted in the z-direction, for which there is no destructive interference. In the present case, the intensity is zero in the z-direction, whereas the maximum intensity is emitted into the (x, y)-plane, where destructive interference is most strongly pronounced. For comparison, Fig. 25 depicts the angular dependence of $S_{THz}(t, r, \theta)$ for both cases. From Fig. 25 we deduce that for $\rho_0 < 0.1\lambda_{THz,0}/n_{\text{eff}}$(which is only 12 μm for $n_{\text{eff}} = 2.6$ at 1 THz) behaves nearly as an LAQD, whereas for $\rho_0 > 0.3\lambda_{THz,0}/n_{\text{eff}}(= 35\ \mu\text{m})$ the total power is already significantly reduced by the interference roll-off. Hardly any THz power will be collected, unless a very efficient lens is used. At this point, we should mention that the cover of this volume is just depicting the scenario of a large area emitter as discussed above.

Although the configuration with normal incidence of the optical beams is not particularly attractive regarding the expected THz power, it is interesting regarding the polarization

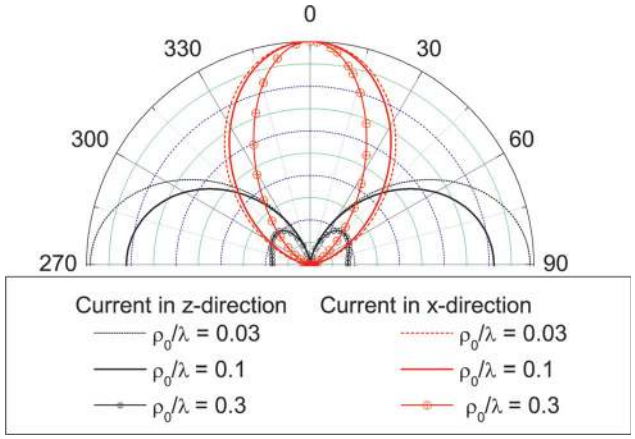

FIG. 25. (Color online) Poynting vector for in-plane (in-plane electric field polarization is shown) and normal oriented THz currents, normalized to the maximum value at $\rho_0 \ll \lambda$.

of the emitted THz beam. It has radial symmetry and exhibits the unusual radial polarization,[124] i.e., the THz field does not contain any tangential component. The focus of a radially polarized beam is smaller than the diffraction-limited spot size for a conventional THz beam. We should note that radially polarized light may also be achieved with in-plane LAEs by a corresponding concentrical contact layout as used by Winnerl *et al.*[125]

c. Grazing angle incidence. As a last example, we discuss the case of laser beams entering the semiconductor structure from the side under a small angle γ, through a semiconductor substrate with larger bandgap and, hence, negligible absorption (InP substrate for InGaAs as the active material, e.g.), as schematically depicted in Fig. 24(b). As the refractive index in the larger bandgap substrate material is typically only slightly smaller than that in the active material, the light will be refracted into the active material without total internal reflection. Total reflection, however, takes place at the interface between the active material and air. Compared with the previous cases, this geometry is much more favorable. The direction of coherent emission nearly coincides with that of maximum THz fields and that of optimum constructive interference.

The energy flux density under an angle δ to the geometric direction of propagation is

$$S(r, \delta, k_{THz}\rho_0) = \frac{Zn_{THz}^2}{16\pi^2 r^2 c_0^2} |D(t)|^2 \sin^2(90^\circ - \gamma + \delta) \cdot \exp\left(-\frac{k_{THz}^2 \rho_0 \sin^2\delta)}{2}\right). \tag{106}$$

The advantage of the present configuration is the much larger value for $\sin^2(90^\circ - \gamma) \approx 1$ compared to $\sin^2\beta_B \approx 0.08$ in configuration (a). Compared to the LAE with in-plane currents, this configuration is also much more favorable, as small values of γ lead to large dimensions of the illuminated area ($\rho_y = \rho_0, \rho_x = \rho_0/\tan\gamma$) but cause only a little destructive interference. The angular distribution of the THz fields exhibits again nearly radial symmetry relative to the γ-direction as in example (a) [Eq. (101)]. Very small angles $\gamma \approx 0^\circ$, however, may lead to destructive interference related

to phase mismatch in the case $n_{THz} \neq n_{opt}$. Further reduction of the THz power arises from absorption of THz radiation in the active layer by free carriers.

In order to obtain estimates of the emitted THz intensity and power, we again have to evaluate the term $D(t)$. In the following, we restrict our calculation to the case of ballistic transport only. In analogy to the case of pulse excitation, Eq. (99), we use for the acceleration and deceleration at time t for electrons generated at time t'

$$\frac{dv}{dt} = e|\vec{E}_z|/m^* = a \quad \text{for } 0 < t' - t < \tau_{bal}. \tag{107}$$

$$\frac{dv}{dt} = -e|\vec{E}_z|/m^* = -a \quad \text{for } \tau_{bal} < t' - t < 2\tau_{bal} \tag{108}$$

We again neglect any hole contribution. For photomixing, the source term $D(t)$ at time t is given by

$$D(t) = e\int_{-\infty}^{t} \frac{dN(t')}{dt'} \cdot \frac{dv(t-t')}{dt'} dt' \tag{109}$$

with the carriers generated at time t' of

$$\frac{dN(t')}{dt'} = \frac{P_{L,0}}{h\nu}\alpha\Delta z_{eff}[1 - \cos(\omega_{THz}t')]. \tag{110}$$

The thickness Δz_{eff} is the effective absorption length in the p-i-n structure, i.e., $\Delta z_{eff} = \Delta z/\cos\beta_B$ for top illumination [Fig. 24(a)] or $\Delta z_{eff} = \Delta z/\sin\gamma$ for grazing incidence. For simplicity, we assumed here that $\alpha\Delta z$ is small and neglected the absorption of optical power along z according to Beer's law. Inserting Eqs. (110) and (108) into Eq. (109) we obtain

$$D(t) = \frac{eP_{L,0}}{h\nu}\alpha\Delta z_{eff}\int_{t-2\tau}^{t-\tau} -a(1 - \cos\omega_{THz}t')dt' + \int_{t-\tau}^{t} a(1 - \cos\omega_{THz}t')dt' \tag{111}$$

Evaluation of the integrals yields

$$D(t) = 2v_{bal}\frac{eP_{L,0}}{h\nu}\alpha\Delta z_{eff}\frac{1 - \cos\omega_{THz}\tau_{bal}}{\omega_{THz}\tau_{bal}} \cdot \sin\{\omega_{THz}[t - \varphi(\tau_{bal})]\}, \tag{112}$$

where we used $a = v_{bal}/\tau_{bal}$. We see that the amplitude of the derivative of the current is proportional to $\omega_{THz}\tau_{bal}$ at lower THz frequencies and exhibits maxima approximately at frequencies

$$v_m = \frac{2m+1}{2\tau_{bal}} \tag{113}$$

For $|\vec{E}_z| = 10$ kV/cm and $\tau_{bal} = 0.5$ ps, maxima of the THz power are expected at about $\nu_{THz} = (2m+1)$ THz. The frequencies of these maxima are expected to scale about linearly with $|\vec{E}_z|$.

The THz power emitted by an ideal large area quasidipole can be expressed by equations similar to Eq. (85)

$$P_{THz}^{LAQD} = \frac{1}{2}\cdot\frac{2Zn_{THz}^2}{3\pi}\cdot\left(\frac{v_{bal}}{c}\cdot\frac{\cos\omega_{THz}\tau_{bal} - 1}{\omega_{THz}\tau_{bal}}\right)^2 \cdot\left(\frac{eP_{L,0}}{h\nu}\alpha\Delta z_{eff}\right)^2. \tag{114}$$

The monotonous ω_{THz}^2 increase of the THz power for in-plane electric fields is replaced by $f(\omega_{THz}\tau_{bal}) = [(\cos\omega_{THz}\tau_{bal} - 1)/(\omega_{THz}\tau_{bal})]^2$ which peaks at $\omega_{THz}\tau_{bal} \approx 0.75\pi$ and a value of $f(0.75\pi) \approx 0.52$. The continuous wave THz power is proportional to v_{bal}^2. In contrast to CW LAEs made from short lifetime material with in-plane currents, the THz power using vertical p-i-n diodes is enhanced by $(v_{bal}/v_{sat})^2 \approx 100$. Therefore, 2 orders of magnitude higher conversion efficiency and THz powers in the mW range are expected.

So far, there are no reports on photomixing based on LAEs with p-i-n diodes with electric field perpendicular to the surface. However, a large number of reports on studies with pulse excitation of semiconductor structures, mostly single or few THz cycles, exists. In most of these investigations, the goal was not the efficient generation of THz radiation, but rather the study of the dynamics of photogenerated carriers in surface depletion layers,[48,49] in semiconductor superlattices,[126] or large electric fields in p-i-n diodes.[120] Therefore, no attempts were made to calibrate the observed signals. A good example of THz generation with LAEs with vertical currents are emitters based on the photo-Dember effect.[47] Electrons and holes are generated close to the surface of a semiconductor. The different mobilities of electrons and holes result in a transient (diffusion) current. The surface field of the semiconductor acts as the accelerating field.

III. EXPERIMENTS WITH CW PHOTOMIXERS AND APPLICATIONS

CW photomixers have a wide range of applications. In this paper, we focus on experiments and applications that take advantage of the high coherence of a CW photomixed THz signal. CW photomixing experiments require two polarization-matched laser signals. A typical schematic 1550 nm photomixing setup is shown in Fig. 26.

Two lasers, typically either distributed feedback (DFB) diodes or grating tuned sources, are polarization matched, coupled, and subsequently amplified by an Erbium-doped fiber amplifier (EDFA) for sufficient power. Either one of the seed sources or the amplified beam is chopped as in most detection mechanisms, the lock-in technique is required to distinguish the THz signal from the far-infrared background. A simple mechanical chopper wheel can be used but, alternatively, many setups allow for an electrical power modulation of one of the sources. Chopping only one beam while working in the saturated regime of the EDFA bears the advantage that the output power of the amplifier remains almost constant. Thus, thermal noise caused by heating of the device is not modulated, reducing the amplitude noise of the system when a broadband detector is used, such as a Golay cell. The amplified lasers drive a photomixer that is mounted on a

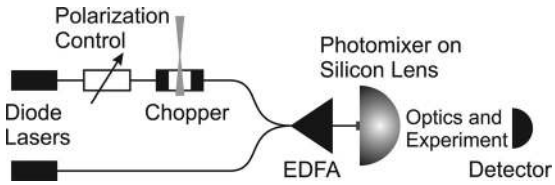

FIG. 26. Typical 1550 nm fiber-based, nonpolarization-maintaining photomixing setup.

hyperhemispherical, high-resistivity silicon lens to prevent total internal reflection at the semiconductor–air interface of the outcoupled THz beam. The optimum hyperhemispherical offset in terms of Gaussicity and transmitted power is around r/n, where r is the radius of the lens and n is its index of refraction.[127] The free space THz beam can then be shaped and guided with parabolic mirrors or waveguides,[128] such as brass tube waveguides[129] or dielectric waveguides.[130,131] Due to the lack of low loss Terahertz materials, waveguides tend to be lossy and can only be used to cover short distances.

A. Interference-based Terahertz optics

A simple demonstration of the coherence of the THz beams is Young's double slit experiment. As an example, we use slits spaced by $a = 4$ mm and widths of 0.5 mm (or 1 mm). Fig. 27(a) shows the far field pattern detected by a Golay cell for 0.23 THz and the two types of slits used. The angles of the first and second order peaks agree well with the theoretical expectation, $\alpha_m = \arcsin(m\lambda/a)$, where m is the order of the peak, as depicted in Fig. 27.

Such an experiment was also carried out to study the resolution of a THz-time domain spectroscopy (TDS) system.[5] Here, however, the temporal data at each pixel had to be Fourier transformed to get the wavelength-dependent interference pattern. The CW system, in contrast, provides Young's interference pattern right away.

Due to the long wavelength of hundreds of microns to several millimeters, THz optics are fairly large. This moves feature sizes from the nm range of instruments for visible light to the easy to handle and visible-by-eye (sub-)mm range. Often, the function of a device can be directly recognized, e.g., that of (wire grid) polarizers[132] or, as we show in the following, a blazed grating. For a given incidence angle, the reflection condition $\alpha_{in} = \alpha_{out}$ coincides only for one specific wavelength with the grating condition, $m\lambda = g(\sin\alpha_{out} - \sin\alpha_{in})$ of the m[th] order, with g being the grating period. For this wavelength, most of the power is concentrated in this peak. Here, the blaze angle is 15° and the grating period is 2.1 mm. The experimental peak position of the first order was found to agree well with the theoretical expectation as depicted in Fig. 28.

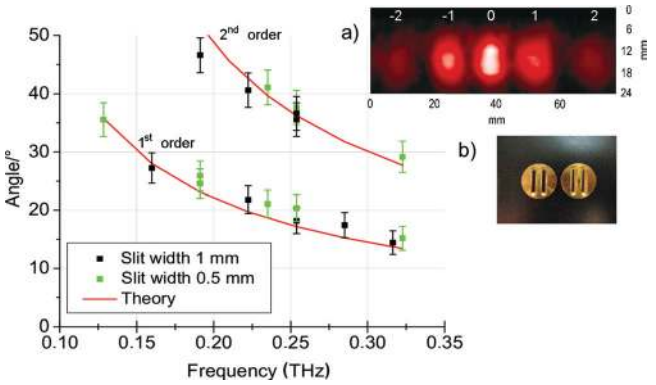

FIG. 27. (Color online) Peaks of the interference pattern of 1 mm and 0.5 mm wide double slits. Inset (a) Far field pattern at 35 mm distance of 0.5 mm wide double slits. Inset (b) The used double slits.

For splitting a THz beam, dielectric quartz wafers or undoped, high resistivity silicon wafers are frequently used. Both dielectric–air interfaces reflect part of the incoming beam, causing multiple interference. The splitting ratio therefore is strongly wavelength- and thickness-dependent. For thin wafers, ($d \leq \lambda_{THz}$), the free spectral range is approximately $\Delta\nu = c_0/(2dn_{THz})\cos[\arcsin(\alpha)/n]$ for a tilt angle α. High-index materials are very attractive to obtain almost α-independent characteristics.[133] Recently, the first fiber-based couplers/splitters have been reported.[134] In analogy to optical splitters/combiners, two subwavelength polyethylene fibers were glued together for a coupling distance d_C. Interference along this coupling length transfers power from one fiber to the other.

Another well-known interference-based optical element is the Bragg mirror. Different types of THz Bragg reflectors have been developed. Cheap commercial plastics with slightly different indices of refraction and thicknesses around 100 μm were stacked,[135] but as a result of very similar indices of refraction, the reflectivity of this mirror was rather low. Instead, a stack of air-separated (with a gap of 200 μm), 100 μm thick polyethylene (PE) plastic films showed an approximately 100 GHz wide transmission window.[135] Such Bragg mirrors are very easily disturbed by air flows. A solid-

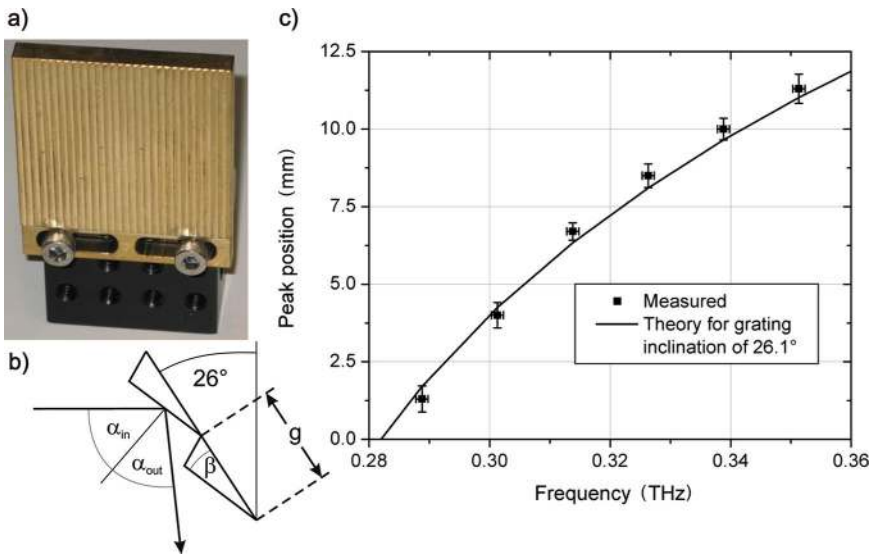

FIG. 28. (Color online) (a) The blazed grating. (b) Schematic of the grating. (c) Occurrence of the peaks for a tilt angle of $\beta = 26.1°$, compared to the theoretical expectation.

state solution with high refractive index difference between low and high n material would be preferable. Thus, nonflexible Bragg mirrors consisting of high resistive silicon and polypropylene (PP) plastic were designed,[136] showing a transmission band of 55 GHz for all polarizations and incidence angles. The latter is mainly attributed to the high index contrast of $\Delta n \approx 1.9$. Such mirrors are nonflexible and also more expensive than pure plastic mirrors. A compromise presented by Jansen *et al.*[137] uses a composition of standard polypropylene (PP) or polyvinylidene fluoride (PVDF) plastic (low $n \approx 1.5$) and plastics doped with up to 60% titania (TiO_2), providing an index of refraction of $n > 3$. Thus, a similar performance as the Si-plastic mirror could be demostrated while keeping the flexibility of the material and -on principle- the possibility of cheap production.

B. Measurement of the photomixer coherence length and applications

For characterizing interference-based optical elements as presented in the last section, only fairly short coherence lengths (in the range of the wavelength) are required. CW photomixers, however, can produce highly coherent signals. The high coherence offers a wide range of applications. We will point out a few of these applications in this section.

In contrast to other free running THz sources such as QCLs, frequency multiplied Gunn or Impatt diodes, spatially separated photomixers are mutually coherent when operated by the same pair of lasers. The THz linewidth basically depends on the linewidth of the lasers. The emission of several coherent photomixers can be interfered to improve the spatial resolution of CW THz stand-off imaging systems while increasing the available photomixing power at the same time. The setup for measuring the coherence length is depicted in Fig. 29.

The beams of two commercial telecom lasers with frequencies ν_1, ν_2, (one of them is chopped) and linewidths of a few MHz are coupled into an EDFA to provide sufficient power. Then, the signal is split in two by a beam splitter to drive two separate photomixers (PM1, PM2). A Si-beam splitter (Si-BS) combines the THz beams and a parabolic mirror focuses the signal on a Golay cell detector. In one optical and one THz arm, delay stages are incorporated in this Mach-Zehnder-like setup. By scanning one of the stages by Δl in the range of a few wavelengths, the path difference, $\Delta s = 2 \cdot \Delta l$, is altered. The relative phase between the two THz beams shifts according to $\Delta\varphi = k \cdot \Delta s = 4\pi/\lambda \cdot \Delta l$. Interference fringes occur with a period of λ_{THz} for sufficient coherence. The fringe visibility defined as $V = (P_{\max} - P_{\min})/(P_{\max} + P_{\min})$ determines the mutual coherence of the two beams where $P_{\max}$ and $P_{\min}$ are the maximum and the minimum power of the interference fringes, respectively. In the next step, a longer delay d (in the range of some meters) is introduced in the optical path. By approaching the coherence length of the beam, the visibility is continuously reduced according to

$$V(d) = V_0 \cdot e^{-2x^2/l_{\text{coh}}^2} \quad \text{with } l_{\text{coh}} = \frac{2}{\pi}\frac{\sqrt{2\ln 2}}{\Delta\nu_{HWHM}}. \tag{115}$$

An exponential fit to the data in Fig. 30 provides a HWHM linewidth of the THz signal of 8.3 MHz (coherence length of 13.6 m). This is very close to the coherence length of the lasers determined by the linewidth of a few MHz. It can be stated that photomixers spaced by less than the coherence length are mutually coherent.

Using highly stabilized lasers[139,140,149] allows for much longer coherence lengths, as we will see later in Sec. III B 2.

1. THz photomixer array concepts

The mutual coherence can be used to enhance the maximum available photomixing power. As mentioned in Sec. II D 5, the highest output power from a photomixer close to 1 THz was 24 μW at 0.914 THz.[55,61] To further increase the maximum output power, the power of several (N) mutually coherent emitters on a single chip can be combined.[57,141] A single source at the position $\vec{r}_j$ provides an electric field of

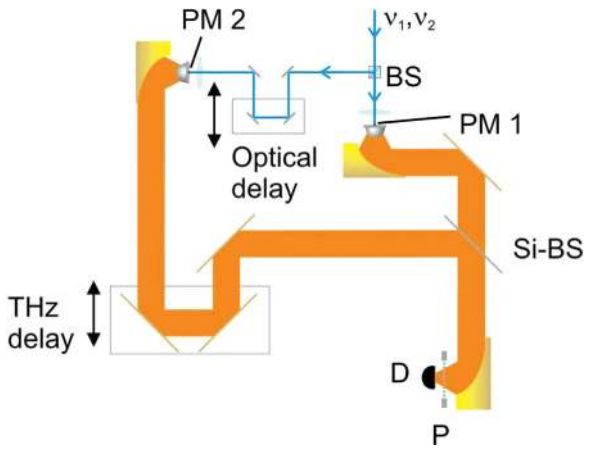

FIG. 29. (Color online) Setup for measuring the temporal coherence. Reprinted with permission from S. Preu, S. Malzer, G. H. Döhler, Q. Z. Zhao, M. Hanson, J. D. Zimmerman, A. C. Gossard, and L. J. Wang, Appl. Phys. Lett. **92**, 221107 (2008). © 2008, American Institute of Physics.

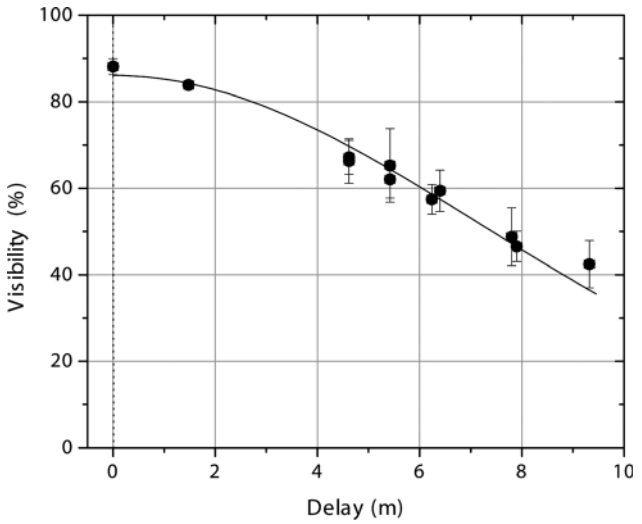

FIG. 30. Fringe visibility versus path delay. The exponential fit provides a coherence length of 13.6 m. Reprinted with permission from S. Preu, S. Malzer, G. H. Döhler, Q. Z. Zhao, M. Hanson, J. D. Zimmerman, A. C. Gossard, and L. J. Wang, Appl. Phys. Lett. **92**, 221107 (2008). © 2008, American Institute of Physics.

$$\vec{E}_j(\vec{r},t) = \vec{E}_{0,j}(\vec{r}-\vec{r}_j)\cdot e^{i(\vec{k}\circ(\vec{r}-\vec{r}_j)-\omega t-\varphi_j)}. \quad (116)$$

The relative phase of $\varphi_j = \Delta s_j \cdot 2\pi/\lambda$ can be chosen by the relative optical path length, Δs_j. All photomixers emit mutually coherent, if the optical path length difference of the driving laser field is much less than the coherence length. Constructive interference occurs provided that the polarizations of the emitters are the same, and the phases of all fields at a point $\vec{r}$ are the same modulo 2π

$$\Phi_j(\vec{r}) = \vec{k}\circ(\vec{r}-\vec{r}_j) - \varphi_j = n\cdot 2\pi, \quad (117)$$

where n is any integer. The total intensity becomes

$$I_{tot}(\vec{r}) = \left|\Sigma_{j=0}^{N}\vec{E}_j(\vec{r},t)\right|^2 = \left|e^{-i\omega t}\Sigma_{j=0}^{N}E_{0,j}(\vec{r}-\vec{r}_j)\right|^2 = \left|\Sigma_{j=0}^{N}E_{0,j}(\vec{r}-\vec{r}_j)\right|^2. \quad (118)$$

If all devices emit the same power, $E_{0,j}(\vec{r}-\vec{r}_j) \approx E_0(\vec{r}) = \sqrt{I_0(\vec{r})}$, the sum breaks down to $I_{tot}(\vec{r}) = |N\cdot E_0|^2 = N^2 I_0$. That is, the intensity increases by N^2 instead of just N. This is a result of a reduction of the beam width w caused by interference.[141] In contrast, incoherent combination does not reduce the beam width. The intensity only increases by a factor of N. It is fairly simple to achieve mutual coherence, as commercial DFB diodes and many other laser sources provide linewidths in the MHz range or below. Such narrow linewidths result in coherence lengths in the range of several meters, much more than is required for most applications. Coherent combination not only provides enhanced intensity; the reduced beam width of the central interference peak facilitates the detection of the beam. If enough sources are implemented on a single chip, the silicon lens will no longer be necessary to outcouple the THz beam through the semiconductor–air interface, similar to an LAE emitter. The majority of the THz light will be emitted almost perpendicular, as the emission lobe will be very narrow. The sidelobes will be strongly suppressed for a large number of densely spaced emitters. The concept of coherent combination allows for beam steering by a careful choice of the relative phases $\Phi_j(\vec{r})$ such that the interference occurs off axis. This is simply achieved by introducing path delays of $l_j = j\cdot\lambda\Delta\Phi/2\pi$ for the j^{th} emitter of a row. The initial phase of the sources is then altered by $\varphi_j = j\cdot\Delta\Phi$. Commercially available fiber-optic stages may be used to control the relative path delays. This concept resembles the LAE approach in transmission geometry, however, with discretized AE. For LAE devices, the path delay originates from an inclined optical beam.

This concept of a THz phased array, as proposed by Brown[57], e.g., was followed up by Ito and co-workers[142] to enhance the maximum available photomixing power. At 0.3 THz, a single UTC device reached 120 μW of output power. An EDFA provides enough power to drive a 3×3 UTC photodiode array. A 1:9 star coupler is used to distribute the power to the individual emitters by optical fibers. However, only a single line of the array (i.e. a 3×1 array) could be investigated in detail. If the THz phase of all elements is the same, constructive interference occurs perpendicular to the array plane, i.e., under broadside emission. The main lobe-width could be reduced by a factor of 2, proving coherent interaction of the sources. In addition, the implementation of a phase delay between the elements of $\Delta\Phi = 2\pi/5$ ($\Delta l = 0.2$ mm) allowed steering of the THz beam by 20°, in very good agreement with the theoretical expectation.

A similar experiment with LT-GaAs photomixers was carried out with a 3×3 dipole array emitting around 0.3 THz with free space optical beams.[143] A microlens array with a lattice constant matched to the emitter spacing of 250 μm was placed in front of the devices to focus the beams on the individual elements. The filling factor of the microlenses is about 72% so that most of the light is focused on the semiconductor surface. Instead of the introduction of a path delay, the relative phase between neighboring devices is introduced by a tilt angle between the two near-IR laser beams (see Fig. 31, similar to a traveling wave approach[144]). The phase difference between two adjacent sources becomes

$$\Delta\Phi = d\cdot(k_1\sin\alpha_1 - k_2\sin\alpha_2) \approx d\cdot k\cdot(\sin\alpha_1 - \sin\alpha_2), \quad (119)$$

where $k_i = 2\pi/\lambda_i$ is the optical wave vector and α_i is the angle of incidence of the laser beam i. For $\alpha_2 = 90°$, Eq. (119) reduces to $\Delta\Phi \approx d\cdot k\cdot\sin\alpha$, with α being the inclination angle of the tilted beam. This way, the phase relation between all emitters for achieving off-axis constructive interference is automatically set correctly by changing a single parameter, the tilt angle α, instead of aligning $N-1=8$ delay stages. Note that the angle of constructive interference of the THz beam is amplified by the ratio of the THz to the optical wavelength. Very small inclination angles α in the mrad range are sufficient to achieve a 2π phase change between the emitters. The emission angle β_n appears at

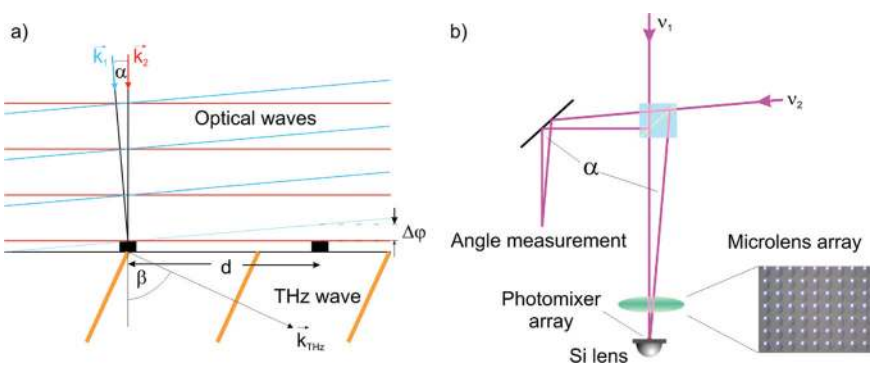

FIG. 31. (Color online) (a) Schematic phase fronts of optical and THz waves. (b) Setup for setting the mixing angle.

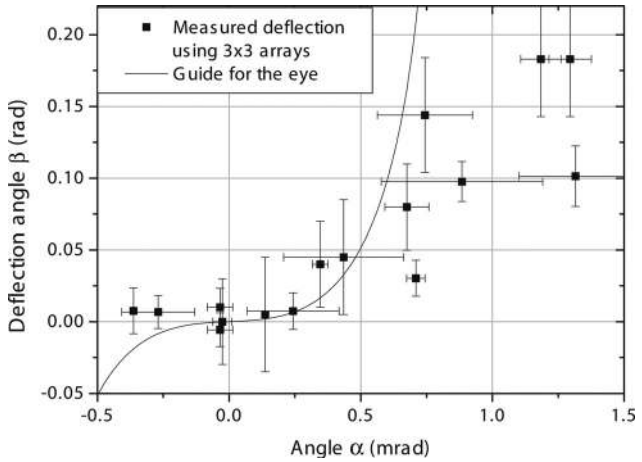

FIG. 32. Emission angle (β) of a coherently driven LT-GaAs array versus optical beam inclination angle (α). Despite the array being mounted on a hyperhemispherical silicon lens that reduces the emission angle, beam deflection could be measured. The focusing property of the silicon lens is responsible for reduced deflection at large angles, α.

$$\beta_n = \arcsin\{\lambda_{THz}/d \cdot [\Delta\Phi/(2\pi) - n]\}, \tag{120}$$

where n is an integer. A schematic setup is depicted in Fig. 31.

Here, deflection of the beam by changing the relative phases was demonstrated, proving the coherent superposition of the THz signals. The presence of the silicon lens, however, makes it fairly difficult to compare the measured deflection angles with theoretical expectations. The results and a scaled theoretical curve as a guide for the eye are depicted in Fig. 32.

Such on-chip arrays have several disadvantages. In the case of a fiber-fed array, unbalanced splitting and inadequate alignment accuracy of the fibers with respect to the photomixers causes unequal power distribution. The latter was the reason for only investigating a single row rather than the full 3×3 UTC photomixer array. In the case of the free space setup, the Gaussian shape of the optical beam, misalignment, and lens errors of the microlens array hinder evenly distributing the optical power. In both cases, bias lines to each single element are necessary. Various cross talk effects between the antennas and through the bias lines influence the antenna performance. This requires tedious simulations. Optimum performance may just be expected for a specific emission angle and frequency. The small distance of the individual elements, on the order of the THz wavelength or less, impede the implementation of broadband antennas. Tunability is limited, which is one of the greatest advantages of photomixers.

As commercially available sources allow for coherence lengths of several meters, there is, in fact, no need to implement all emitters on a single chip. Another approach implements coherent combination of the THz beams of individually packaged and pigtailed single emitters, each with its own silicon lens and imaging/focusing optics.[141] This way, broadband antennas can be implemented, there are no cross talk effects, and the alignment of the fibers to the photomixers is facilitated. For adequately large apertures, such a system is capable of providing enough CW THz power for stand-off imaging, even at a distance of several meters. A typical setup is depicted in Fig. 33.

The interference of the sources allows for generating any interference pattern, ranging from regular lattices of peaks with similar power levels to patterns with a very pronounced center peak. Some examples are given in Fig. 34. The pattern only depends on the phase relations and source positions. High intensities in one peak can be generated by emitters with relatively small apertures. Interference patterns were numerically calculated by Preu *et al.*[141] for a target distance of 30 m. For the calculation, Gaussian THz beams are assumed. The emitter phase is chosen such that constructive interference occurs on the optical axis 30 m away from the emitter plane. To achieve constructive interference at a target point $\vec{r} = \vec{\rho}$ for all wavelengths, the phase, in Eq. (117), of all beams at this point has to be wavelength-independent. The relative phase offset of the source, φ_j, must be chosen as

$$\varphi_j = k \cdot \Delta s_j = \vec{k}(\vec{\rho} - \vec{r}_j) \Rightarrow \Delta s_j = |\vec{\rho} - \vec{r}_j|. \tag{121}$$

For sources that are set up in a plane, wavelength-independent constructive interference at $\vec{\rho}$ can be achieved by implementing a small delay path of $\Delta s_j = |\vec{\rho} - \vec{r}_j|$. Alternatively, the emitters can be aligned on a sphere with radius $|\vec{\rho}|$, in which the optical path length difference Δs_j is zero for all sources. In-line delay stages are not required, given that all fibers have the same length.

For long distances, ρ, the maximum (ideal) focal length of a Gaussian beam is given by

$$f_{\max} = \frac{\pi r_A^2}{2\lambda} \quad \text{for } \rho > f_{\max} \tag{122}$$

$$f = \rho \text{ else}, \tag{123}$$

where r_A is the radius of the imaging optics of a source. For Eq. (122) we assumed the e^{-2} beam waist is matched to r_A.

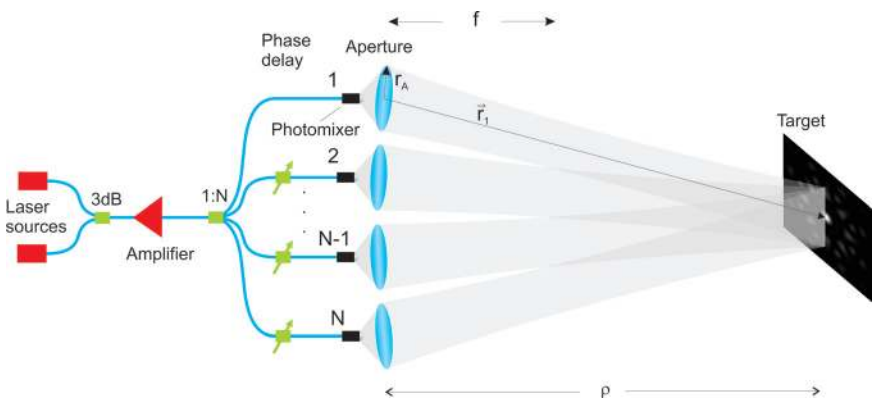

FIG. 33. (Color online) Schematic setup for coherent superpositioning of THz beams in the far field. Reprinted with permission from S. Preu, S. Malzer, G. H. Döhler, and L. J.Wang, Proc. SPIE 7117, 28 (2008). Copyright © 2008, SPIE.

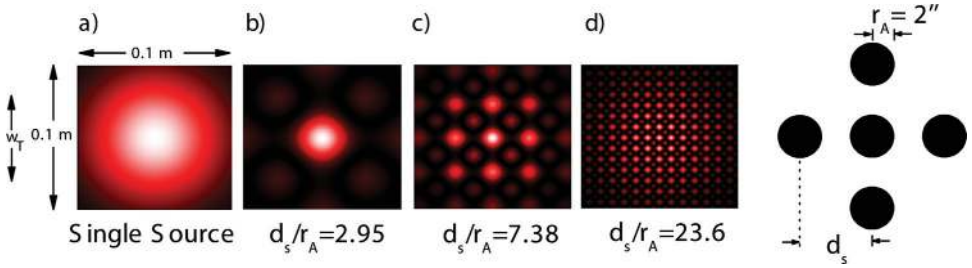

FIG. 34. (Color online) Calculated examples for interference patterns at 1 THz (ρ =30 m) with 5 sources using different source spacings, d_s. The beam waist, w_T, of an individual beam in the target plane is indicated in (a). Reprinted with permission from S. Preu, S. Malzer, G. H. Döhler, and L. J.Wang, Proc. SPIE 7117, 28 (2008). Copyright © 2008, SPIE.

Diffraction effects slightly alter the optimum focal length and maximum focusing distance.[145] Some examples of interference patterns, neglecting diffraction effects, are shown in Fig. 34.

In general, the intensity of N sources at the zeroth order of constructive interference is $N^2 I_0$ [see Eq. (118)], as for chip-sized arrays. For a low number of sources and $\rho \gg f_{\max}$, some simple design criteria can be determined by approximating the Gaussian beam phase fronts by plane waves. The optical axes of two neighboring sources are inclined by α. The THz beams cross at $x = 0$ in the target plane. The first minimum occurs at $x_{\min,1}$ where the relative phases of the two sources differ by π. In general, the n^{th} minimum appears where $\vec{k} \circ \vec{x}_{\min,n} = \sin\alpha \cdot (2\pi/\lambda) \cdot x_{\min,n} = (2n\ -1) \cdot \pi$. The value $x_{\min,1} = \lambda/(2 \cdot \sin\alpha)$ determines the width of the central peak (please refer to Fig. 35). A narrow peak will be created for large α. If the beam waist of the single source is much larger than $x_{\min,1}$, the next orders of constructive interference ($n > 1$) will also contain a similar amount of power. This results in an array of very similarly intense peaks [Fig. 34(d)]. For a given distance, ρ, the angle $\alpha = \arctan(\rho/d_S)$ is determined by the source spacing. The value of d_S determines whether a high power central peak [small d_S, Fig. 34(b)] or an array of similarly strong THz pixels is created [large d_S, Fig. 35(d)]. An experimental verification is shown in Fig. 35. A Golay cell with a 6 mm aperture was used to scan the interference pattern of two beams that are inclined by $\alpha = 10.5°$. Due to the finite width of the Golay cell, the pattern does not reach the nodes. A theoretical calculation based on the beam profiles of the individual sources, using the above assumptions and taking the finite width of the Golay cell into account, closely matches the experimental data with the relative phase between the two laser beams as the only fitting parameter.

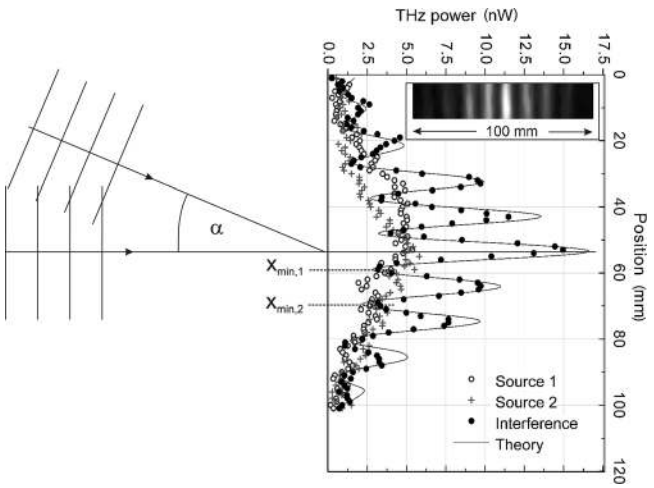

FIG. 35. Interference of two (plane-wave) beams for an inclination angle of 10.5° at 0.15 THz. Powers of the individual sources are depicted in crosses and circles. The theoretical graph includes the finite width of the Golay cell window of 6 mm.

For high spatial resolution, however, a single narrow peak with high intensity is best suited for many imaging applications. This can be achieved by using many sources to form a synthetic aperture[145] as depicted in Fig. 36. For the depicted 4×1 setup [Fig. 36, inset (a)], the central peak contains about 63% of the total power at 0.23 THz. Due to the linear configuration, the direction perpendicular to the array axis is almost unaffected, resulting in the oval spot shown in Fig. 36, inset (b). The intensity of the central spot increased by (almost) $4^2 = 16$ due to constructive interference. The array of photomixers overcomes the single source power limit, while strongly increasing the center peak intensity (up to a factor N^2) and reducing the peak width at the same time. The interference patterns can be adapted to the desired working scheme by the setup and phase relations in the array. By aligning the polarizations of the emitters in a radial geometry, i.e., pointing outwards, even radially polarized THz beams should be possible using a circular array. Such doughnut modes may enable subdiffraction limited spot sizes[124,125] and may aid in further improving the spatial resolution.

2. Application to very long baseline interferometry

Another very interesting field of THz research is astronomical THz background spectroscopy. A ground-based

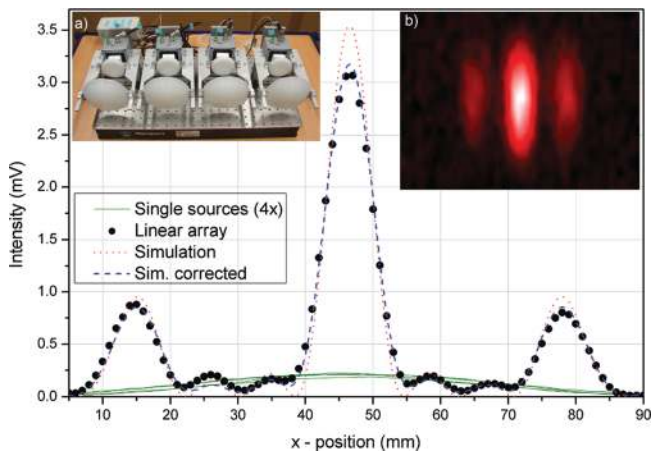

FIG. 36. (Color online) Cut through the interference pattern of a linear 4×1 array [inset (a)] along the array axis at a target distance of $\rho = 4.2$ m and $\nu_{THz} = 0.23$ THz. The dashed line shows the theoretical expectation corrected for the finite width of the Golay cell aperture. Inset (b): Interference pattern of the array at 0.8 THz. Reprinted with permission from S. Bauerschmidt, S. Preu, S. Malzer, G. H. Döhler, H. Lu, A. C. Gossard, and L. J. Wang, Proc. SPIE **7671**, 76710D (2010). Copyright © 2010, SPIE.

facility, the Atacama Large Millimeter Array (ALMA) is being built in the Atacama desert in Chile at an elevation of 5000 m.[16,21] The giant array with a baseline of tens of kilometers, will consist of up to 66 antennas with 12 m diameter. Its purpose is astrophysical spectroscopy, e.g., for studying radiation from protostars and star-forming regions, THz imaging of galaxies, and determination of the temperature, density, and excitation state of gases in stellar clouds. It will be operated as a phased array detector (i.e., the inverse scheme of a sender array as presented in the previous section) in the frequency range of 30–950 GHz. The synthetic aperture provides an equivalent single aperture diameter of about 15 km.[16,21] The THz signal will be detected by mixing the received THz signal with a local oscillator signal in a superconductor-insulator-superconductor (SIS) junction down to below 12 GHz. The resulting RF signal will be further down converted and electronically transferred to a data evaluation center. For a phased array receiver operation, the antennas have to be phase correlated. The distribution of THz radiation in the antenna network is typically hindered by high losses of bulky THz waveguides. A local oscillator (LO) signal for down conversion has to be provided on-site. These phase-correlated local oscillators may be CW photomixers, as first proposed by Payne and Shillue[146] and followed up by several groups.[139,148] The photomixers are driven by a common pair of 1550 nm laser beams, fiber-distributed within the antenna array. Distributed EDFAs can be implemented to provide sufficient power. For stabilized lasers with coherence lengths in the tens of km range and adequate stabilization of the fiber length variations attributed to thermal and seismic fluctuations,[147,149,150] all antennas are mutually coherent, similar to the small scale arrays presented in the last section. Fig. 37 depicts a schematic setup. In fact, the ALMA frequency range matches the frequency range where photomixers operate most efficiently. Except for the highest frequency bands of ALMA (>0.7 THz), the results of Ito and coworkers[54,90] show that photomixers indeed provide enough local oscillator power

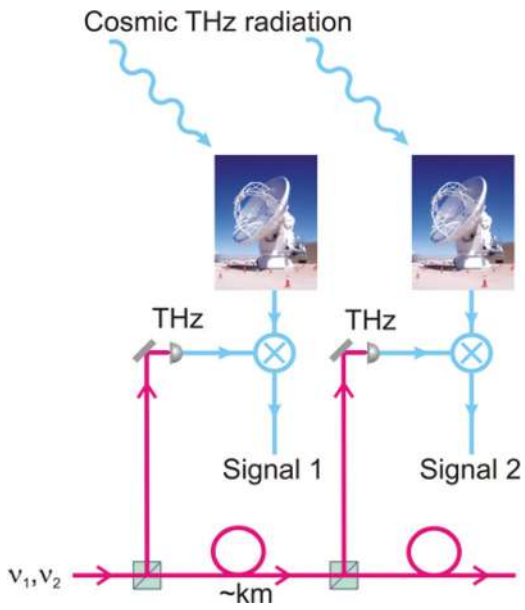

FIG. 37. (Color online) A schematic setup for phase coherent operation of the antenna receivers at ALMA. Antennas reprinted permission from the Atacama large millimeter submillimeter array website, http://almaobservatory.org/.

according to the ALMA project book,[151] e.g., 20 mW around 100 GHz.

The very long baseline of 14–16 km implies laser linewidths well below 5 kHz to achieve mutual coherence between the LOs. Such narrow linewidths at single frequency operation are only achievable with highly stabilized CW lasers. Using the frequency comb stabilization technique, linewidths close to or even below 1 Hz[140,152] of a single stabilized CW laser were already demonstrated. Hereby, a narrow linewidth laser (at or below 1 MHz is typically sufficient) is mixed with a peak of a highly stabilized frequency comb that is locked to a sub-Hertz level (atomic) clock or a hydrogen maser (typical frequency stabilities $\Delta v/v = 10^{-13}$ at 1 s integration time). The implementation of a phase lock loop allows for transferring the extreme stability of the atomic clock to the optical signal. Musha and coworkers[139,147] performed a photomixing experiment with UTC photomixers by stabilizing two 1550 nm external cavity lasers via a single 1550 nm frequency comb to a Rb clock. By stabilizing the signal to different comb lines, up to 100 GHz photomixing signals were generated. The maximum frequency was only limited by the phase noise detection scheme, not by the photomixer. Excellent carrier to noise characteristics, fulfilling the ALMA requirements on spectral purity and stability were achieved.

Thermal and seismic noise cause severe fiber length fluctuations for such large displacements of the antennas, which have to be compensated. In the optical domain, successful stabilization experiments were carried out by Daussy *et al.*[150] A laser signal was transferred via public optical fibers over a distance of 43 km using fiber length fluctuation compensation. Again, only slight linewidth broadening and excellent stability with an Allan deviation in the range of $10^{-14} - 10^{-15}$ could be reported.

ALMA yet incorporates a photomixer (photodetector) operated around 100 GHz[149,153,154] A subsequent RF amplifier and a Schottky varactor chain[155] may be used to double and triple the frequency to the desired band and to provide sufficient LO power.In principle, however, a purely photonic photomixer approach should yet also be possible.[146] A single wideband photomixer can cover most of the frequency bands of the ALMA project. The power levels of UTC diodes have already met the requirements in the ALMA project book,[151] except for the highest frequency bands. A small-scale demonstration of real time synthetic aperture imaging around 100 GHz is given in Refs. 156 and 174. Four packaged LT-GaAs photomixers were used to image a moving (strong) THz source. Precise knowledge of the baseline lengths allowed for a reconstruction of the source position and its trajectory.

C. Continuous-wave THz spectroscopy

1. Gaseous phase spectroscopy

As already demonstrated for the ALMA array, photomixers are an interesting tool for astronomical spectroscopy. The spectra of extraterrestrial gases, e.g., of stellar dust, are superposed with the cosmic background blackbody radiation. Blackbody radiation is described by Planck's law[157]:

$$L(v,T) = \frac{8\pi h v^3}{c^3} \cdot \frac{1}{\exp(hv/kT) - 1}. \qquad (124)$$

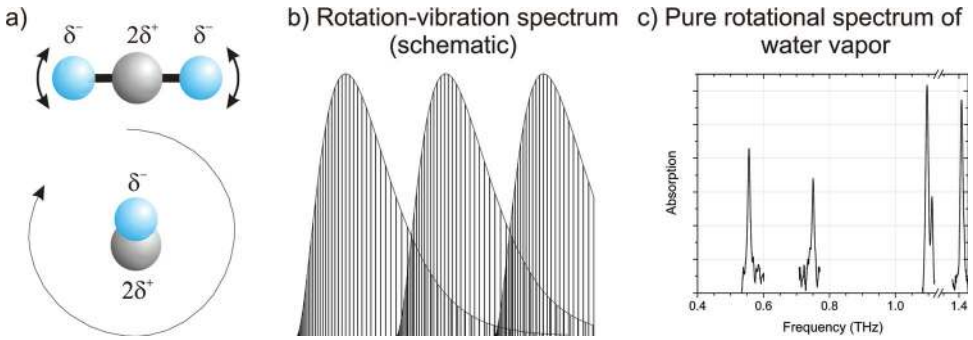

FIG. 38. (Color online) (a) Top: Vibration of a CO_2 molecule, creating a dipole moment. Bottom: The rotation of the excited CO_2* provides an oscillating dipole moment. (b) Schematic of a rotation-vibration spectrum as it occurs e.g. for CO_2 or similar molecules with available energy levels at $E = E_{vib} + E_{rot}$. (c) Some measured pure rotational spectral lines of the polar molecule water (vapor in air) in the THz range.

The spectral density of cosmic background radiation (T = 2.7525 K) or radiation from stellar dust (up to T = 30 K) peaks at 0.282 THz and 3.1 THz, respectively, right in the THz frequency range. Terahertz radiation can also penetrate through stellar dust, in contrast to visible and infrared light. Stellar THz spectroscopy can give insight into the physics of star forming regions. As described in the last section, photomixers are already used as local oscillators for down conversion of the extraterrestrial signal[155] at ALMA, offering high spectral purity and a huge tuning range with a single, compact sender at room temperature. These features allow for building powerful spectrometers with a huge frequency span. The distinct, strong resonances of many molecules in the THz frequency region allow THz spectroscopy for resolving the composition and excitation state of stellar gases and clouds, but also for spectroscopy of polar molecules. The interaction mechanism will be explained in the following.

Electromagnetic waves interact with matter via dipole moments. In the (soft) UV, visible, and near-IR ranges, such dipole moments are usually excited electronic states of the atom or molecule. In the mid-IR, photon energies are too small to excite electronic transitions, but can excite vibrations of a molecule. For low order vibrations the binding potential of the molecule is approximated by a harmonic potential. The energy necessary to excite a (1D) vibration with quantum number n is

$$E_{\mathrm{vib}} = h\nu(n + 1/2) \quad \text{where } \nu = \frac{1}{2\pi}\sqrt{\frac{\kappa}{\mu}}. \tag{125}$$

κ is the curvature of the harmonic potential and μ is the reduced mass. Even nonpolar molecules, e.g., CO_2, can interact with light by creation of a dipole moment and via a transition into an excited state (see Fig. 38). A very common implementation of such a process is the CO_2 laser operating at 30 THz.

The vibrational modes of the molecule are superposed with rotational modes of much less energy where the excited dipole, CO_2^*, rotates along one of its major axes, perpendicular to the dipole moment. THz photons carry too little energy to excite vibronic interactions, except for phononic interactions of the Reststrahlen band of solids or librations of macromolecules.[158] However, many molecules already exhibit a permanent dipole moment in the ground state due to their chemical structure, for instance water. Similar to rotating CO_2^*, photons can excite rotations of these polar molecules with an energy of

$$E_{rot} = \hbar^2/(2\Theta) \cdot J(J + 1), \tag{126}$$

where Θ is the moment of inertia of the molecule and J the rotational quantum number. Typically, $\hbar^2/(2\Theta)$ is in the range of 0.1–10 meV (25 GHz–2.5 THz),[157] i.e., the rotational spectra appear in the microwave and THz frequency range. Therefore, polar molecules exhibit strong, feature-rich THz spectra, allowing for identifying individual gaseous components down to the ppm range.[14] Noteworthy, the Doppler broadening increases the linewidth much less in the THz range than in the optical domain, as

$$\Delta\nu_D = \nu\sqrt{\frac{k_B T}{mc^2}} \propto \nu. \tag{127}$$

The much smaller THz frequencies, ν, compared to the optical domain ($\nu_{\mathrm{opt}} \approx 1000\,\nu_{THz}$) reduce the effect of Doppler broadening to around 1 MHz or less, even at room temperature. In contrast, Doppler-broadened linewidths of optical transitions are in the GHz range. At low pressure, as is the case for stellar THz spectroscopy, these narrow lines allow for accurate THz fingerprinting. At standard pressure, however, the linewidths are broadened due to collision processes with any component of the investigated gas mixture:

$$\Delta\nu_P = p \cdot \sigma\sqrt{\frac{8}{\pi\mu k_B T}}, \tag{128}$$

where μ is the reduced mass of the participating scattering partners, $\sigma \approx \pi(r + R)^2$ is the scattering cross section of the scattered partners with classical radius r and R, and p is the pressure. At room temperature and standard pressure, the pressure broadening is in the range of 1–10 GHz for small molecules.

The rotation energy for a given rotation state in Eq. (126) is inversely proportional to the reduced mass of the molecule, μ, as $\Theta \propto \mu$. The THz spectra are thus very sensitive to the isotopic composition. This has been verified for water and heavy water[159] and isotopomers of CO.[160] Also slight changes of the chemical structure, e.g., replacement of a functional group, cause strong differences in the THz spectra.[11]

To date, many THz spectroscopic results were achieved with pulsed systems, mostly implementing LT-GaAs photomixers (THz-TDS). One reason for the choice of pulsed operation is the ease of detection of signals with extremely low intensity using electro-optic sampling or a zero-biased LT-GaAs

switch. To date, various kinds of detectors are also available for CW-based systems. Cryogenic transition edge detectors[161] for very high resolution and fast data acquisition, hot electron bolometers, Golay cells, or much cheaper (but slow) commercial pyroelectric detectors (with nW resolution) are available. THz detection by electro-optic sampling could also be demonstrated for CW signals.[162] In addition fast, small Schottky-diode detectors with high responsivity are available.[163] CW THz detection with photoconductors[4,164] is feasible as well. Plasmon-resonant detectors have recently gained much attention. The first room temperature operating plasmon-based field effect transistors have been demonstrated.[165–167] The latter four detection schemes operate at room temperature and can easily be miniaturized. They allow for extremely high chopping frequencies (up to more than 1 MHz) and, hence, short lock-in time constants and high measurement speed, enabling short data acquisition times.

A second reason for the choice of pulsed systems is the lack of commercially available, tunable, and powerful CW sources in the past decade. Currently, however, several vendors offer CW systems or are about to commercialize such systems. CW photomixers are excellent tools for spectroscopic applications. Due to single frequency operation, they offer much higher spectral densities which translate into an improved signal-to-noise ratio. By using narrow linewidth driving lasers, they can offer very narrow THz linewidths (i.e., Hertz level when adequate laser stabilization is maintained[138,147,168]) and provide excellent resolution for narrow molecular resonances, in contrast to Fourier-limited optical rectification. The resolution and measurement speed is solely limited by the linewidth and tuning speed of the photomixed lasers and the detector speed. CW systems can potentially be much faster than THz-TDS systems that are resolution limited by the scanning speed and delay step width. This is particularly the case for applications where just a single (or a few) narrow, but well-resolved frequency window(s) are required rather than a large spectral range. CW photomixers can be operated with laser diode pairs, if necessary with a subsequent semiconductor or fiber amplifier. Very compact photomixers[76,90] (see also Fig. 19) and inexpensive optics and lasers are available. Most pulsed THz systems, however, still depend on powerful, but more or less bulky and expensive Ti:sapphire laser systems. CW photomixing systems are more compact, cheaper, and potentially more accurate than pulsed systems. Photomixing systems also outperform other CW systems, such as backward-wave oscillators or Gunn-diodes, with respect to tunability. A single photomixer can cover several octaves. Several groups have demonstrated CW spectroscopy systems with a dynamic range of 10^6 or more,[4,74] suitable for most spectroscopic experiments. UTC photodiodes have already shown an output of several μW at 1 THz[90] and much more at lower frequencies,[103,169] permitting a dynamic range on the order of 10^6 even if a Golay cell detector is used. Similar values can be found for CW LT-GaAs systems.[4] To give a few examples, CW photomixing systems have been used to resolve the rotational eigenstates of several gases such as water or SO_2.[8] Small biomolecules, like biotin,[170] were characterized. A very good example for extremely high-resolution CW THz spectroscopy with LT-GaAs photomixers is given by Chen *et al.*[171] Five resonances of acetonitrile were resolved at a pressure of 150 mTorr in a frequency window of only 96.1 MHz at 312.5 GHz. A relatively simple stabilization system for the lasers was implemented. The short term linewidth of the system was only 50 kHz, the long term drift resulted in 2 MHz/10 s stability. The data set for acetonitrile was further extended by Matsuura and coworkers[160] with a similar system based on CW LT-GaAs photoconductors, operating around 1.337 THz. In addition, they finely resolved the resonance shift of isotopomers of carbon monoxide (CO) around 1.45 THz. CW photomixing systems have also been used to study macrosystems, e.g. *Bacillus subtilis*,[19] a close relative to Anthrax. As a result of the large amount of constituents, the spectra do not show such clear resonances as molecules. However, there are several clear signatures that could be used for identification. Similar results on several small biomolecules are found by Plusquellic and coworkers.[10] Future security-related THz scanners could be operated with CW photomixing systems as proposed in refs.[172,174] When looking for molecular resonances, only those narrow frequency windows are scanned where spectral features of the species of interest appear. Other parts of the spectrum can be omitted to increase the measurement speed.

2. THz whispering gallery mode resonators

Spectroscopy of artificial, photonic atoms and molecules, namely THz whispering gallery mode (WGM) resonators, can give insight into these novel photonic systems. WGM resonators consist mostly of a disklike, droplike, or stadium-shaped piece of dielectric material. Light can be stored inside the dielectric material by total internal reflection at the boundary of the resonator. From a classic point of view, the light of round trip m in the resonator interferes with the other $m-1$ round trips, resulting in an angular boundary condition. A discrete mode structure evolves, providing high Q resonances, similar to a Fabry–Perot cavity. A more accurate description is given in Refs. 175–177, by solving the Helmholtz equation at the boundary of the resonator. Such resonators can drastically enhance the THz electric field, attributed to their potentially high-quality (Q) factors. They can also be used as small-sized filtering elements, as will be shown below.

The long wavelength makes THz optical elements bulky and difficult to integrate. The blazed grating shown in Sec. III A, Fig. 28, only had 29 ridges but is 6.1 cm in size. The maximum wavelength resolution of such a device is limited to $\Delta\lambda = \lambda/N = \lambda/29$ for the first order. To achieve better resolution, compact WGM resonators can be used. For simplicity, we only focus on cylindrical disks (or toroids) here. The Helmholtz equation is separable into radial and angular components. Only a 2D equation set needs to be solved in the disk plane. Both components provide discrete solutions. Any mode can be denoted by $TE_{j,m}$ or $TM_{j,m}$, where j is the radial and m the angular quantum number. The (small) extension of the disk in the vertical direction causes a shift of the resonances and can be taken into account by an effective index of refraction. Note that in contrast to total internal reflection on

a straight interface, the curvature of the resonator allows for a small leakage, limiting the maximum Q factor, even for loss-free materials. This loss is taken into the theoretical model by solving the equation set with a complex wave number $k \in \mathcal{C}$. In general, the losses are (exponentially) higher for lower order modes. The ideal Q factor is $Q_{id} = -2\mathrm{Re}[k]/\mathrm{Im}[k]$. In addition, material specific losses and surface roughness reduce the Q factor. The real Q factor is $Q = (1/Q_{abs} + 1/Q_{id})^{-1}$, where Q_{abs} is the absorption and roughness limited quality factor. In the optical domain, Q factors higher than 10^{10} have been demonstrated.[178] The record Q factors are still continually shifted to higher values by further smoothing the surface and reducing material losses. Note that the resonators only need to be a few wavelengths in diameter, and can thus be very compact, even in the THz frequency range. Due to the large tuning range and narrow linewidth, CW photomixers are an ideal tool to characterize THz WG-resonators over many WG-free spectral ranges. As the cavities are purely optical, the linewidths are solely broadened by acoustic vibrations and opto-mechanical cross talk (heating). The latter only occurs at very high power levels and with much less impact as Doppler and pressure broadening in the case of real atoms and molecules. We summarize some results from polyethylene (PE) plastic and quartz resonators with diameters ranging from 3 mm to 5.2 mm to provide an overview of the potential of WGM resonators. Q factors of up to 700 at frequencies between 100 and 330 GHz were measured for these resonators. These values demand a resolution of better than $\Delta\nu < \nu/Q$, i.e., a resolution in the 200 MHz scale is required. Figure 39 shows measured Q factors for different resonator types: The quality factors are deduced from the measurements by $Q_{meas} = \nu_{res}/w_{res}$, with w_{res} the FWHM of the Lorentz-shaped resonance and ν_{res} the resonance frequency. The chosen materials have relatively low loss: PE plastic offers an absorption-limited Q factor Q_{max} around 3000 and quartz provides $Q_{max} > 20000$ but with some birefringence. For nonabsorption-limited resonances or Q much below Q_{max}, numerical calculations predict a roughly exponential increase of the quality factor with increasing frequency or increasing m, for the radial mode number $j = \text{const}$. The measured Q factors for circular resonators in Fig. 39 show such a behavior. Only the highest Q values show some saturation, also attributed to the frequency stability limited resolution of the setup. By increasing the radius of the resonator less light leaks out. The confinement of a mode, and, consequently, the Q factor, increases. For this reason, the Q factors of curve (b) in Fig. 39 are much higher than that of curve (a) for the same wavelength. Q also increases for resonators with the same geometry but with higher indices of refraction due to stronger confinement. For this reason, the much smaller quartz resonators of curve (c) provide similar Q factors to the PE resonators of curve (b).

Common ways to couple light into a WGM resonator are evanescent coupling of a thin (tapered) dielectric waveguide[179,180] to the evanescent field of the cavity or phase-matched, frustrated total internal reflection at a prism.[181] For the measurements shown in Fig. 39, thin, rectangular Teflon waveguides with dimensions around 1×1.5 mm^2 and 1×2 mm^2 were used.

Shape-related theories concerning WGM resonators can be easily tested in the THz frequency range. As a result of the scale invariance of electromagnetism, most of the concepts followed up in the optical domain can be transferred to the THz domain and vice versa. Due to much longer wavelengths, it is often much easier to test WGM-related theories in the THz domain. The larger size facilitates the production of resonator features in many cases. As an example, Annino and coworkers[180] could directly measure the radial field distribution of the evanescent field of a cavity. A sharpened dielectric rod, acting as antenna, was scanned along the resonator surface. Whenever the rod tip coincided with the position of a WG mode, some power was coupled into the rod. Scanning across the resonator surface showed the exact mode structure and mode distribution of the resonator.

For many applications such as lasers with WGM cavities, knowledge of the exact mode distribution is important, for instance to match the mode position with that of the amplifying medium. Of further importance is efficient outcoupling of the laser mode. In the following, we want to show directional emission from a WGM resonator with a finite scatterer. A spherically symmetric WGM resonator does not show directional emission due to its symmetry. For

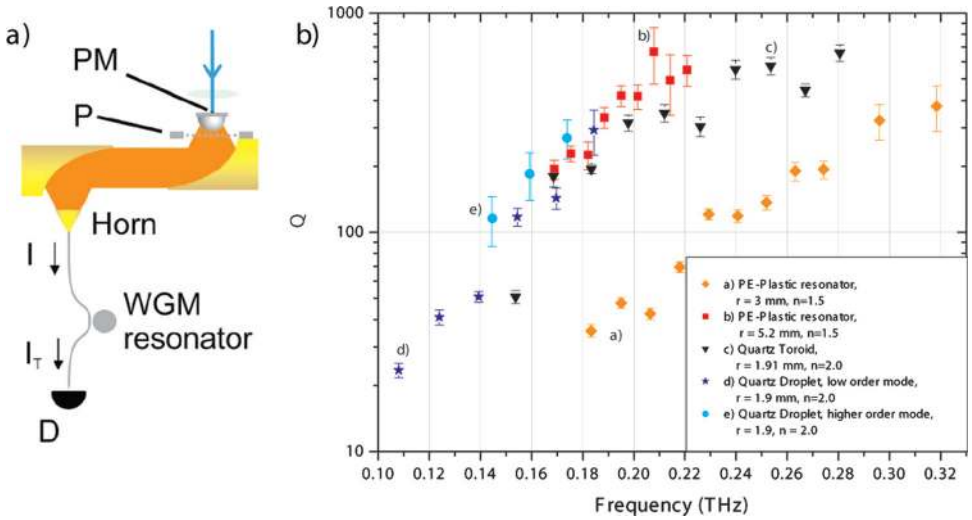

FIG. 39. (Color online) (a) Setup with a bent waveguide for enhanced coupling. (b) Single logarithmic plot of the Q factors of different resonator types.

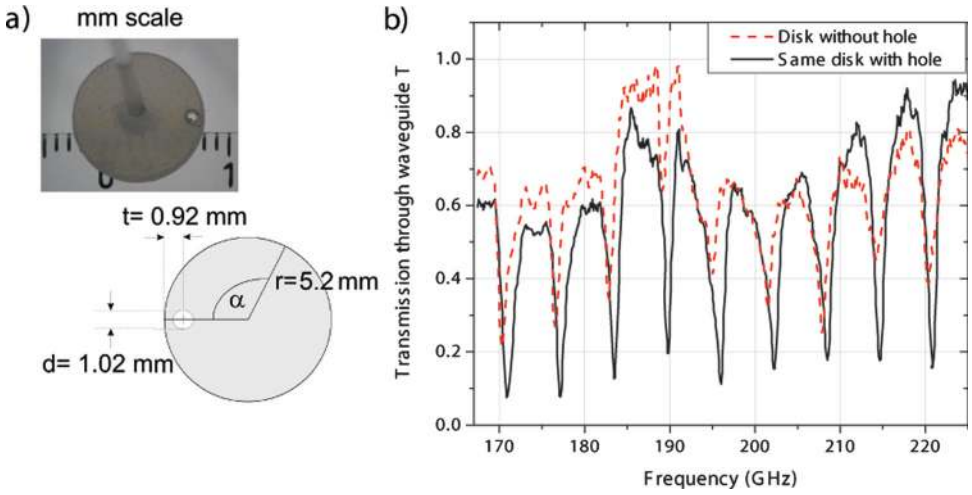

FIG. 40. (Color online) (a) Disk with hole and its dimensions. (b) Spectrum of the disk with and without hole.

several applications such as outcoupling of a microdisk laser mode, directional emission is highly desired. Asymmetric and chaotic resonators have been designed.[182] Other concepts implement stadium-shaped resonators[183] that outcouple at the position of highest curvature. Putting a scatterer, e.g., a hole, close to the boundary of the disk will also allow for outcoupling. If the position of the hole is carefully chosen, the WG modes are only slightly disturbed, causing a slight frequency shift and a moderate reduction of the quality factor.[184,185] In the following, PE plastic disk resonators with a radius $r = 5.2$ mm and a thickness of 1.1 mm are used. They are coupled to a rectangular Teflon THz waveguide. The resonance spectra are recorded before and after a hole is drilled at $0.82 \cdot r$ by measuring the transmitted signal through the waveguide, as shown in Fig. 40. The Q factors are only marginally altered and the peaks are slightly blue shifted for this configuration. The coupling to the waveguide is even improved for the waveguide and resonator in contact. In addition, angular emission is scanned (Fig. 41) using cylindrical Teflon lenses to improve the collection efficiency. The lenses collected the THz power within a 15° aperture angle. The emission oscillates with respect to the emission angle around the (also slightly oscillatory) value for a disk without hole (see Fig. 41). The strongest peak contains about 4% of the power fed into the disk. The waveguide, however, disturbs the WG modes and, consequently, the emission pattern.

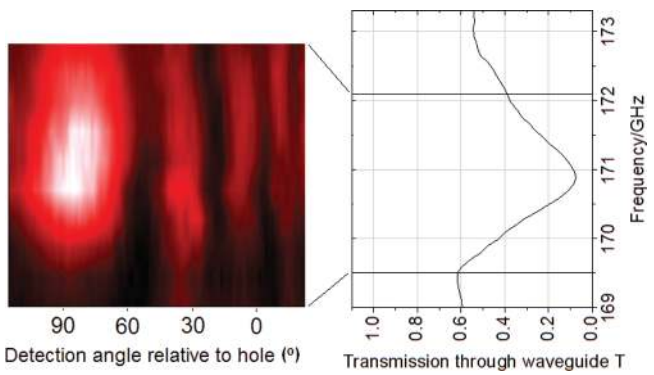

FIG. 41. (Color online) Angular scan of the outcoupled light around a resonance at 0.17 THz. The frequency scan of the disk is shown to the right.

The enhanced emission is consistent with theoretical predictions, however, the angular spectrum differs. This is partly attributed to waveguide feeding, which already perturbs the symmetry of the system and causes some directional emission even for a disk without a hole. Further measurements and careful comparison to the theory are underway.

More fundamental physical aspects of WGM resonators can be tested and examined in the THz frequency range. The (nontrivial) modes of symmetric WGM resonators exhibit an orbitlike structure, very similar to that of electrons in atoms. In fact, there are more analogies to an atom. If the evanescent field of the cavity is disturbed by a second cavity close by, the cavities interact. Modes that are common for both cavities split up into a low frequency and a high frequency mode (see Fig. 42). The system becomes nonresonant at the original resonance frequency. This is very similar to the formation of a bonding and an antibonding electron mode of two approaching atoms. The bonding mode is the symmetrical combination of the two atoms' wave functions. The electron probability between the atoms is enhanced. In the same way, the electric field strength is increased for the lower-frequency mode of the coupled resonators whereas the field of the antibonding (antisymmetric) high-frequency mode provides a node in between the disks. There is an analogy between resonance frequencies and molecular energy levels as well as between electron wave function and electric field strength, as illustrated in Fig. 42. A recent theoretical publication[186] also showed that there is a force between the two WGM resonators. It is attractive for the symmetric (low-frequency) and repulsive for the antisymmetric (high-frequency) mode, similar to the case of molecules. However, the force is very tiny and the distance between the resonators needs to be in the range of the wavelength, such that static charging and Van der Waals forces make measurements in the optical domain very challenging. Using (sub)mm wavelengths circumvents these problems and could help to verify the theoretical prediction if sufficient power and resonators with high Q factors are available.

For showing mode splitting, the possibility of a large disk size in the THz frequency range again facilitates the experiment. In the optical domain, engineered thermally tuned resonators,[187] sophisticated tools such as ion beam

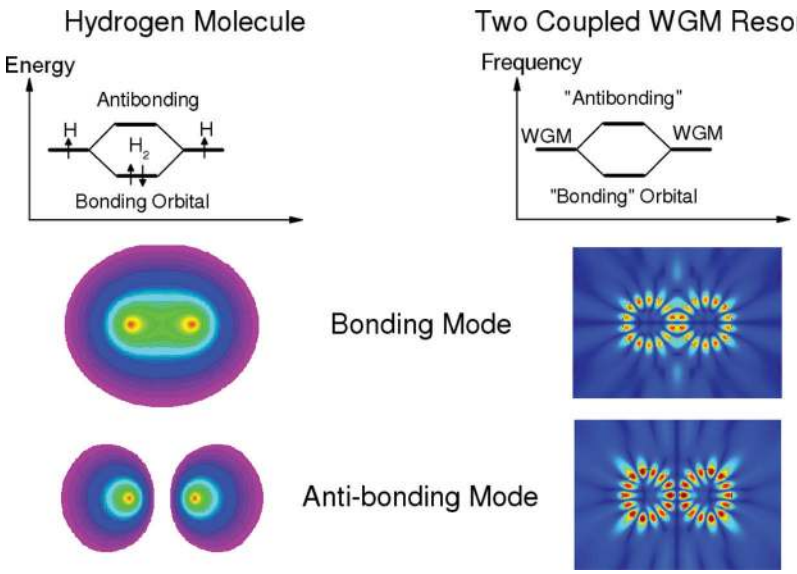

FIG. 42. (Color online) Analogy between the electronic states in a H_2 molecule and the photonic modes in a dielectric whispering gallery mode resonator. Bottom left: electron probability in the H_2 molecule for the first symmetric and antisymmetric state. Bottom right: Electric field strength of coupled WGM resonators for the single resonator mode (n,l)=(1,7). Note that the color scales and mode numbers are different.

etching and electron beam lithography,[188] or the production of many similar resonators[189] was necessary to produce resonators with coinciding modes. THz resonators can just be milled to an appropriate size and then fine-tuned with emery paper or the like. This way, PE plastic disks and quartz disks with agreeing mode spectra were produced.[131] Figure 43 shows the individual spectra of two mode matched quartz resonators and the spectrum of the coupled resonators. The setup was very similar to that of the investigation of resonators with induced scatterers (see Fig. 39). The modes were matched to within the measurement accuracy of the nonfrequency-stabilized setup as can be seen in the inset. Clear mode splitting/electromagnetically induced transparency is found. The experimental spectra agree well with a numerical calculation. Similar to approaching atoms, the strength of the mode splitting depends on the distance of the resonators.[131] Again, very good agreement to the theory was found with a frequency difference of the split peaks up to 2.5 GHz. The theory holds true for any wavelength range as a result of the scalability of electromagnetism and, thus, the results are transferable to the optical domain and vice versa.

The capability of designing a resonance at a deliberate frequency allows for construction of small-sized (just a few wavelengths in scale), interference-based filters (bandpass/band stops), a potential application of coupled resonators.[190,191] THz WGM resonators could also stimulate the research for low-loss THz materials, as material specific losses limit the maximum Q factor of a resonator. For more general WGM applications we refer the reader to the work of Ilchenko and Matsko.[192]

In the optical domain, WGM resonators are used for evanescent sensing.[193] Even small absorption within the range of the evanescent field of the cavity has a strong impact on the quality factor and also shifts the resonance frequency. Sensitivities in the range of or below nanomoles could be demonstrated.[193] WGM resonators could also be used as very sensitive evanescent field sensors in the THz range. A demonstration of such a THz sensor is given the work of Annino *et al.*,[194] using the example of electron magnetic spectroscopy. 1,1-diphenyl-2-picrylhydrazyl (DPPH) was dissolved in a wax droplet that is attached to the outer rim of a WGM resonator, and spectra were recorded.

Whispering gallery mode resonators have been proposed as efficient $\chi^{(2)}$ difference frequency mixing sources for CW

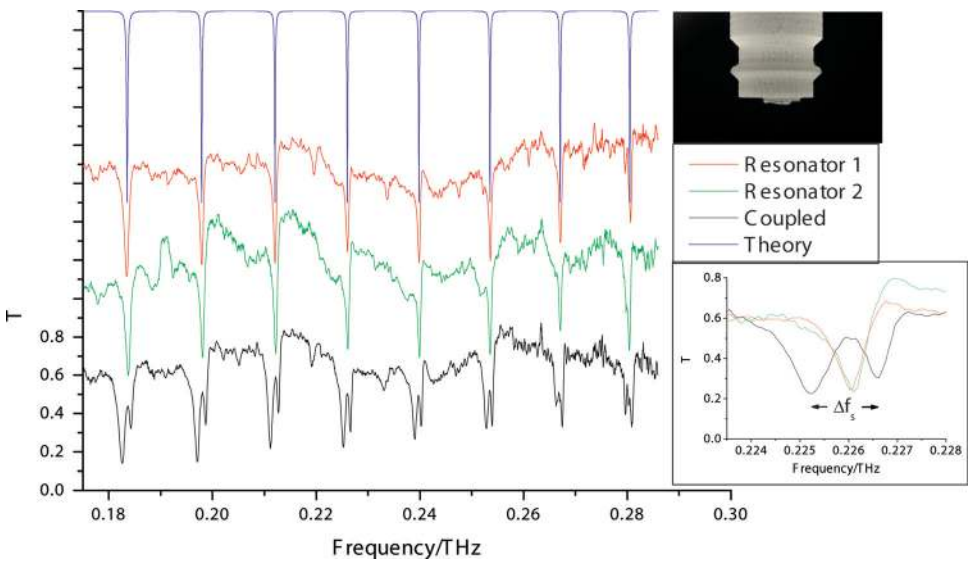

FIG. 43. (Color online) Spectra of single and coupled, matched quartz WGM resonators. Reprinted with permission from S. Preu, H. G. L. Schwefel, G. H. Döhler, L. J. Wang, M. Hanson, J. D. Zimmerman, and A. C. Gossard, Opt. Express **16**, 7336 (2008). © 2008, Optical Society of America.

THz radiation.[195] By proper choice of the disk dimensions, a whispering gallery mode resonator made of a material with a large $\chi^{(2)}$ coefficient and small THz absorption can be co-resonant for two optical frequencies and their respective THz difference frequency. For a disk with thickness much larger than the optical wavelength but smaller than the THz wavelength, $\lambda_{THz} > d \gg \lambda_{opt}$, the optical fields will be well confined in the z-direction perpendicular to the disk plane. The effective optical index of refraction is close to the refraction index n_{opt} of the material. The THz wave, however, will have a very large evanescent field along the z-direction, resulting in a thickness-dependent effective index of refraction that is much smaller than the bulk THz refraction index, n_{THz}. For materials with $n_{opt} < n_{THz}$, phase matching of the optical and THz waves can be achieved by choosing an appropriate thickness, d, of the resonator. Many $\chi^{(2)}$ active materials show $n_{opt} < n_{THz}$, for instance $LiNbO_3$: $n_{opt}^{\mathrm{ord}} = 2.2 - 2.4$, $n_{opt}^{eo} = 2.1 - 2.3$, and $n_{THz}^{\mathrm{ord}} \approx 6.7 - 7.1$, $n_{THz}^{eo} \approx 5.15 - 5.4$.[196,197] Triply resonant WGM resonators with high Q factors provide extremely high electric fields within the resonator, even for CW signals. Provided that there is sufficient spatial overlap of the optical and THz modes, efficient down conversion of the optical beat signal[195] to a THz signal or up conversion of a THz wave on an optical carrier may be achieved.[198]

D. Wireless LAN utilizing THz photomixers

Since the development of digitized data transfer, the required data rate has been growing exponentially: manual Morse codes (a few baud, since 1833), early telephone modems (up to about 200 baud, 1950s), ISDN (8 kbaud for a single channel, 1980), to the up-to date Gbit ethernet (GbE) network links [e.g., 125 Mbaud/wire pair (1000Base-T)]. This trend is not expected to end, since there is growing interest in private telecommunication for transferring huge amounts of data such as music, games, and movies. Furthermore, the networks and Internet representations are continually growing. Higher data transfer rates require higher data throughput in links and channels. The data capacity of a given transfer technology, however, is limited. For binary systems (as used by computers), the theoretical maximum data transfer rate, C, is given by the Shannon–Hartley law

$$C = B \cdot \log_2(1 + \mathrm{SNR}), \tag{129}$$

where B is the bandwidth of the system, e.g., $B \geq 62.5$ MHz (1000Base-T) for the 1 GbE, and SNR is the signal-to-noise ratio. Increasing data rates at a given bandwidth require an exponentially improved SNR. This soon reaches practical limits such as excess noise caused by electrical stray fields along the transmission line (in the case of RF technologies) or absorption, dispersion, and thermal index variations of fiber-based optical transmission lines.

A more promising approach for improving the data transfer rate is an increase of the bandwidth, as a result of linear dependence. Alternatively, new channels in yet unused frequency bands could be implemented. An increase of the maximum carrier frequency up to THz frequencies can both provide access to new frequency bands and larger bandwidth (which is, of course, a fraction of the carrier frequency). To the knowledge of the authors, the highest carrier frequency used in a public network has almost reached the THz frequency range, implementing 80 GHz[199] connections between Trump buildings in New York. The international telecom union (ITU) already regulates frequencies up to 400 GHz.

For far distance high data rate communication, optical 1550 nm continuous-wave systems are currently used. Electronic methods would simply catch too much noise over large distances. The maximum bandwidth of a fiber system is currently only limited by the data modulation technology, fiber loss, and dispersion. For the last few 100 meters, the optical signal is converted into an electrical one, yet using RF photodiodes in the GHz range. The next generation of high speed data transmitters will have to penetrate into the THz frequency range. Standard photodiodes are then too slow. Their 3 dB bandwidth [which is the maximum bandwidth, B, in Eq. (129)] is limited by their transit and RC time constants, similar to photomixers. Thus, high speed, continuous-wave THz photomixers may replace RF photodiodes. In fact, InGaAs photomixers, such as the UTC p-i-n diode, are well suited for this process. These diodes have an extremely high transit time 3 dB frequency and are compatible with the currently available optical networks and technologies. Yet, UTC diodes reached a transit time 3 dB frequency of 0.31 THz.[90] InGaAs n-i-pn-i-p superlattice photomixers can even be estimated to have transit time 3 dB frequencies of $\nu_{tr} \geq 0.7$ THz. Furthermore, THz photomixers equipped with antennas can directly convert the optical modulation into (sub)THz free space radiation. They are an ideal sender-converter for wireless LAN applications. A proof of principle of such a system using UTC p-i-n diodes is given in Refs. 106 and 128. A 120/125 GHz carrier frequency WLAN, fulfilling the 10 GbE standard, was implemented. An optical CW signal is double sideband modulated at 60 (62.5) GHz using an RF-fed Mach–Zehnder modulator. The optical carrier is eliminated using a filter structure[200] just leaving the two sidebands with a difference frequency of 120 (125) GHz. This way, the optical frequency noise is common for both sidebands. Only the RF noise of the modulator, which can be in the (sub)Hz range, remains. A second Mach–Zehnder modulator modulates the data onto the optical signal. Another, more cost-effective solution for modulating a signal on the THz beam is directly bias-modulating the UTC mixer[168] with the signal instead of the implementation of a second Mach–Zehnder interferometer. The bandwidth used is 116.5–133.5 GHz. An in-line EDFA amplifies the signal and feeds a UTC diode that converts the modulation into a waveguide-fed RF signal. For high output power, the waveguided THz signal is amplified by an InP-HEMT and radiated into free space by an appropriately designed large aperture antenna with a diameter of 375 mm. The THz signal was transmitted over about 200 m. The receiver consisted of a similar antenna feeding a HEMT preamplifier followed by a Schottky-barrier detector diode for conversion into an electrical signal. For measuring the bit error rates (BER), the resulting RF signal was again modulated on an optical carrier for comparison of sent and received signal using a OC-192 network tester. A schematic of the setup is depicted in Fig. 44(c).

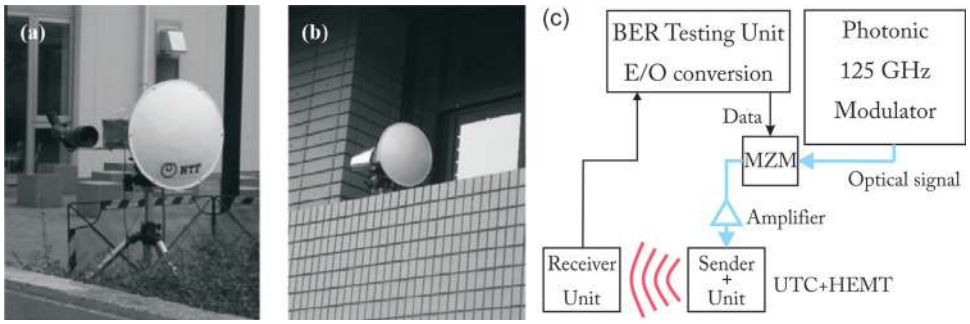

FIG. 44. (Color online) Prototypes of (a) the transmitter core and b) the receiver core for UTC diode–based WLAN system. Reprinted with permission from A. Hirata, H. Takahashi, R. Yamaguchi, T. Kosugi, K. Murata, T. Nagatsuma, N. Kukutsu, and Y. Kado, J. Lightwave Technol. **26**, 2338 (2008). © 2008, IEEE (c) Schematic setup for BER measurement.

Chains of random signals were transferred over the WLAN link and the sent and received signals were compared, achieving a BER of $< 10^{-12}$ at good weather conditions. In a next step, the minimum received power necessary to fulfill the BER requirements for 10 GbE was evaluated to be able to estimate the maximum transmission length at any weather condition. The maximum transmission distance at dry weather conditions was estimated to be up to 3 km and still 500–600 m in rain (120 mm/h) for this system.[106]

Such a system is capable of cost effectively bridging a WLAN between two adjacent buildings, where installing new optical fibers in the ground is too expensive. The 120 GHz signal almost behaves as an optical beam, i.e., it can be easily focused and there is only little scattering. This allows for efficient point-to point transmission, providing high transmission efficiencies as long as the line of sight is not blocked. This technology can readily apply the currently developed schemes for radio over fiber technologies (RoF). In future systems, a pair of laser beams or a double sideband-modulated, carrier-suppressed laser beam could be distributed in an optical network using dispersion-shifted fibers and then be readily converted into (sub)THz signals by photomixers. Ongoing research also provides solutions for up converting the THz signals (> 1 THz) on an optical carrier where RF Mach–Zehnder modulation is no longer applicable. For instance, a quantum-cascade laser was successfully used to modulate a 2.8 THz signal on an optical carrier by using the THz-induced anomalous dispersion in the lasing medium.[201] A photomixer with a resonant antenna can be used to down convert the modulation again. Such systems could provide solutions for future high-speed networks. A detailed review of the state-of-the-art of THz telecommunication is given by Federici and Moeller.[202] Their article also includes a valuable discussion of possible applications and of the requirements to be met.

IV. SUMMARY AND OUTLOOK

In this review the different approaches for CW-THz generation by photoconductive and by p-i-n–based photomixers have been discussed in detail, highlighting their strengths and shortcomings. Besides the established antenna-based (AE) scheme, particular attention has been paid to the emerging concept of antennaless large area emitters (LAEs). Regarding photoconductive AEs, we have reviewed GaAs-based mixers operating at 850 nm using LT-GaAs or ErAs:GaAs superlattices to achieve short recombination times, as well as the efforts undertaken to overcome the high dark conductivity in InGaAs photoconductive AEs for operation in the economically more attractive telecom wavelength range around 1550 nm. The most promising schemes include heavy ion bombardment of InGaAs, implanting deep traps or locally destroying the lattice and thus creating recombination centers. Another method uses a superlattice of monolayers of ErAs in an InGaAs matrix. Quasimetallic states for efficient recombination of electrons and holes are formed by the ErAs layers. A third method uses a superlattice of LT-InGaAs and LT-InAlAs layers with deep traps in the latter for capturing free carriers. Weak Be doping is used to compensate for the high n-background. All these methods have proven capable of producing THz radiation and are continually improved. Much higher responsivities than in photoconductors can be achieved with p-i-n–based AEs. In uni-traveling-carrier (UTC) p-i-n photomixers, the maximum output power level has exceeded that of the best photocondutors in AEs by almost an order of magnitude (24 μW at 914 GHz for UTC p-i-n vs. 2 μW at 1 THz for LT-GaAs based photoconductive mixers). The power of UTC p-i-n diodes is very close to the theoretically expected value. These high-frequency optimized p-i-n diodes have now achieved a transit time 3 dB frequency of 310 GHz. The diode designs require a compromise between the internal reaction speed (transit time roll-off) and the RC time constant of the device capacitance C and antenna radiation resistance R. An independent optimization of RC and transit time can be achieved by using a stack consisting of a sufficient number of transport-optimized p-i-n diodes. Although the implementation of this n-i-pn-i-p photomixer concept is still ongoing, an output power exceeding 0.65 μW $\pm$ 0.15 μW at 1 THz could yet be demonstrated in InGaAs devices. Technological challenges, but no fundamental physical limitations, have to be overcome to reach the high roll-off frequencies and the resulting much higher power levels expected according to the concept. Improved thermal management should lead to much higher power levels.

Even higher input power can be tolerated in large area emitters (LAEs), due to a strongly reduced power density. Although the radiation efficiency of LAEs is strongly reduced due to their low radiation resistance, the strong directivity and the negligible RC roll-off makes both photoconductive and pin-based LAEs attractive. At present, there are no reports of experimental results on CW-LAEs. However, record power values have very recently been reported from LAEs under pulse excitation. Considering the good

agreement of these results with theory, LAEs also appear to be a very appealing alternative for future CW-THz generation by photomixing.

The second part of this review deals with key applications for CW photomixers. Several (quasi)optical THz components for applications in CW-THz systems have been shown. We reviewed experiments demonstrating that the THz linewidth of CW photomixers only depends on the linewidths of the lasers, thus allowing for spectrally very pure, but at the same time, frequency tunable THz beams. Such sources are particularly interesting for spectroscopic applications. Several groups demonstrated the feasibility, ease of use, and possible ultrahigh spectral purity of CW photomixing systems. As an example, the rotational lines of acetonitrile were ultra-fine resolved in a narrow frequency window of less than 100 MHz, containing just a few modes. Also artificial, photonic atoms (and artificial, photonic molecules), i.e., THz whispering gallery mode resonators (or coupled resonators) have been spectroscopically studied in a similar way. Shape-related theories such as the introduction of a finite scatterer for efficient outcoupling can be examined in the THz frequency range. The 100 to 1000 times larger geometrical dimensions allow for easy resonator structuring as demonstrated for mode-matched and coupled resonators. The results are directly transferable to the optical domain due to the scalability of electromagnetism. In the optical domain, however, feature sizes in the sub-μm range require very accurate, sophisticated, expensive high-end fabrication tools.

CW photomixers can also be used in astronomical spectroscopy and imaging. An excellent example is the Atacama Large Millimeter/Submillimeter Array where UTC photomixers are considered as local oscillators. They may be driven with two highly stabilized lasers that are distributed in the array of antennas to achieve mutual coherence between the local oscillators and, subsequently, the receivers. This way, the set of 64 receiver telescopes, each with a 12 m diameter, will behave as a single receiver with a huge aperture. A CW photomixer as local oscillator could provide an on-site THz signal around 100 GHz by photomixing the distributed laser signals. The resulting THz radiation could be amplified and frequency multiplied to the desired frequency band. Then it will be mixed with the received radiation from outer space and down converted to provide an IF signal. Further down conversion allows for transfer via RF lines to a central data evaluation building.

Another very appealing field of applications for CW photomixers are high-frequency wireless LANs. Yet, modulated telecom wavelength beams are used for data transfer at GHz frequencies. For the sake of increasing data transmission rates, future systems require higher modulation frequencies. The modulation frequency (and the bandwidth) will have to enter the THz frequency range to keep up with the increasing requirements for high speed networks and greater data throughput. A THz photomixer is a straightforward transmitter concept to convert the optical signal into a free space THz signal for future wireless LANs. It is already compatible with existing technology and the first proof of principle experiments showed its feasibility at 120 and 125 GHz. Arbitrary signals were transmitted over 200 m, fulfilling the 10 Gb ethernet standards. The available power largely exceeded the level required to comply with the 10 GbE standard. Estimates show that this scheme should work up to distances of 500–600 m, even in rainy weather (120 mm/h) conditions.

In this review, a wide range of applications for continuous-wave Terahertz photomixers was addressed. The ongoing development of photomixers and Terahertz detectors makes CW systems an appealing and less expensive alternative to the commonly used pulsed THz time domain systems. Potentially, photomixers even allow for higher speed of data acquisition and, at the same time, offer higher spectral purity.

APPENDIX A: FREQUENCY DEPENDENCE OF THE TRANSIT TIME ROLL-OFF OF p-i-n–BASED ANTENNA EMITTERS (AEs)

In the following, we derive the roll-off expressions for the AC electron and hole current in a p-i-n diode from Sec. II D 2. We assume that electron hole pairs are generated by absorption of an incident modulated optical power $P_L(z,t) = P_{L,0}(z)[\cos(2\pi\nu_{THz}t) + 1]$ in the intrinsic layer of a p-i-n diode (see Fig. 45). For the most general case, we allow for spatial dependence of the absorption coefficient $\alpha(z)$ within the intrinsic layer. The electron-hole $(n-p)$ carrier generation rate at time t and position z in a diode with cross section A is

$$A\dot{n}(z,t) = A\dot{p}(z,t) = \alpha(z)\frac{P_L(z,t)}{h\nu_0}. \tag{A1}$$

In order to calculate the resulting current observed in the diode we have to recall first that an electron, generated in the i-region of a p-i-n diode at the position z $(0 < z < d_i)$ at an (earlier) time t' $(t' < t)$ induces a displacement current in the

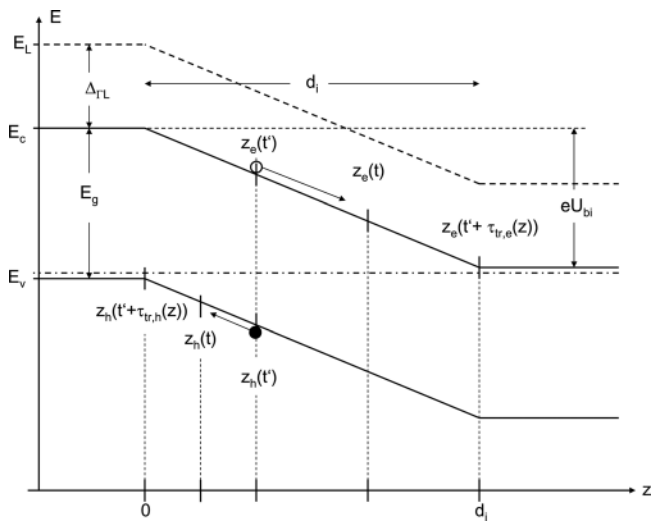

FIG. 45. Schematic energy diagram (solid lines) of an InGaAs p-i-n diode at zero bias, showing the valence band and the Γ- and L- (dashed line) conduction bands. Electrons generated near $z=0$ can propagate ballistically at $\bar{v}_{bal} \gg v_{sat}$ over more than 1/2 of the intrinsic layer in the lower conduction band before being scattered into the L valley, where they are slowed down to v_{sat}. With moderate forward bias, the transport regime can be extended over the whole i-layer. Under reverse bias, the transit time becomes increasingly dominated by the nonballistic part of transport with the much smaller saturation velocity. The point $z_e(t') = z_h(t')$ indicates the position at which an electron-hole pair was generated at the time t'. The points $z_e(t)$ and $z_h(t)$ depict the positions at a later time t and $z_e[t' + \tau_{tr,e}(z)] = d_i$ and $z_h[t' + \tau_{tr,h}(z)] = 0$.

contact layers. This displacement current is flowing while the electron is traveling from its generation point z to the n-contact, and stops upon arrival at the contact, $z = d_i$ (see Fig. 45). During this transit time $\tau_{tr,e}(z)$, which depends on the distance of $d_i - z$ from the contact layer and on the evolution of the velocity $v_e(z, t - t')$, the current generated by a single electron at time t is given by

$$\begin{aligned} i_e(z, t - t') &= e v_e(z, t - t')/d_i \quad \text{for } t - \tau_{tr,e}(z) < t' < t \\ i_e(z, t - t') &= 0 \quad \text{else.} \end{aligned} \tag{A2}$$

From Eq. (A2) we see that an electron contributes to the displacement current at time t, if it has been generated at a time t' within the time interval $[t - \tau_{tr,e}(z), t]$. An electron generated at z contributes only the fraction

$$\begin{aligned} q_e &= \int_{t'}^{t'+\tau_{tr,e}(z)} i_e(t - t') \\ dt &= (e/d_i) \int_0^{\tau_{tr,e}(z)} v_e(z, t'') \\ dt'' &= e \frac{d_i - z}{d_i} \end{aligned} \tag{A3}$$

of an elementary charge during its transit time (the complementary fraction being contributed by the hole generated at the same time t'). The transit time $\tau_{tr,e}(z)$ is defined by the integral equation

$$\int_{t'}^{t'+\tau_{tr,e}(z)} v_e(z, t - t') dt = d_i - z. \tag{A4}$$

Corresponding expressions apply for the holes. Note that in the integral equation for the hole transit time, $d_i - z$ has to be replaced by z, as the holes are traveling in the opposite direction toward the p-contact layer, i.e.,

$$\int_{t'}^{t'+\tau_{tr,h}(z)} v_h(z, t - t') dt = z. \tag{A5}$$

Figure 46 shows the current $i_e(t - t')$ for three different idealized transport regimes, namely a fully absorbing standard p-i-n diode, and diodes with either carrier transport at the saturation velocity or ballistic transport that only absorb within a small area close to the p-contact. To calculate the total displacement current at time t originating from absorption within $[z, z + dz]$, all the contributions $i_e(t - t')$ due to all electrons generated at times t' within the transit interval $[t - \tau_{tr,e}(z), t]$ are included. This yields

$$\begin{aligned} dI_e(t, z) &= \int_{t-\tau_{tr,e}(z)}^{t} \dot{n}(z, t') i_e(z, t - t') dt' dV \\ &= \frac{e\alpha(z)}{h\nu_0 d_i} \int_{t-\tau_{tr,e}(z)}^{t} P_L(z, t - t') v_e(t - t') dt' dz. \end{aligned} \tag{A6}$$

The total current at time t is then obtained by integration over the whole intrinsic region, i.e.,

$$I_e(t) = \frac{e}{h\nu_0 d_i} \int_0^{d_i} \alpha(z) \int_{t-\tau_{tr,e}(z)}^{t} P_L(z, t') v_e(z, t - t') dt' dz. \tag{A7}$$

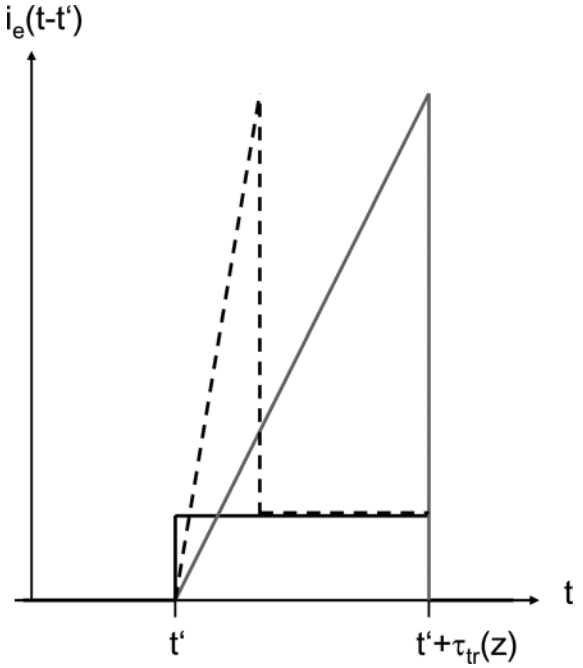

FIG. 46. Displacement current $i_e(t-t')$ of an electron generated at the position z for three idealized typical transport regimes. The solid black line corresponds to the case of very high fields ($\gg$ 20 kV/cm), where the electron acquires its nearly constant saturation velocity $v_e(t-t') = v_{sat} \approx 10^7$ cm/s within a negligibly small time interval. The lighter solid line corresponds to purely ballistic transport $v_{bal}(t-t') = (e|\vec{E}|/m_c)(t-t')$, which applies for moderate electric fields (3 kV/cm $< |\vec{E}| <$ 50 kV/cm) as long as the electron does not reach the threshold energy $\Delta_{\Gamma L}$ for inter-valley scattering. The dashed line depicts partial ballistic transport for $e|\vec{E}|d_i \gg \Delta_{\Gamma L}$. The ballistic overshoot is followed by drift with the saturation velocity when the electron reaches the kinetic energy of $E_{kin} = \Delta_{\Gamma L}$.

Substituting $t - t' = \tau$ provides

$$\begin{aligned} I_e(t) = \frac{1}{d_i} \int_0^{d_i} \frac{eP_{L,0}(z)}{h\nu_0} \alpha(z) \\ \times \int_0^{\tau_{tr,e}(z)} \{\cos[2\pi\nu_{THz}(t - \tau)] + 1\} v_e(z, \tau) d\tau dz. \end{aligned} \tag{A8}$$

We will now discuss three interesting cases, representing idealized versions of different real implementations of pin-based AEs.

(a) Absorption within a narrow region of (negligible) width Δz near $z = 0$. We get for the absorption $\alpha(z) \approx \delta(z)\alpha_0\Delta z$ with α_0 being the absorption constant of the semiconductor at the optical frequency ν_0. In this case, the resulting photocurrent is due to electrons only [Fig. 46(a)]. The contribution of the holes is negligible, as they are generated at the p-contact layer. Furthermore, the electrons are assumed to travel through the i-layer at their high-field saturation velocity, i.e. $v_e = v_{sat} =$ constant. This corresponds to the case of a reverse bias of several volts applied to the p-i-n diode. The electrons are slowed down to v_{sat} after a (very) short ballistic flight. These assumptions represent a simplified version of the uni-traveling-carrier (UTC) photodiode. This scenario reduces Eq. (A8) to

$$I(t) = \frac{v_{sat}}{d_i} \cdot \frac{eP_{L,0}}{h\nu_0} \alpha_0 \Delta z \int_0^{\tau_{tr,e}} \{[\cos[\omega_{THz}(t - \tau)] + 1\} d\tau, \tag{A9}$$

with $\omega_{THz} = 2\pi\nu_{THz}$. Integration provides

$$I(t) = \frac{eP_{L,0}}{h\nu_0}\alpha_0\Delta z\left\{\mathrm{sinc}\left(\frac{\omega_{THz}\tau_{tr,e}}{2}\right) \cdot \sin[\omega_{THz}(t-\tau_{tr,e}/2)] + 1\right\}. \quad \text{(A10)}$$

Here, we have taken into account that $\tau_{tr,e} = d_i/v_{\mathrm{sat}}$. The DC part is the expected average current generated by the absorbed optical power within Δz of

$$I_{DC} = I_0^{id} = \frac{eP_{L,0}}{h\nu_0}\alpha_0\Delta z. \quad \text{(A11)}$$

The amplitude of the AC current, $I_{AC}(\omega_{THz})$, however, exhibits a roll-off of

$$I_{AC}(\omega_{THz}) = I_0^{id}\mathrm{sinc}\left(\frac{\omega_{THz}\tau_{tr,e}}{2}\right). \quad \text{(A12)}$$

As $P_{THz} = \frac{1}{2}R_A I_{AC}^2 \propto I_{AC}^2$, the (power) 3 dB frequency is at $I_{AC}(\omega_{THz}) = I_0^{id}/\sqrt{2}$, providing

$$\nu_{tr} \approx 0.44/\tau_{tr,e}. \quad \text{(A13)}$$

The roll-off of the AC amplitude [Eq. (A12)] yields a frequency dependence of the emitted THz power, which differs from the simple behavior assumed in Eqs. (34) and (35), especially above its 3 dB frequency. Below this frequency, Eq. (34) still provides a good approximation. (For a discussion of these results, see II D 2 b).

(b) Absorption within a narrow region of (negligible) width Δz near $z = 0$, with ballistic transport of the electrons. In this case, $v_e(t) = v_{\mathrm{bal}}(t) \approx (e|\vec{E}|/m_e^*)t$ is representing an idealized version of the ballistic transport p-i-n diodes in the n-i-pn-i-p-AEs in Sec. II D 6. The hole contributions are again negligible. Eq. (A7) now reduces to

$$I(t) = \frac{e|\vec{E}|}{m^* d_i}\cdot\frac{eP_{L,0}}{h\nu_0}\alpha_0\Delta z\int_0^{\tau_{\mathrm{bal}}}\tau\{\cos[\omega_{THz}(t-\tau)]+1\}\tau, \quad \text{(A14)}$$

with $\tau_{\mathrm{bal}} \approx \sqrt{2m^* d_i/(e|\vec{E}|)} \geq d_i\sqrt{2m^*/\Delta_{\Gamma L}}$. More accurate values for τ_{bal} can be obtained from the simulations summarized in Fig. 7. By integration, we obtain

$$I(t) = \frac{eP_{L,0}}{h\nu_0}\alpha_0\Delta z\left\{1 + \frac{2}{x^2}[(\sin x - x\cos x)\sin\omega_{THz}t + (x\sin x + \cos x - 1)\cos\omega_{THz}t]\right\}, \quad \text{(A15)}$$

with $x = \omega_{THz}\tau_{\mathrm{bal}}$. The DC current is the same as in case (a), Eq. (A11), as expected. The frequency dependence of the AC current is

$$I_{AC}^{\mathrm{bal}}(x,t) = I_0^{id}\frac{2}{x^2}\sqrt{(\sin x - x\cos x)^2 + (x\sin x + \cos x - 1)^2)} \times \sin[\omega_{THz}t + \Phi(x)] \quad \text{(A16)}$$

The (power) 3 dB frequency is

$$\nu_{tr} = 0.554/\tau_{\mathrm{bal}} \quad \text{(A17)}$$

Although Eq. (A13) provides a very similar expression for the 3 dB frequency, it should be noted that τ_{bal} is much shorter than $\tau_{tr,e}$ for transport with the saturation velocity. Hence, ballistic transport strongly increases the transit time 3 dB frequency. (These results are further analyzed in Sec. II D 2).

(c) Uniform absorption in the intrinsic layer, $\alpha(z) = \alpha_0 = \text{constant}$. For simplicity, we assume relatively small absorption coefficients such that we can neglect the absorption of optical power along z according to Beer's law. We assume $P_{L,0}(z) = P_{L,0}$ instead. For the electron transport we take again the high-field limit, i.e. $v_e = v_{\mathrm{sat}} = \text{constant}$. For the much heavier holes we assume that their velocity follows $v_h = \mu_h|\vec{E}| = \text{constant}$, with the hole mobility μ_h. These assumptions represent an idealized, but rather realistic version of a standard double hetero (DH) p-i-n diode with absorption within the whole i-region. The total current is now the sum of the electron and hole contributions. The expression for the currents $I_j(t) = [I_e(t), I_h(t)]$ is formally the same for electrons and holes, respectively. It differs only by the different velocities $v_j = (v_{\mathrm{sat}}, v_h)$ and respective transit times $\tau_{tr,j} = (\tau_{tr,e}, \tau_{tr,h})$.

$$I_j(t) = \frac{v_j}{d_i}\cdot\frac{eP_{L,0}}{h\nu_0}\alpha_0\int_0^{d_i}\int_0^{\tau_{tr,j}(z)}\{\cos[\omega_{THz}(t-\tau)]+1\}d\tau dz. \quad \text{(A18)}$$

With

$$\tau_{tr,e} = \frac{d_i - z}{v_{\mathrm{sat}}} \quad \text{for electrons.} \quad \text{(A19)}$$

$$\tau_{tr,h} = \frac{z}{\mu_h|\vec{E}|} \quad \text{for holes,} \quad \text{(A20)}$$

the integration provides

$$I_j(x_j,t) = \frac{1}{2}\frac{eP_{L,0}}{h\nu_0}\alpha_0 d_i + \frac{eP_{L,0}}{h\nu_0}\alpha_0 d_i\frac{1}{x_j^2}[(\sin x_j - x_j)\cdot\sin\omega_{THz}t + (\cos x_j - 1)\cos\omega_{THz}t] \quad \text{(A21)}$$

with $x_j = \omega_{THz}\tau_{tr,j}$. For the DC part of the current we get

$$I_{DC,e} = I_{DC,h} = \frac{1}{2}\frac{eP_{L,0}}{h\nu_0}\alpha_0 d_i = \frac{I_0^{id}}{2}. \quad \text{(A22)}$$

The AC current is

$$I_j^{(AC)}(x_j,t) = \frac{I_0^{id}}{x^2}[(\sin x_j - x_j)\sin\omega_{THz}t + (\cos x_j - 1)\cos\omega_{THz}t]. \quad \text{(A23)}$$

In the limit $x_j \to 0$, $I_j^{(AC)}(x_j \to 0, t) = \frac{I_0^{id}}{2}\cos\omega_{THz}t$, reflecting the fact that electrons and holes contribute equally to the current with $I_e = I_k = I_0/2$ at low frequencies. Expressing $I_j^{(AC)}(x_j,t)$ in polar form yields

$$I_j^{(AC)}(x_j,t) = \frac{I_0^{id}}{x_j^2}\sqrt{(\sin x_j - x_j)^2 + (\cos x_j - 1)^2}\sin[\omega_j t - \Phi(x_j)] \quad \text{(A24)}$$

$$\Phi(x_j) = \arctan\frac{\cos x_j - 1}{\sin x_j - x_j} \quad \text{(A25)}$$

The individual 3 dB frequencies (i.e., where the individual AC amplitudes have decreased from the maximum amplitude of $I_0/2$ by a factor of $\sqrt{2}$) are

$$v_{tr,j} = 0.55/\tau_{tr,j}^{\max}, \tag{A26}$$

with $\tau_{tr,j}^{\max} = d_i/v_j$. The THz power emitted from a standard p-i-n diode is given by the total AC current,

$$P_{THz}^{\text{pin}}(\omega) = \frac{1}{2} R_A [I^{(AC)}(x_e,t) + I^{AC}(x_h,t)]^2. \tag{A27}$$

For the case of $v_e \gg v_h$, the THz power will decrease by a factor of 4 above (a relatively low) frequency of $v_{tr,h} = 0.55 v_h/d_i$ and then mainly follow the electron roll-off with a 6 dB frequency of $v_{tr,e} = 0.55 = v_e/d_i$.

(d) The results of (a)–(c) can also be used to express partial ballistic transport across the intrinsic layer for both absorption close to the p-contact and uniform absorption. This case of intermediate fields represents the most realistic expression for UTC diodes with a significant contribution from ballistic electron transport. However, deriving an exact analytic expression ends up in lengthy mathematics. We refer to the work of Feiginov,[93] where realistic cases of UTC diodes were treated.

APPENDIX B: SCREENING OF THE ELECTRIC FIELD IN p-i-n DIODES DUE TO PHOTOGENERATED SPACE CHARGES

At large photocurrent densities in p-i-n diodes, a quasistationary space charge develops in the i-layer. In this appendix, we provide some estimates of the potential associated with this space charge and for its effect on the mixer performance. The partial screening of the original uniform field can result in drastically increased transit times, if the current densities become too high. This limits the possibilities of reducing the device cross section A at a given current I, which otherwise would be desirable in order to obtain small capacitances and, hence, high RC 3 dB roll-off frequencies for the photomixer.

1. Standard p-i-n diode with nonballistic transport

First, we consider the case of a standard p-i-n diode (Fig. 45) with uniform absorption, $\alpha(z) = \text{const}$. We neglect the spatial variation of the optical power due to the Lambert–Beer law (i.e., we assume the case of a weakly absorbing sample) and assume uniform carrier generation in the intrinsic layer. At frequencies above the roll-off frequencies, it is sufficient to consider the time averages of the quantities of interest (indicated by bars). We assume that the laser power P_L of photon energy $h\nu_0$ is uniformly focused onto the device area A. The (average) photon flux density $\bar{P}_L/(h\nu_0 A)$ yields a spatially constant (time-averaged) electron and hole generation rate

$$\frac{d\bar{n}}{dt} = \frac{d\bar{h}}{dt} = \alpha_0 \frac{\bar{P}_L}{h\nu_0 A}. \tag{B1}$$

Neglecting internal carrier recombination, the continuity condition for the electron and hole current densities provides[203]

$$\operatorname{div} \bar{j}_e = -\frac{d}{dz}[e v_e \bar{n}(z)] = -e\frac{d\bar{n}}{dt} = -\alpha_0 \frac{e\bar{P}_L}{h\nu_0 A} = \text{const.} \tag{B2}$$

$$\operatorname{div} \bar{j}_h = \frac{d}{dz}[e v_h \bar{p}(z)] = e\frac{d\bar{p}}{dt} = \alpha_0 \frac{e\bar{P}_L}{h\nu_0 A} = \text{const.} \tag{B3}$$

if the velocity of electrons and holes does not depend on the coordinate z. This is justified if the electric field $|\vec{E}|$ in the intrinsic region is (nearly) constant. The z integration yields

$$\bar{j}_e(z) = -\alpha_0 d_i \frac{e\bar{P}_L}{h\nu_0 A} \cdot \frac{z}{d_i}. \tag{B4}$$

and

$$\bar{j}_h(z) = -\alpha_0 d_i \frac{e\bar{P}_L}{h\nu_0 A} \cdot \frac{d_i - z}{d_i} \tag{B5}$$

with the total current

$$\bar{j} = \bar{j}_e + \bar{j}_h = -\frac{eP_L^{\text{abs}}}{h\nu_0 A} \tag{B6}$$

where we substituted $P_L^{\text{abs}} = \alpha_0 d_i \bar{P}_L$. This is the optical power absorbed in the volume Ad_i.We are interested in the electron and hole densities in order to calculate the space charge density $\bar{\rho}(z) = e\bar{p}(z) - e\bar{n}(z)$, the resulting screening fields, and the space charge potential, which distorts the linear potential drop in the i-region of the p-i-n diode at a given current $\bar{I} = \bar{j}A$. The average carrier densities follow from Eqs. (B4) to (B6) as

$$\bar{n}(z) = \frac{|\bar{j}|}{e v_e} \cdot \frac{z}{d_i}. \tag{B7}$$

and

$$\bar{p}(z) = \frac{|\bar{j}|}{e|v_h|} \cdot \frac{d_i - z}{d_i}. \tag{B8}$$

We see that the space charge densities at a given current $\bar{I}$ are inversely proportional to the cross section A and the carrier velocity. The space charge density is given by

$$\rho(z) = e[\bar{p}(z) - \bar{n}(z)] = \rho_0 \left(1 - \frac{z}{z_0}\right) \tag{B9}$$

with $\rho_0 = \bar{j}/v_h$ and $z_0 = d_i/(1 + v_h/v_e)$. The space charge depends linearly on z and changes sign at $z = z_0$.

In Fig. 47(a), the stationary charge densities associated with the electron and hole currents are depicted for $|I| = 13$ mA, A $= 35\ \mu\text{m}^2$, $d_i = 300$ nm (as used in Sec. II D 3) and an electric field $|\vec{E}| = 40$ kV/cm, corresponding to $U_{\text{bi}} - U_0 = 1.2$ V for InGaAs as an example. We assume that at $|\vec{E}| = 40$ kV/cm the electrons are propagating at the saturation velocity $v_e = v_{\text{sat}} = 10^7$ cm/s and the holes with $v_h = 3 \cdot 10^6$ cm/s.[96] In this case, the space charge density distribution is dominated by the relatively slow holes and becomes negative only at $z > z_0 \approx 230$ nm.

To estimate the influence of this space charge, we solve Poisson's equation for the space charge–induced field,

$$\frac{dE_z^{sc}}{dz} = \frac{\rho(z)}{\epsilon_0 \epsilon_r} = \frac{\rho_0}{\epsilon_0 \epsilon_r}\left[1 - \frac{z}{z_0}\right] \tag{B10}$$

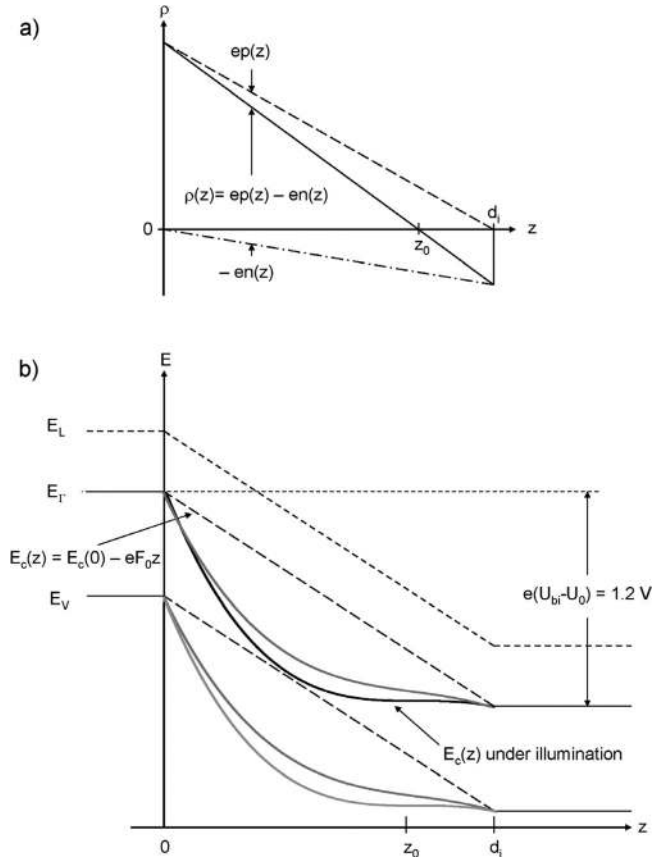

FIG. 47. (a) Charge density distribution in a p-i-n diode assuming constant absorption over the total intrinsic layer with transport at the saturation velocity. (b) Band diagram in the dark state (dashed line) and under illumination for $I = 16.4$ mA (black solid line), and $I = 13$ mA (gray solid line), for a device with a cross section of 35 μm^2 for a fixed total voltage drop in the junction of 1.2 V.

The electric field becomes

$$E_z^{sc}(z) = \frac{\rho_0}{\epsilon_0\epsilon_r}\left[z - \frac{z^2}{2z_0}\right] = -\frac{\rho_0}{\epsilon_0\epsilon_r}\left[\frac{(z-z_0)^2}{2z_0} + \frac{z_0}{2}\right]. \quad \text{(B11)}$$

The constant part of the space charge field, $\rho_0/(\epsilon_0\epsilon_r)\cdot z_0/2$ can easily be compensated for by an external bias. We therefore neglect this contribution in the following as we are only interested in saturation effects that impede carrier transport. The space charge potential then changes with the third power in $(z - z_0)$ as

$$U_{\text{pin}}^{sc}(z) = -\frac{\rho_0}{6z_0\epsilon_0\epsilon_r}(z-z_0)^3. \quad \text{(B12)}$$

The total (nonlinear) space charge–induced potential drop is

$$U_{\text{pin}}^{sc} = U_{\text{pin}}^{sc}(d_i) - U_{\text{pin}}^{sc}(0) = \frac{\rho_0}{6z_0\epsilon_0\epsilon_c}\left[(d_i - z_0)^3 + z_0^3\right]$$
$$= \frac{\bar{j}}{6\epsilon_0\epsilon_r}\left[\frac{1 - v_h/v_e + (v_h/v_e)}{v_h(1 + v_h/v_e)}\right]d_i^2 \propto \bar{j}d_i^2 \quad \text{(B13)}$$

It is clear that band bending due to the quasistationary space charge accumulation in the i-layer becomes drastic if the total space charge potential drop becomes comparable with the potential drop in the i-layer in the absence of space charges, i.e., $E_C(d_i) - E_C(0) = -e(U_{bi} - U_0)$ [see dashed line in Fig. 47(b)].

For our example, the space charge potential drop from Eq. (B13) would become $U_{\text{pin}}^{sc} = (U_{bi} - U_0) = 1.2$ V for a current of $I = 16.4$ mA [see full lines in Fig. 47(b)], according to our simplified model. According to Eq. (B12), the electric field would become zero at the inflection point, z_0. This implies that in this region both hole and electron current would be due to diffusion only. It is clear that in the strong screening regime, our model ought to be replaced by a model which self-consistently accounts for the space charge–induced spatial variation of the drift velocities with the local field, $|v_{e,h}(z)| = \mu_{e,h}|E(z)|$. For significantly smaller currents, however, our model can, at least qualitatively, describe the real situation. From Eq. (B12) we see that U_{pin}^{sc} scales linearly with the current. This implies that a reduction of the current by a factor of 2, e.g., would still result in a reduction of the field around the inflection point, z_0, by a factor of 2 compared to its original value. In this case, the strongly reduced hole drift velocity would lead to a significant, but perhaps still tolerable, degradation of the transport roll-off for holes.

So far, we have assumed electron motion with the saturation velocity. In realistic diodes, electrons will generally propagate ballistically after generation until they reach the threshold energy for inter-valley transfer from the Γ-valley (with very small effective mass m_e^*, and relatively long momentum relaxation times) to the L-valley (with very large effective mass, m_L, and very short momentum relaxation time). During this time, they travel much faster and, accordingly, contribute more strongly to the displacement current (this overshoot and the resulting ballistic benefit was discussed in Sec. II D 1). The high hole density at high current densities, however, drastically constrains the ballistic transport not only because of the field reduction, but also because of increased electron hole scattering rates. Moreover, the enhanced potential drop near $z = 0$ [see Fig. 47(b)] reduces the width and time during which the transport can be quasiballistic.

2. Nonballistic transport with absorption restricted to a narrow zone near the p-contact layer (UTC diode)

We now turn to the case of diodes with absorption restricted to a narrow region of width Δz near the p-contact layer. As before, we assume that the electrons are traveling mostly with the high field saturation velocity, v_{sat}. The electron current density and the corresponding space charge density now reach their maximum values $\bar{j}_n = \bar{j} = eP_L^{\text{abs}}/(hv_0A)$ (with $P_L^{\text{abs}} = \alpha\Delta z P_L$) and $\bar{n} = \bar{j}/(ev_{\text{sat}})$ within the narrow zone Δz. Vice versa, the hole current and space charge density decrease from their maximum values to zero within this narrow region. As the space charge potential scales with the square of the width of the absorption region [Eq. (B13)], only weak field screening results. The space charge density in the rest of the intrinsic zone is now exclusively due to the electron current. It is given by

$$\rho(z) = -en(z) = \frac{\bar{j}}{v_{\text{sat}}} = \text{const.} \quad \text{(B14)}$$

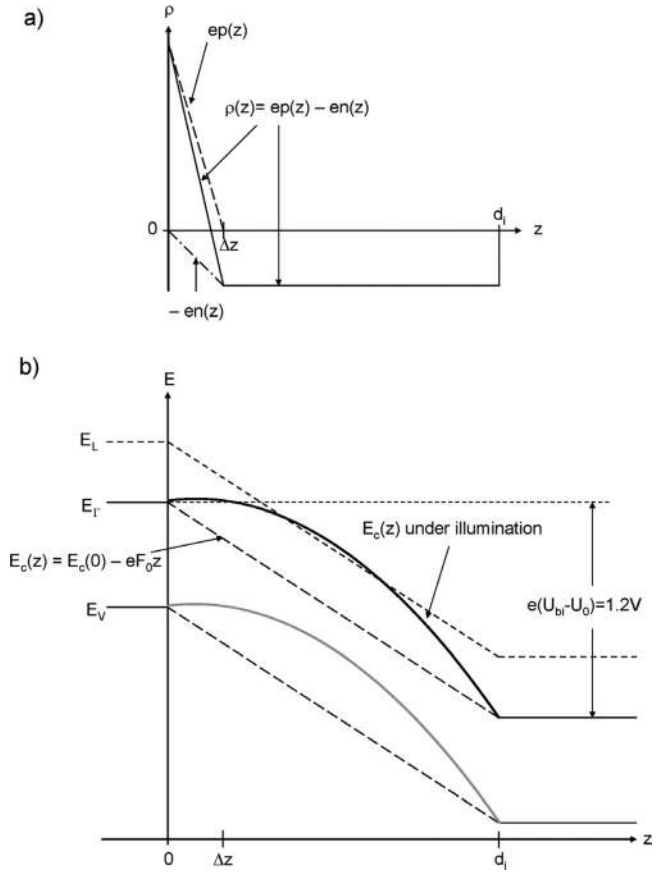

FIG. 48. (a) Charge density distribution for a nonballistic UTC diode. (b) Schematic band diagram in the ground state (dashed line) and under illumination ($I = 13$ mA, $A = 35$ μm^2) for a δ-shaped absorption region ($\Delta z \approx 0$) and a fixed total bias of $U_{bi}-U_0 = 1.2$ V. The maximum of $E_C(z)$ close to the p-contact ($z = 0$) under illumination forms a barrier for electron transport. The appearance of this maximum is referred to as current blocking.[100] To remove this barrier, a higher reverse bias is required. Fields larger than 3 kV/cm are required for transport with v_{sat} at least, requiring a total voltage drop of at least $U_{bi}-U_{ext} = 1.54$ V in the junction. This corresponds to an external bias of only $U_{ext} = -0.2$ V for InP ($E_G = 1.344$ eV)

The resulting space charge potential is

$$U^{sc}_{UTC}(z) = -\frac{\bar{j}z^2}{2\epsilon_0\epsilon_r v_{sat}} \tag{B15}$$

This result is shown in Fig. 48(b). As there are no holes for $z > \Delta z$, the space charge induced (parabolic) band bending now affects only the electron transport. As long as the field is not reduced to $|\vec{E}(z=0)| < 3$ kV/cm, the electron velocity will be $v_e \geq v_{sat}$.

With the values from our previous sample design ($I = 13$ mA, $A = 35$ μm^2, $d_i = 300$ nm), the difference of the (nonlinear) space charge potential between $z = 0$ and $z = d_i$ becomes

$$U^{sc}_{UTC} = U^{sc}(d_i) - U^{sc}(0) = -\frac{\bar{j}d_i^2}{2\epsilon_0\epsilon_r v_{sat}} = -1.45\,\mathrm{V} \tag{B16}$$

Comparing Eq. (B16) with Eq. (B13) we notice that $U^{sc}_{pin} < U^{sc}_{UTC}$ by a factor of 0.63 for a fixed value of $\bar{j}$ and d_i. However, the implications of the critical currents at which the electric field vanishes at z_0 or at the p-contact, respectively, are quite different. We had argued that the tolerable current for standard p-i-n diodes has to be smaller by a factor of 2, at least, whereas a current reduction by 5–10% is sufficient in a UTC diode to turn the operation condition into a regime with strong ballistic benefit.

3. Ballistic transport with absorption restricted to a narrow region near the p-contact

As a result of the relatively low electric fields used for ballistic transport, the contribution of the holes would particularly suffer from low hole velocities. The large space charge densities associated with them would prevent any attractive performance. Hence, we focus on absorption close to the p-contact as in the last section, with pure electron transport. The ideal scenario for ballistic transport in a p-i-n diode is a potential drop within the intrinsic region, $e|\vec{E}|d_i$, just corresponding to the threshold energy $\Delta_{\Gamma L}$, for inter-valley scattering:

$$eU(z) = -\Delta_{\Gamma L}\frac{z}{d_i}. \tag{B17}$$

For an electron generated with negligible kinetic energy at $z = 0$, the ballistic velocity at a point z follows from energy conservation, $E_{kin}(z) + U(z) = \text{const}$. With $E_{kin}(z) = m^*_e[v_{bal}(z)]^2/2$ this yields

$$v_{bal}(z) = \sqrt{\frac{2\Delta_{\Gamma L}z}{m^*_e d_i}} = v^{max}_{bal}\sqrt{\frac{z}{d_i}}, \tag{B18}$$

with $v^{max}_{bal} = \sqrt{2\Delta_{\Gamma L}/m^*_e}$.

This provides values for the ideal maximum ballistic velocity of $v^{max}_{bal} = 1\cdot 10^8, 1.6\cdot 10^8$, and $1.85\cdot 10^8$ cm/s for GaAs, InP, and InGaAs, respectively. According to the accurate theoretical simulation in Fig. 7 [or as a result of Eq. (B18)], the ballistic velocity of the electrons exceeds the saturation velocity $v_{sat} = 10^7$ cm/s within less than 1% of the intrinsic region (for fields in the range of a few kV/cm). The width of the absorbing region, Δz, is typically significantly broader. Thus, electrons are, at least, traveling with ballistic velocities exceeding v_{sat}, when they leave the generation zone. The space charge field within the generation zone, $z < \Delta z$, is again negligible for the same reason as in the case described in the previous section. For $z > \Delta z$, the local space charge density is again solely due to the ballistic electrons. It is well approximated by

$$\rho^{sc}(z) = -e\bar{n}(z) = \frac{\bar{j}}{v_{bal}(z)} = \frac{\bar{j}}{v^{max}_{bal}}\sqrt{\frac{d_i}{z}} \tag{B19}$$

Here, we have neglected the finite length of the absorption region and that the electron velocity at its point of generation is nonzero because of the finite diffusion velocity and a finite kinetic energy resulting from excitation above the band edge. Neglecting these aspects causes the divergence at $z = 0$. Under these assumptions, the space charge potential becomes

$$U^{sc}_{bal}(z) = -\frac{\bar{j}}{\epsilon_0\epsilon_r v^{max}_{bal}}\left[\frac{4}{3}\sqrt{d_i}z^{3/2} - 2\sqrt{d_i\Delta z}\cdot z + \frac{2}{3}\sqrt{d_i\Delta z^3}\right]. \tag{B20}$$

Neglecting terms containing Δz yields

$$U^{sc}_{bal} = U^{sc}_{bal}(d_i) - U^{sc}_{bal}(0) = \frac{4\bar{j}}{3\epsilon_0\epsilon_r v^{max}_{bal}}d_i^2. \tag{B21}$$

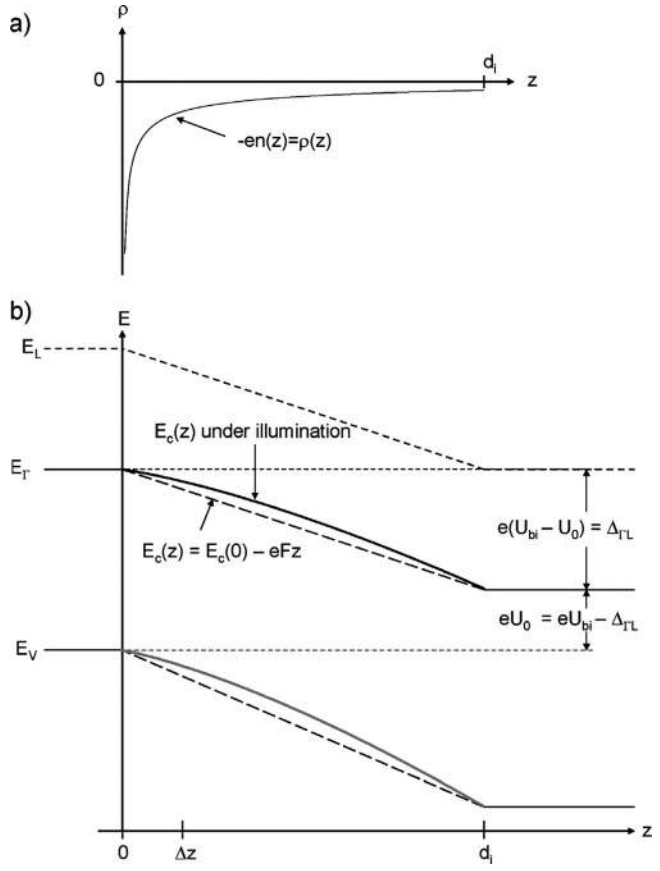

FIG. 49. (a) Electron density distribution for a diode with ballistic transport. b) Band diagram for a ballistically operating diode under dark (dashed line) and illuminated (solid line, I = 20 mA) conditions for $d_i = 300$ nm, an area of 35 μm^2, and a total voltage drop of 1.2 V.

Compared to UTC diodes, this potential drop is by a factor of $8v_{sat}/(3v_{bal}^{max})$ smaller, corresponding to 0.27, 0.17, and 0.13 for GaAs, InP, and InGaAs, respectively. For the previous design parameters and a current of 13 mA this yields $U_{bal}^{sc} = 0.35\,eV$, 0.22 eV, and 0.18 eV for the respective materials. A comparison to the corresponding values for $\Delta_{\Gamma L} = 0.25, 0.59$, and 0.46 eV shows that for a current of I = 13 mA screening becomes a considerable problem for ballistic transport in GaAs, whereas even significantly higher currents can be tolerated in InP and InGaAs diodes.

In Fig. 49(b), the band profiles and the electron density are depicted for vanishing photocurrent (dashed lines) for $e(U_{bi} - U_0) = \Delta_{\Gamma L}$ (i.e., forward bias) for InGaAs and, this time, I = 20 mA (solid line). The field near $z = 0$ is reduced by about a factor of 2. This would considerably increase the transit time and reduce the transit time 3 dB roll-off frequency. Weak n-doping introduced into the i-layer can help to maintain considerably high fields near $z = 0$.

APPENDIX C: RELATIONS BETWEEN EXTERNAL CURRENT, SHEET CARRIER DENSITY, SOURCE TERM, *D*(*t*), AND INCIDENT OPTICAL POWER

In order to calculate the THz power emitted by an LAE device, we need to relate the incident optical power and the externally detectable photocurrent to the sheet carrier density which is the source term for generation of carriers by (quasi)

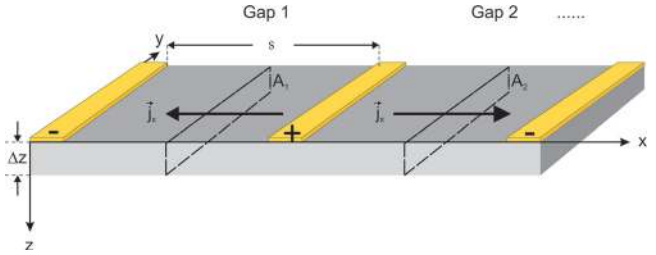

FIG. 50. (Color online) Orientation of the current density and integration area for obtaining the photocurrent.

acceleration and deceleration. The contact stripes and accelerating fields are chosen such that the current has only an x component, i.e. $\vec{j} = \vec{e}_x j$. For now, we assume a material with a long lifetime, $\tau_{rec} \gg \tau_{tr}$. We assume the geometry depicted as in Fig. 50 with vanishing electrode width, w.

The photocurrent of a single gap is given by integrating the current density over the gap cross section oriented along the (y, z)-plane, providing

$$i_0(t) = \int_A j_x(x, y, z, t) dz\, dy = \int j_{s,x}(x, y, t) dy \tag{C1}$$

where we have introduced the sheet carrier density $j_{s,x}(x, y) = \int j(x, y, z) dz$. For simplicity, we omit the index x in $j_s(x, y, t)$. The total current of the structure is the sum over all gaps,

$$I_0(t) = \sum i_0(t) = \sum \int j_s(x, y, t) dy. \tag{C2}$$

For a sufficiently small gap width compared to the spot size of the optical beam with radius ρ_0, we can replace the sum by an integration providing

$$I_0^{id} = \sum i_0 \approx \int\int j_{s,x}(x, y, t) dy \frac{dx}{s}, \tag{C3}$$

where s is the gap width. Actually, we should replace the gap size s by the period $p = s_a + s_{bl} + w$. This would just alter the formula by the geometrical efficiency $\eta_{geo} = s_a/(s_a + s_{bl} + w)$, with s_{bl} the width of blocked gaps and $s = s_a$ the width of active gaps. To simplify the calculations, we are neglecting the geometry factor, η_{geo} throughout this appendix and assume a homogeneously absorbing area and vanishing contact widths w. The number of carriers is proportional to the incident optical power. Hence, the local current density becomes

$$j_s(\rho, t) = j_{s,0}(t) \exp\left(-\frac{\rho^2}{\rho_0^2}\right). \tag{C4}$$

with $\rho = \sqrt{x^2 + y^2}$. For sufficiently small gaps s all infinitesimal dipole currents, $i_0(t)$ are phase coherent. The integrations in Eq. (C3) provide

$$I_0 = \frac{\pi \rho_0^2}{s} j_{s,0}. \tag{C5}$$

In case of a material with long lifetime, the external current is related to the optical power as $I_0(t) = eP_L(t)/(hv_0)$. We

can now express the sheet photocurrent density by the optical power as

$$j_s(\rho,t) = j_{s,0}(t)\exp\left(-\frac{\rho^2}{\rho_0^2}\right) = \frac{s}{\pi\rho_0^2}\frac{eP_L(t)}{h\nu_0}\exp\left(-\frac{\rho^2}{\rho_0^2}\right), \tag{C6}$$

with $j_{s,0}(t) = [s/(\pi\rho_0^2)\cdot\{eP_L(t)/(h\nu_0)\}]$. With the definition used in connection with Eq. (77), the source term, $D(t) = \pi\rho_0^2\cdot\partial j_{s,0}(t)/\partial t$, becomes

$$D(t) = \frac{\partial}{\partial t}s\frac{eP_L(t)}{h\nu_0}, \tag{C7}$$

which is independent of ρ_0. For harmonic time dependence of the optical power, $P_L(t) = [1+\exp(i\omega_{THz}t)]P_{L,0}$ we get for the source term

$$D(t) = i\omega_{THz}s\frac{eP_{L,0}}{h\nu_0}\exp(i\omega_{THz}t) = i\omega_{THz}sI_0^{id}\exp(i\omega_{THz}t). \tag{C8}$$

The appearance of the gap spacing s may be surprising. When the electron reaches the contact, it does not contribute to the x component of the radiated electric field anymore because of the contact orientation. We can therefore interpret the source term, $D(t)$, as the time derivative of the dipole current, i.e., the photocurrent times the dipole length, s. For larger gaps, $s > 0.5v_{\rm sat}/\nu_{THz}$, we can no longer assume phase coherence of the infinitesimal currents, $i_0(t)$. In analogy to a p-i-n diode with a completely absorbing intrinsic layer as described in Appendix A, we get an additional roll-off term for the source term of $\eta_{D,tr} \approx 1/(1+i\tau_{tr}\nu_{THz}/0.55)$, with $\tau_{tr} = s/v_{\rm sat}$.

In Eq. (C8), we implicitly assumed a long lifetime of the material by setting $I_0(t) = eP_L(t)/(h\nu_0)$. A more general approach to derive the source term for materials with short carrier lifetime or pulsed operation uses the continuity equation, providing for the sheet carrier density

$$j_s(\rho,t,t') = eN_s(\rho,t,t')\cdot v(t,t'). \tag{C9}$$

with $N_s(\rho,t,t')$ the 2D carrier density at time t but generated at time t'. For the case of continuous-wave photomixing we can assume transport at the saturation velocity, $v(t) = v_{\rm sat} = \text{const}$. The total photocurrent density becomes

$$j_s(\rho,t) = ev_{\rm sat}\int\frac{\partial N_s(\rho,t,\tau)}{\partial\tau}\exp(-\tau/\tau_{\rm rec})d\tau, \tag{C10}$$

with the finite lifetime of the carriers $\tau_{\rm rec}$. We can express the 2D carrier density by the incident optical intensity as

$$\frac{\partial N_s(\rho,t,\tau)}{\partial\tau} = \frac{I_L(\rho,t,\tau)}{h\nu_0} = \frac{P_{L,0}}{h\nu_0}\exp[i\omega_{THz}(t-\tau)]\cdot\frac{1}{\pi\rho_0^2}\exp\left(-\frac{\rho^2}{\rho_0^2}\right). \tag{C11}$$

With $eP_L/h\nu_0 = I_0^{id}$ and the definition of the sheet current density amplitude of $j_s(\rho,t) = j_{s,0}(t)\cdot\exp(-\rho^2/\rho_0^2)$ we get, by substituting Eq. (C11) in Eq. (C10),

$$j_{s,0}(t) = v_{\rm sat}I_0^{id}\frac{1}{\pi\rho_0^2}\int_0^{\tau_{tr}} e^{i\omega_{THz}(t-\tau)}\cdot e^{-\tau/\tau_{\rm rec}}d\tau \tag{C12}$$

The source term, $D(t) = \pi\rho_0^2\partial j_{s,0}(t)/\partial t$ can be expressed as

$$D(t) = i\omega_{THz}v_{\rm sat}I_0^{id}e^{i\omega t_{THz}}\int_0^{\tau_{tr}} e^{-i\omega_{THz}\tau}\cdot e^{-\tau/\tau_{\rm rec}}d\tau. \tag{C13}$$

We see that the source term is proportional to the quasiacceleration, $\omega_{THz}v_{\rm sat}$ [or, alternatively, $\omega_{THz}v_{\rm sat} = \omega_{THz}^2 l(\omega_{THz})$ with a frequency-dependent dipole length $l(\omega_{THz}) = v_{\rm sat}/\omega_{THz}$]. For showing that Eq. (C13) and Eq. (C8) are indeed the same for long lifetimes, we need to evaluate the integral in Eq. (C13). In Appendix A we have shown that at sufficiently low frequencies, the AC and the low frequency (DC) components of the photocurrent are identical but differ by a transit-time-dependent term at high frequencies. For simplicity, we now calculate the low-frequency limit of Eq. (C13), i.e., assuming $\omega_{THz}^{-1} \gg \max(\tau_{tr},\tau_{\rm rec})$ such that we can omit the ω_{THz} dependence in the integral (quasistatic approximation, $\omega_{THz}\tau \to 0$). The high-frequency roll-off, η_t, may be included later. We get

$$D(t) = i\omega_{THz}v_{\rm sat}I_0^{id}e^{i\omega_{THz}t}\tau_{\rm rec}[1-\exp(-\tau_{tr}/\tau_{\rm rec})]. \tag{C14}$$

For material with a long lifetime, $\tau_{\rm rec} \gg \tau_{tr}$, the Taylor expansion of Eq. (C14) provides

$$D(t) = i\omega_{THz}v_{\rm sat}\tau_{tr}I_0^{id}e^{i\omega_{THz}t} \tag{C15}$$

We can express $v_{\rm sat}\tau_{tr} = s$. In this limit of a long lifetime, Eq. (C15) results in the earlier derived Eq. (C8). The reduction of the source term amplitude due to the transit-time roll off can be included similar to the reduction of the AC photocurrent in p-i-n diodes with fully absorbing intrinsic layers. We get approximately $|\eta_{D,tr}| \approx 1/\sqrt{1+(v_{THz}\tau_{tr}/0.55)^2}$. The THz power is reduced by $|\eta_{D,tr}|^2 = \eta_t, pin$. For material with short lifetime, $\tau_{\rm rec} \ll \tau_{tr}$, the exponential term in Eq. (C14) can be omitted, providing

$$D(t) = i\omega_{THz}v_{\rm sat}\tau_{\rm rec}I_0^{id}e^{i\omega_{THz}t} \tag{C16}$$

At high frequencies, the current amplitude is reduced by $|\eta_{D,rec}| \approx 1/\sqrt{1+(2\pi v_{THz}\tau_{rec})^2}$ (which provides the THz power roll-off of $\eta_t = |\eta_{D,rec}|^2 = 1/[1+(2\pi v_{THz}\tau_{rec})^2]$ as derived in Sec. II B 1 for short-lifetime material). Omitting the harmonic time dependence, the amplitude of the source term, D_0, becomes

$$D_0 = i\omega_{THz}v_{\rm sat}\tau_{\rm rec}I_0^{id}\eta_{D,\rm rec} \tag{C17}$$

Again, the interpretation of the source term as time derivative of the local AC current, $I = \eta_{D,\rm rec}I_0^{id}$ times dipole length $v_{\rm sat}\tau_{\rm rec}$ holds.

In this case of a short lifetime, the external photocurrent is lowered by $I^{\rm ext} = gI_0^{id}$. By using $\tau_{\rm rec} = g\tau_{\rm tr}$ we may rewrite the amplitude of the source term in Eq. (C17) as

$$D_0 = i\omega_{THz}v_{sat}\tau_{tr}gI_0^{id}\eta_{D,rec} = i\omega_{THz}s\cdot gI_0^{id}\eta_{D,rec} = i\omega_{THz}sI^{ext}\eta_{D,rec} \tag{C18}$$

We see that in case of a material with short lifetime, Eq. (C8) has to be altered by the photoconductive gain, g, or

I_0^{id} has to be replaced by the external photocurrent I_{ext}. However, it is clear from Eq. (C17) that the emitted THz power is independent of s in this case. By expressing D_0 in terms of incident optical power, $I_0^{id} = eP_{L,0}/h\nu_0$, we obtain

$$D_0 = i\omega_{THz} v_{\mathrm{sat}} \tau_{\mathrm{rec}} \left(\frac{eP_{L,0}}{h\nu_0}\right) \eta_{D,\mathrm{rec}} \tag{C19}$$

Summarizing the results for transport with the saturation velocity from Eqs. (C8), (C17), and (C18), we can express the THz power emitted from an LAQD emitter, $P_{THz}^{LAQD} = 1/2 \cdot Zn_{THz}^2/6\pi c_0^2 |D(t)|^2$, by any of the following forms:

$$P_{THz}^{LAQD} = \frac{1}{2} \cdot \frac{Zn_{THz}^2}{6\pi c_0^2} (\omega_{THz} v_{\mathrm{sat}})^2 [eN_0^{(2d)}]^2 \eta_D^2 \tag{C20}$$

$$P_{THz}^{LAQD} = \frac{1}{2} \cdot \frac{Z_0 n_{THz}}{6\pi c_0^2} (\omega_{THz} v_{\mathrm{sat}})^2 [eN_0^{(2d)}]^2 \eta_D^2 \tag{C21}$$

$$P_{THz}^{LAQD} = \frac{1}{2} \cdot \frac{Zn_{THz}^2}{6\pi c_0^2} (\omega_{THz} v_{\mathrm{sat}} \tau)^2 \left(\frac{eP_{L,0}}{h\eta_0}\right) \eta_D^2 \tag{C22}$$

$$\begin{aligned} P_{THz}^{LAQD} &= \frac{1}{2} \cdot \frac{Zn_{THz}^2}{6\pi c_0^2} (\omega_{THz} v_{\mathrm{sat}} \tau)^2 (I_0^{id})^2 \eta_D^2 \\ &= \frac{1}{2} \cdot \frac{Zk^2}{6\pi} (v_{\mathrm{sat}} \tau)^2 (I_0^{id})^2 \eta_D^2 \end{aligned} \tag{C23}$$

$$P_{k^2}^{LAQD} = \frac{1}{2} \cdot \frac{Zn_{THz}^2}{6\pi c_0^2} (\omega_{THz} gs)^2 (I_0^{id})^2 \eta_D^2 = \frac{1}{2} \cdot \frac{Zk_{THz}^2}{6\pi} (gs)^2 (I_0^{id})^2 \eta_D^2 \tag{C24}$$

$$P_{k^2}^{LAQD} = \frac{1}{2} \cdot \frac{Zn_{THz}^2}{6\pi c_0^2} (\omega_{THz} s)^2 (I^{ext})^2 \eta_D^2 = \frac{1}{2} \cdot \frac{Zk_{THz}^2}{6\pi} (s)^2 (I^{ext})^2 \eta_D^2 \tag{C25}$$

with $\tau = \tau_{\mathrm{rec}}$ or τ_{tr}, whatever is shorter, and $\eta_D = \eta_{D,\mathrm{tr}}$ or $\eta_{D,\mathrm{rec}}$. These expressions correspond formally to the power emitted by a Hertzian dipole[117] of length $l_0 = s$ with a total current of $\eta_D I^{\mathrm{ext}} = \eta_D g I_0^{id}$, or to the power emitted by a Hertzian dipole of length $l_0 = gs$ and a current of $\eta_D {I_0}^{id}$. An alternative interpretation is the emission of a Hertzian dipole consisting of $N_s = \tau \eta_D P_{L,0}/(h\nu_0)$ oscillating charges at a (frequency-dependent) dipole length of $l\ (\omega_{THz}) = v_{\mathrm{sat}}/\omega_{\mathrm{THz}}$. With the dipole moment of $p\ (\omega_{THz}) = N_s l\ (\omega_{THz})$ this yields the textbook formula

$$P_{THz}^{LAQD} = \frac{|p(\omega_{THz})|^2 (\omega_{THz})^4}{12\pi e_0 c_0^3 / n_{THz}}. \tag{C26}$$

ACKNOWLEDGMENTS

The authors want to acknowledge Viktor Krozer, Univ. of Denmark, for antenna simulations. Furthermore, the authors want to thank Jan Schür, Harald Schwefel, and Sebastian Bauerschmidt, Univ. of Erlangen-Nuremberg, Germany, for their experimental and theoretical aid. Many thanks go to L. P. Schmidt, Univ. of Erlangen-Nuremberg, E. R. Brown, Univ. of California, Santa Barbara, USA, and to H. Roskos, H. Maestre, and A. Lysauskas, Univ. of Frankfurt, Germany, for their hospitality in their labs. We thank Hong Lu, J. D. Zimmerman, and M. Hanson for sample growth and fruitful discussions.

We thank Kartik Sheth, NRAO, for information on the ALMA project. We also want to thank the European space agency (ESA) and the Deutsche Forschungsgemeinschaft (DFG) for financial support.

[1] J. E. Bjarnason, T. L. J. Chan, A. W. M. Lee, M. A. Celis, and E. R. Brown, Appl. Phys. Lett. **85**, 519 (2004).
[2] Y. Zhang, X.-H. Peng, Y. Chen, J. Chen, A. Curioni, W. Andreoni, S. K. Nayak, and X.-C. Zhang, Chem. Phys. Lett. **452**, 59 (2008).
[3] Y.-S. Jin, G.-J. Kim, and S.-G. Jeon, J. Korean Phys. Soc. **49**, 513 (2006).
[4] I. S. Gregory, W. R. Tribe, C. Baker, B. E. Cole, M. J. Evans, L. Spencer, M. Pepper, and M. Missous, Appl. Phys. Lett. **86**, 204104 (2005).
[5] S. Wang and X.-C. Zhang, J. Phys. D: Appl. Phys. **37**, R1 (2004).
[6] R. Wilk, F. Breitfeld, M. Mikulics, and M. Koch, Appl. Opt. **47**, 3023 (2008).
[7] G. Carelli, D. Pereira, and F. Strumia, IEEE J. Quantum Electron. **31**, 144 (1995).
[8] A. S. Pine, R. D. Suenram, E. R. Brown, and K. A. McIntosh, J. Mol. Spectrosc. **175**, 37 (1996).
[9] D. M. Mittleman, R. H. Jacobsen, R. Neelamani, R. G. Baraniuk, and M. C. Nuss, Appl. Phys. B **67**, 379 (1998).
[10] D. F. Plusquellic, K. Siegrist, E. J. Heilweil, and O. Esenturk, ChemPhysChem. **8**, 2412 (2007).
[11] B. M. Fischer and D. Abbott, IEEE IRMMW-THz, 398 (2007).
[12] B. M. Fischer, H. Helm, and P. U. Jepsen, Proc. SPIE **6038**, 603809 (2006).
[13] M. Nagel, P. Haring-Bolivar, M. Brucherseifer, and H. Kurz, Appl. Phys. Lett. **80**, 154 (2002).
[14] S. A. Harmon and R. A. Cheville, Appl. Phys. Lett. **85**, 2128 (2004).
[15] K. Kawase, Y. Ogawa, H. Minamide, and H. Ito, Semicond. Sci. Technol. **20**, 258 (2005).
[16] M. Tonouchi, Nature Photon. **1**, 97 (2007).
[17] M. J. Fitsch, D. Schauki, C. Dodson, and R. Osiander, Proc. SPIE **5411**, 84 (2004).
[18] H.-B. Liu, H. Zhong, N. Karpowicz, Y. Chen, and X.-C. Zhang, Proc. IEEE **95**, 1514 (2007).
[19] E. R. Brown, J. E. Bjarnason, T. L. J. Chan, A. W. M. Lee, and M. A. Celis, Appl. Phys. Lett. **85**, 3438 (2004).
[20] For more information, see the ESA website, http://www.esa.int/specials/herschel/index.html.
[21] For more information, see the Atacama large millimeter/submillimeter array website, http://almaobservatory.org/.
[22] A. Maestrini, J. Ward, J. Gill, H. Javadi, E. Schlecht, G. Chattopadhyay, F. Maiwald, N. R. Erickson, and I. Mehdi, IEEE Microw. Wirel. Compon. Lett. **14**, 253 (2004).
[23] G. Scalari, C. Walther, M. Fischer, R. Terazzi, H. Beere, D. Ritchie, and J. Faist, Laser Photonics Rev. **3**, 45 (2009).
[24] K. Kawase, J.-I. Shikata, and H. Ito, J. Phys. D: Appl. Phys. **34**, R1 (2001).
[25] E. R. Brown, K. A. McIntosh, K. B. Nichols, and C. L. Dennis, Appl. Phys. Lett. **66**, 285 (1995).
[26] A. Dobroiu, M. Yamashita, Y. N. Ohshima, Y. Morita, C. Otani, and K. Kawase, Appl. Opt. **43**, 5637 (2004).
[27] B. P. Gorshunov, A. A. Volkov, A. S. Prokhorov, and I. E. Spektor, Phys. Solid State **50**, 2001 (2008).
[28] E. R. Brown, J. R. Söderström, C. D. Parker, L. J. Mahoney, K. M. Molvar, and T. C. McGill, Appl. Phys. Lett. **58**, 2291 (1991).
[29] M. Tachiki, M. Iizuka, K. Minami, S. Tejim, and H. Nakamura, Phys. Rev. B **71**, 134515 (2005).
[30] L. Ozyuzer, A. Koshelev, C. Kurter, N. Gopalsami, Q. Li, M. Tachiki, K. Kadowaki, T. Yamamoto, H. Minami, H. Yamaguchi, T. Tachiki, K. E. Gray, W.-K. Kwok, and U. Welp, Science **318**, 1291 (2007).
[31] R. Köhler, A. Tredicucci, F. Beltram, H. E. Beere, E. H. Linfield, A. G. Davies, D. A. Ritchie, R. C. Iotti, and F. Rossi, Nature **417**, 156 (2002).
[32] C. Walther, G. Scalari, J. Faist, H. Beere, and D. Ritchie, Appl. Phys. Lett. **89**, 231121 (2006).
[33] J. A. Fan, M. A. Belkin, F. Capasso, S. P. Khanna, M. Lachab, G. Davies, and E. H. Linfield, Appl. Phys. Lett. **92**, 031106 (2008).
[34] F. Zernike and P. R. Berman, Phys. Rev. Lett. **15**, 999 (1965).
[35] Y. J. Ding, IEEE J. Sel. Top. Quantum Electron. **13**, 705 (2007).
[36] T. Tanabe, K. Suto, J. Nishizawa, T. Kimura, and K. Saito, J. Appl. Phys. **93**, 4610 (2003).
[37] D. Creeden, J. C. McCarthy, P. A. Ketteridge, T. Southward, P. G. Schunemann, and J. J. Komiak, IEEE J. Sel. Top. Quantum Electron. **13**, 732 (2007).

[38]I. Shoji, T. Kondo, A. Kitamoto, M. Shirane, and R. Ito, J. Opt. Soc. Am. B **14**, 2268 (1997).
[39]J. M. Yarborough, S. S. Sussman, H. E. Purhoff, R. H. Pantell, and B. C. Johnson, Appl. Phys. Lett. **78**, 102 (2001).
[40]K. Kawase, J. ichi Shikata, K. Imai, and H. Ito, Appl. Phys. Lett. **78**, 2819 (2001).
[41]P. N. Butcher and D. Cotter, *The elements of nonlinear optics*, (Cambridge University Press, Cambridge, U. K., 1990).
[42]Y. Shimada, K. Hirakawa, M. Obnoblioudov, and K. A. Chao, Phys. Rev. Lett. **90**, 046806 (2003).
[43]B. Rosam, K. Leo, L. Yang, and M. M. Dignam, Appl. Phys. Lett. **85**, 4612 (2004).
[44]C. Waschke, H. G. Roskos, R. Schwedler, K. Leo, H. Kurz, and K. Köhler, Phys. Rev. Lett. **70**, 3319 (1993).
[45]A. Schwanhäußer, M. Betz, M. Eckardt, S. Trumm, L. Robledo, S. Malzer, A. Leitenstorfer, and G. H. Döhler, Phys. Rev. B **70**, 085211 (2004).
[46]R. Ascazubi, I. Wilke, K. Denniston, H. Lu, and W. J. Schaff, Appl. Phys. Lett. **84**, 4810 (2004).
[47]P. Gu and M. Tani, in *Terahertz optoelectronics*, Topics in Applied Physics Vol. 97, p. 70, edited by K. Sakai (Springer Verlag, Berlin, 2005)
[48]J. N. Heyman, P. Neocleous, D. Herbert, P. A. Crowell, T. Müller, and K. Unterrainer, Phys. Rev. B **64**, 085202 (2001).
[49]M. Hangyo, M. Migita, and K. Nakayama, J. Appl. Phys. **90**, 3409 (2001).
[50]C. Weiss, R. Wallenstein, and R. Beigang, Appl. Phys. Lett. **77**, 4160 (2000).
[51]M. Awad, M. Nagel, H. Kurz, J. Herfort, and K. Ploog, Appl. Phys. Lett. **91**, 181124 (2007).
[52]A. Dreyhaupt, S. Winnerl, T. Dekorsy, and M. Helm, Appl. Phys. Lett. **86**, 121114 (2005).
[53]M. Beck, H. Schäfer, G. Klatt, J. Demsar, S. Winnerl, M. Helm, and T. Dekorsy, Opt. Express **18**, 9251 (2010).
[54]H. Ito, A. Hirata, T. Minotani, A. Sasaki, Y. Hirota, and T. Ishibasi, IEEE Proc.: Optoelectron. **150**, 138 (2003).
[55]C. C. Renaud, M. Robertson, D. Rogers, R. Firth, P. J. Cannard, R. Moore, and A. J. Seeds, Proc. SPIE, **6194**, 6164C (2006).
[56]B. Ferguson and X.-C. Zhang, Nature Mater **1**, 26 (2002).
[57]E. R. Brown, Int. J. High Speed Electron. Syst. **13**, 497 (2003).
[58]D. Saeedkia and S. Safavi-Naeini, J. Lightwave Technol. **26**, 2409 (2008).
[59]K. Sakai, Ed., *Terahertz optoelectronics*, Topics in Applied Physics Vol. 97 (Springer Verlag, Berlin, 2005).
[60]C. A. Balanis, *Antenna Theory: Analysis and design*, 3rd ed. (John Wiley & Sons, Hoboken, New Jersey, USA, 2005).
[61]C. C. Renaud, L. Ponnampalam, F. Pozzi, E. Rouvalis, D. Moodie, M. Robertson, and A. J. Seeds, IEEE Microw. Photon. **55** (2008).
[62]J. B. D. Soole and H. Schumacher, IEEE Trans. Electron. Devices **37**, 2285 (1990).
[63]J. D. Dyson, IRE Trans. Antenna Propag. 181 (1959).
[64]Y. Huo, G. W. Taylor, and R. Bansal, Int. J. Infrared Millim. Waves **23**, 819 (2002).
[65]S. Verghese, K. A. McIntosh, and E. R. Brown, Appl. Phys. Lett. **71**, 2743 (1997).
[66]G. C. Loata, T. Löffler, and H. G. Roskos, Appl. Phys. Lett. **90**, 052101 (2007).
[67]J. E. Pedersen, V. G. Lyssenko, J. M. Hvam, P. U. Jepsen, S. R. Keiding, C. B. Sorensen, and P. E. Lindelof, Appl. Phys. Lett. **62**, 1265 (1993).
[68]G. C. Loata, M. D. Thomson, T. Löffler, and H. G. Roskos, Appl. Phys. Lett. **91**, 232506 (2007).
[69]G. Rodriguez and A. J. Taylor, Opt. Lett. **21**, 1046 (1996).
[70]C. Kadow, J. A. Johnson, K. Kolstad, J. P. Ibbetson, and A. C. Gossard, J. Vac. Sci. Technol. B **18**, 2197 (2000).
[71]C. Kadow, A. W. Jackson, A. C. Gossard, S. Matsuura, and G. A. Blake, Appl. Phys. Lett. **76**, 3510 (2000).
[72]M. Griebel, J. H. Smet, D. C. Driscoll, J. Kuhl, C. Alvarez-Diez, N. Freytag, C. Kadow, A. C. Gossard, and K. von Klitzing, Nature Mater. **2**, 122 (2003).
[73]C. Kadow, "Self-assembled ErAs islands in GaAs for photomixer devices," Ph.D. thesis, University of California Santa Barbara, 2000.
[74]J. R. Demers, R. T. Logan, and E. R. Brown, Proc. IEEE Microw. Photon. (2007)
[75]R. A. Metzger, A. S. Brown, L. G. McCray, and J. A. Henige, J. Vac. Sci. Technol. B **11**, 798 (1993).
[76]B. Sartorius, H. Roehle, H. Künzel, J. Böttcher, M. Schlak, D. Stanze, H. Venghaus, and M. Schell, Opt. Express **16**, 9565 (2008).
[77]C. Carmody, H. H. Tan, C. Jagadish, A. Gaarder, and S. Marcinkevicius, Appl. Phys. Lett. **82**, 3913 (2003).
[78]N. Chimot, J. Mangeney, L. Joulaud, P. Crozat, H. Bernas, K. Blary, and J. F. Lampin, Appl. Phys. Lett. **87**, 193510 (2005).
[79]J. Mangeney, N. Chimot, L. Meignien, N. Zerounian, P. Crozat, K. Blary, J. F. Lampin, and P. Mounaix, Opt. Express **15**, 8943 (2007).
[80]J. Mangeney, A. Merigault, N. Zerounian, and P. Crozat, Appl. Phys. Lett. **91**, 241102 (2007).
[81]J. Mangeney and P. Crozat, J. Phys. Colloq. **9**, 142 (2008).
[82]D. C. Driscoll, M. P. Hanson, A. C. Gossard, and E. R. Brown, Appl. Phys. Lett. **86**, 051908 (2005).
[83]F. Ospald, D. Maryenko, K. von Klitzing, D. C. Driscoll, M. P. Hanson, H. Lu, A. C. Gossard, and J. H. Smet, Appl. Phys. Lett. **92**, 131117 (2008).
[84]E. R. Brown, D. C. Driscoll, and A. C. Gossard, Semicond. Sci. Technol. **20**, 199 (2005).
[85]M. van Exter, C. Fattinger, and D. Grischkowsky, Opt. Lett. **14**, 1128 (1989).
[86]D. C. Driscoll, M. Hanson, C. Kadow, and A. C. Gossard, Appl. Phys. Lett. **78**, 1703 (2001).
[87]M. Eckardt, "Aspects of high-field carrier transport in AlGaAs-Towards an efficient THz-emitter," Ph.D. thesis, Lehrstuhl für Mikrocharakterisierung, Erlangen, Germany, 2004.
[88]B. K. Ridley, *Quantum processes in semiconductors* (Oxford University Press, Oxford, U. K., 1999).
[89]M. S. Shur and L. F. Eastman, IEEE Trans. Electron. Devices **26**, 1677 (1979).
[90]H. Ito, F. Nakajima, T. Futura, and T. Ishibashi, Semicond. Sci. Technol. **20**, 191 (2005).
[91]G. H. Döhler, F. Renner, O. Klar, M. Eckardt, A. Schwanhäußer, S. Malzer, D. Driscoll, M. Hanson, A. C. Gossard, G. Loata, T. Löffler, and H. Roskos, Semicond. Sci. Technol. **20**, 178 (2005).
[92]K. J. Williams and R. D. Esman, IEEE Photonics Technol. Lett. **6**, 639 (1994).
[93]M. N. Feiginov, J. Appl. Phys. **102**, 084510 (2007).
[94]A. Beling and J. C. Campbell, J. Lightwave Technol. **27**, 343 (2009).
[95]P. Bhattacharya, Ed., *Properties of Lattice-Matched and Strained Indium Gallium Arsenide* (Inspec, New York, 1993).
[96]For more information, see the Ioffe Physico-Technical Institute website, http://www.ioffe.ru/sva/nsm/semicond/index.html.
[97]K. J. Williams and R. D. Esman, J. Lightwave Technol. **17**, 1443 (1999).
[98]A. Dyson, I. D. Henning, and M. J. Adams, IEEE J. Sel. Top. Quantum Electron. **14**, 277 (2008).
[99]N. Shimizu, N. Watanabe, T. Furuta, and T. Ishibashi, IEEE Photonics Technol. Lett. **10**, 412 (1998).
[100]T. Ishibashi, T. Furuta, H. Fushimi, and H. Ito, Proc. SPIE **4283**, 469 (2001).
[101]H. Ito and T. Ishibashi, Device Research Conference **58**, 165 (2000).
[102]T. Ishibashi, T. Furuta, H. Fushimi, S. Kodama, H. Ito, T. Nagatsuma, N. Shimizu, and Y. Miyamoto, IEICE Trans. Electron. **E83C**, 938 (2000).
[103]E. Rouvalis, C. C. Renaud, D. G. Moodie, M. J. Robertson, and A. J. Seeds, Opt. Express **18**, 11105 (2010).
[104]F. Nakajima, T. Furuta, and H. Ito, Electron. Lett. **40**, 1297 (2004).
[105]A. Beck, G. Ducournau, M. Zaknoune, E. Peytavit, T. Alkalin, J. F. Lampin, F. Mollot, F. Hindle, C. Yang, and G. Mouret, Electron. Lett. **44**, 1320 (2008).
[106]A. Hirata, T. Kosugi, H. Takahashi, R. Yamaguchi, F. Nakajima, T. Furuta, H. Ito, H. Sugahara, Y. Sato, and T. Nagatsuma, IEEE Trans. Microw. Theory Tech. **54**, 1937 (2006).
[107]P. Pohl, F. H. Renner, M. Eckardt, A. Schwanhäußer, A. Friedrich, Ö. Yüksekdag, S. Malzer, G. H. Döhler, P. Kiesel, D. Driscoll, M. Hanson, and A. C. Gossard, Appl. Phys. Lett. **83**, 4035 (2003).
[108]S. Preu, S. Malzer, G. H. Döhler, H. Lu, A. C. Gossard, and L. J. Wang, Semicond. Sci. Technol. **25**, 115004 (2010).
[109]F. Renner, "The nipnip-THz-emitter," Ph. D. thesis, Lehrstuhl für Mikrocharakterisierung, Erlangen, Germany, 2004.
[110]S. Preu, F. H. Renner, S. Malzer, G. H. Döhler, L. J. Wang, T. L. J. Wilkinson, E. R. Brown, M. Hanson, and A. C. Gossard, Appl. Phys. Lett. **90**, 212115 (2007).
[111]Z. D. Taylor, E. R. Brown, J. E. Bjarnason, M. P. Hanson, and A. C. Gossard, Opt. Lett. **31**, 1729 (2006).
[112]B. Sartorius, M. Schlak, D. Stanze, H. Roehle, H. Künzel, D. Schmidt, H.-G. Bach, R. Kunkel, and M. Schell, Opt. Express **17**, 15001 (2009).

[113]H. Ito, F. Nakajima, T. Furuta, K. Yoshino, Y. Hirota, and T. Ishibashi, Electron. Lett. **39**, 1828 (2003).
[114]D. S. Kim and D. S. Citrin, Appl. Phys. Lett. **88**, 161117 (2006).
[115]A. Dreyhaupt, S. Winnerl, M. Helm, and T. Dekorsy, Opt. Lett. **31**, 1546–1548 (2006).
[116]A. Dreyhaupt, S. Winnerl, T. Dekorsy, and M. Helm, Appl. Phys. Lett. **86**, 121114 (2005).
[117]J. D. Jackson, *Klassische Elektrodynamik* 3rd ed. (De Gruyter, Weinheim, Germany, 2002).
[118]The radiation resistance for the external circuit, however, needs to be related to the external current, $I_0 = gI_0^{id}$. Hence, the equivalent resistance for the external circuit is R_{rad}^{LAQD}/g^2 in both Eq. (86) and Eq. (89) and the equivalent dipole length becomes $l_0 = s$.
[119]D. R. Jackson and N. G. Alexopoulos, Int. J. Infrared Millim. Waves **7**, 1 (1986).
[120]A. Leitenstorfer, S. Hunsche, J. Shah, M. C. Nuss, and W. H. Knox, Phys. Rev. B **61**, 16 642 (2000).
[121]G. Matthäus, S. Nolte, R. Hohmuth, M. Voitsch, W. Richter, B. Pradarutti, S. Riehemann, G. Notni, and A. Tünnermann, Appl. Phys. Lett. **93**, 091110 (2008).
[122]J. H. Kim, A. Polley, and S. E. Ralph, Opt. Lett. **30**, 2490 (2005).
[123]F. Peter, S. Winnerl, H. Schneider, M. Helm, and K. Köhler, Appl. Phys. Lett. **93**, 101102 (2008).
[124]J. Kindler, P. Banzer, S. Quabis, U. Peschel, and G. Leuchs, Appl. Phys. B **89**, 517 (2007).
[125]S. Winnerl, B. Zimmermann, F. Peter, H. Schneider, and M. Helm, Opt. Express **17**, 1571 (2009).
[126]T. Dekorsy, P. Leisching, C. Waschke, K. Köhler, K. Leo, H. G. Roskos, and H. Kurz, "Semicond. Sci. Technol. **9**, 1959 (1994).
[127]D. F. Filipovic, G. P. Gauthier, S. Raman, and G. M. Rebeiz, "Off-axis properties of silicon and quartz dielectric lens antennas," IEEE Trans. Antennas Propag. **45**, 760 (1997).
[128]A. Hirata, H. Takahashi, R. Yamaguchi, T. Kosugi, K. Murata, T. Nagatsuma, N. Kukutsu, and Y. Kado, J. Lightwave Technol. **26**, 2338 (2008).
[129]T. L. J. Chan, J. E. Bjarnason, A. W. M. Lee, M. A. Celis, and E. R. Brown, Appl. Phys. Lett. **85**, 2523 (2004).
[130]A. Hofmann, E. Hörster, J. Weinzierl, L.-P. Schmidt, and H. Brand, in Proc. 33rd Eur. Microw. Conf., 2003, pp. 955.
[131]S. Preu, H. G. L. Schwefel, G. H. Döhler, L. J. Wang, M. Hanson, J. D. Zimmerman, and A. C. Gossard, Opt. Express **16**, 7336 (2008).
[132]L. Sun, Z.-H. Lv, W. Wu, W.-T. Liu, and J.-M. Juan, Appl. Opt. **49**, 2066 (2010).
[133]C. C. Homes, G. L. Carr, R. P. S. M. Lobo, J. D. LaVeigne, and D. B. Tanner, Appl. Opt. **46**, 7884 (2007).
[134]H.-W. Chen, C.-M. Chiu, C.-H. Lai, J.-L. Kuo, P.-J. Chiang, Y.-J. Hwang, and H.-C. Chang, J. Lightwave Technol. **27**, 1489 (2009).
[135]D. Turchinovich, A. Kammoun, P. Knobloch, T. Dobbertin, and M. Koch, Appl. Phys. A **74**, 291 (2002).
[136]N. Krumbholz, K. Gerlach, F. Rutz, M. Koch, P. Piesiewicz, T. Kürner, and D. Mittleman, Appl. Phys. Lett. **88**, 202905 (2006).
[137]C. Jansen, F. Neubauer, J. Helbig, D. M. Mittleman, and M. Koch, IEEE IRMMWTHz, 984–986 (2007).
[138]S. Preu, S. Malzer, G. H. Döhler, Q. Z. Zhao, M. Hanson, J. D. Zimmerman, A. C. Gossard, and L. J. Wang, Appl. Phys. Lett. **92**, 221107 (2008).
[139]M. Musha, A. Ueda, M. Horioshi, K. Nakagawa, M. Ishiguro, K.-I. Ueda, and H. Ito, Opt. Commun. **240**, 201 (2004).
[140]Y. Zhao, J. Zhang, A. Stejskal, T. Liu, V. Elman, Z. Lu, and L. Wang, Opt. Express **17**, 8970 (2009).
[141]S. Preu, S. Malzer, G. H. Döhler, and L. J. Wang, Proc. SPIE **7117**, 28 (2008).
[142]N. Shimizu, T. Nagatsuma, and H. Ito, IEEE Photon. Technol. Lett. **18**, 743 (2006).
[143]S. Preu, S. Malzer, G. H. Döhler, J. Zhang, Z. H. Lu, and L. J. Wang, Proc. SPIE **6194**, 13 (2006).
[144]E. A. Michael, B. Vowinkel, R. Schieder, M. Mikulics, M. Marso, and P. Kordos, Appl. Phys. Lett. **86**, 111120 (2005).
[145]S. Bauerschmidt, S. Preu, S. Malzer, G. H. Döhler, H. Lu, A. C. Gossard, and L. J. Wang, Proc. SPIE **7671**, 76710D (2010)
[146]J. M. Payne and W. P. Shillue, ALMA Memo, **440** (2002).
[147]M. Musha, Y. Sato, K. Nakagawa, K. Ueda, A. Ueda, and M. Ishiguro, Appl. Phys. B **82**, 555 (2006).
[148]A. Ueda, Y. Sekimoto, M. Ishiguro, S. Asayama, M. Yamada, and T. Noguchi, ALMA Memo, **516** (2005).
[149]J.-F. Cliche, B. Shillue, C. Latrasse, M. Tetu, L. D'Addriario, Proc. **5489**, 1115 (2004).
[150]C. Daussy, O. Lopez, A. Amy-Klein, A. Goncharov, M. Guinet, C. Chardonnet, F. Narbonneau, M. Lours, D. Chambon, S. Bize, A. Clairon, and G. Santarelli, Phys. Rev. Lett. **94**, 203904 (2005).
[151]For more information, see the ALMA website, http://www.alma.nrao.edu/projectbk/construction/ (2002).
[152]C.-H. Shin and M. Ohtsu, Opt. Lett. **15**, 1455 (1990).
[153]P. G. Huggard, B. N. Ellison, P. Shen, N. J. Gomes, P. A. Davies, W. Shillue, A. Vaccari, and J. M. Payne, Electr. Lett. **38**, 327 (2002).
[154]J. F. Cliche, W. Shillue, Cont. Syst. Mag., IEEE, **26**, 19 (2006).
[155]R. E. Hills and A. J. Beasley, Proc. SPIE, **7012**, 70120N (2008)
[156]Z. Liu, K. Su, D. E. Gary, J. F. Federici, R. B. Barat, and Z.-H. Michalopoulou, Appl. Opt. **48**, p. 3788–3795 (2009)
[157]H. Stöcker, Ed., *Taschenbuch der Physik*, 5th ed. (Verlag Harri Deutsch, Frankfurt am Main, Germany. 2004).
[158]S. J. Clark and P. U. Jepsen, in Proceedings of the Optical Terahertz Science and Technology Conference (OSA, 2007) p. WA3.
[159]S. Brünken, H. S. P. Müller, C. Endres, F. Lewen, T. Giesen, B. Drouin, J. C. Pearson, and H. Mäder, PhysChemPhys. **9**, 2103 (2007).
[160]S. Matsuura, M. Tani, H. Abe, K. Sakai, H. Ozeki, and S. Saito, J. Mol. Spectrosc. **187**, 97 (1998).
[161]A. Luukanen and J. P. Pekola, Appl. Phys. Lett. **82**, 3970 (2003).
[162]A. Nahata, J. T. Yardley, and T. F. Heinz, Appl. Phys. Lett. **75**, 2524 (1999).
[163]C. Sydlo, O. Cojocari, D. Schönherr, T. Goebel, P. Meissner, and H. L. Hartnagel, Frequenz **62**, 107 (2008).
[164]S. Verghese, K. A. McIntosh, S. Calawa, W. F. Dinatale, E. K. Duerr, and K. A. Molvar, Appl. Phys. Lett. **73**, 3824 (1998).
[165]A. Lisauskas, U. Pfeiffer, E. Öjefors, P. H. Bolivar, D. Glaab, and H. G. Roskos, J. Appl. Phys. **105**, 114511 (2009).
[166]W. Knap, V. Kachorovskii, Y. Deng, S. Rumyantsev, J. Q. Lü, R. Gaska, M. S. Shur, G. Simin, X. Hu, M. A. Khan, C. A. Saylor, and L. C. Brunel, J. Appl. Phys. **91**, 9346 (2002).
[167]S. Kim, J. D. Zimmerman, P. Focardi, A. C. Gossard, D. H. Wu, and M. S. Sherwin, Appl. Phys. Lett. **92**, 253508 (2008).
[168]T. Nagatsuma, A. Hirata, Y. Sato, R. Yamaguchi, H. Takahashi, T. Kosugi, M. Tokumitsu, H. Sugahara, T. Futura, and H. Ito, IECE Trans. Commun. **18**, 1 (2005).
[169]H.-J. Song, N. Shimizu, T. Furuta, K. Suizu, H. Ito, and T. Nagatsuma, J. Lightwave Technol. **26**, 2521 (2008).
[170]T. M. Korter and D. F. Plusquellic, Chem. Phys. Lett. **385**, 45 (2004).
[171]P. Chen, G. A. Blake, M. C. Gaidis, E. R. Brown, K. A. McIntosh, S. Y. Chou, M. I. Nathan, and F. Williamson, Appl. Phys. Lett. **71**, 1601 (1997).
[172]M. Scheller, K. Baaske, and M. Koch, Appl. Phys. Lett. **96**, 151112 (2010).
[173]K. J. Siebert, H. Quast, R. Leonhardt, T. Löffler, M. Thomson, T. Bauer, and H. G. Roskos, Appl. Phys. Lett. **80**, 3003 (2002).
[174]K. Su, Z. Liu, R. B. Barat, D. E. Gary, Z.-H. Michalopoulou, and J. F. Federici, Appl. Opt. **49**, E13–E19 (2010).
[175]H. G. L. Schwefel, and C. G. Poulton, Optics Express, 17(15), 13178 (2009).
[176]H. E. Türeci, H. G. L. Schwefel, P. Jacquod, and A. D. Stone, Prog. Opt. **47**, 75 (2005).
[177]H. E. Türeci and H. G. L. Schwefel, J. Phys. A, **40**, 13869 (2007).
[178]I. Grudinin, V. Ilchenko, A. B. Matsko, M. Mohageg, and L. Maleki, Phys. Rev. A **74**, 063806 (2006).
[179]A. Morand, K. Phan-Huy, Y. Desieres, and P. Benech, J. Lightwave Technol. **22**, 827 (2004).
[180]G. Annino, M. Cassettari, I. Longo, and M. Martinelli, IEEE Trans. Microw. Theory Tech. **45**, 2025 (1997).
[181]A. A. Savchenkov, V. Ilchenko, A. B. Matsko, and L. Maleki, Proc. SPIE **5333**, 154 (2004).
[182]J. Gao, P. Heider, C. J. Chen, X. Yang, C. A. Husko, and C. W. Wong, Appl. Phys. Lett. **91**, 181101 (2007).
[183]H. G. L. Schwefel, N. B. Rex, H. E. Türeci, R. K. Chang, A. D. Stone, T. Ben-Messaoud, and J. Zyss, J. Opt. Soc. Am. B **21**, 923 (2004).
[184]J. Wiersig and M. Hentschel, Phys. Rev. A **73**, 031802 (2006).
[185]C. P. Dettmann, G. V. Morozov, M. Sieber, and H. Waalkens, "Directional emission from an optical microdisk resonator with a point scatterer," EPL **82**, 34002 (2008).
[186]M. L. Povinelli, S. G. Johnson, M. Lonèar, M. Ibanescu, E. J. Smythe, F. Capasso, and J. D. Joannopoulos, Opt. Express **13**, 8286 (2005).
[187]M. Benyoucef, S. Kiravittaya, Y. F. Mei, A. Rastelli, and O. G. Schmidt, Phys. Rev. B **77**, 035108 (2008).
[188]M. Bayer, T. Gutbrod, J. P. Reithmaier, A. Forchel, T. L. Reinecke, P. A. Knipp, A. A. Dremin, and V. D. Kulakovskii, Phys. Rev. Lett. **81**, 2582 (1998).

[189]T. Mukaiyama, K. Takeda, H. Miyazaki, and M. Kuwata-Gonokami, = Phys. Rev. Lett. **82**, 4623 (1999).
[190]D. Cros and P. Guillon, "Whispering gallery dielectric resonator modes for W-band devices," IEEE Trans. Microw. Theory Techn., **38**, 1667 (1990).
[191]X. H. Jiao, P. Guillon, L. A. Bermudez, and P. Auxemery, "Whispering-gallery modes of dielectric structures: Applications to millimeter-wave bandstop filters," IEEE Trans. Microw. Theory Tech. **35**, 1169 (1987).
[192]V. Ilchenko and A. Matsko, IEEE J. Sel. Top. Quantum Electron. **12**, 15 (2006).
[193]F. Vollmer, D. Braun, A. Libchaber, M. Khoshsima, I. Teraoka, and S. Arnold, Appl. Phys. Lett. **80**, 4057 (2002).
[194]G. Annino, M. Cassettari, M. Fittipaldi, L. Lenci, I. Longo, M. Martinelli, C. A. Massa, and L. A. Mardi, Appl. Magn. Reson. **19**, 495 (2000).
[195]A. Andronico, J. Claudon, J.-M. Gérard, V. Berger, and G. Leo, Opt. Lett. **33**, 2416 (2008).
[196]G. D. Boyd, W. L. Bond, and H. L. Carter, J. Appl. Phys. **38**, 1941 (1967).
[197]M. Schall, H. Helm, and S. R. Keiding, "Far infrared properties of electro-optic crystals measured by THz time-domain spectroscopy," Int. J. Infrared Millim. Waves, **20**, 595 (1999).
[198]A. B. Matsko, D. V. Strekalov, and N. Yu, Phys. Rev. A **77**, 043812 (2008).
[199]O. Sevimli, V. Dyadyuk, D. Abbott, L. Stokes, S. Smith, J. Archer, M. Shen, R. Kendall, and J. Tello, IEEE ACES, 434 (2005).
[200]A. Hirata, H. Togo, N. Shimizu, H. Takahashi, K. Okamoto, and T. Nagatsuma, IEICE Trans. Electron. **E88C**, 1458 (2005)
[201]S. S. Dhillon, C. Sirtori, J. Alton, S. Bariberi, A. D. Roosi, H. E. Beere, and D. A. Ritchie, Nature Photon. **1**, 411 (2007).
[202]J. Federici and L. Moeller, J. Appl. Phys. **107**, 111101 (2010).
[203]Note that, according to Fig. 45, the technical current has negative sign and v_h is negative